UNIVERSIDAD DE CHILE
FACULTAD DE CIENCIAS FÍSICAS Y MATEMÁTICAS
DEPARTAMENTO DE FÍSICA

PHASE SINGULARITY DYNAMICS IN OUT OF EQUILIBRIUM ANISOTROPIC SYSTEMS

TESIS PARA OPTAR AL GRADO DE MAGÍSTER EN CIENCIAS, MENCIÓN FÍSICA

ESTEFANIA CAROLINA VIDAL HENRÍQUEZ

PROFESOR GUÍA:
MARCEL G. CLERC GAVILÁN

MIEMBROS DE LA COMISIÓN:
RAFAEL BENGURIA DONOSO
MICHAL KOWALCZYK
MARIO MOLINA GÁLVEZ
STEFANIA RESIDORI

Este trabajo ha sido parcialmente financiado por CONICYT-PCHA/Magíster Nacional/2013 - 221320023.

SANTIAGO DE CHILE
2015

RESUMEN DE LA TESIS PARA OPTAR AL
GRADO DE: Magíster en Ciencias, mención Física
POR: Estefania Vidal Henríquez
FECHA: 06/03/2014
PROFESOR GUÍA: Marcel Clerc Gavilán

DINÁMICA DE SINGULARIDADES DE FASE EN SISTEMAS ANISOTRÓPICOS FUERA DEL EQUILIBRIO

Esta tesis está enfocada en el estudio de singularidades de fase en el contexto de auto organización en sistemas fuera del equilibrio. Nuestra investigación estuvo focalizada en comprender el surgimiento de vórtices en una válvula de cristal líquido nemático (LCLV por sus siglas en inglés) con anclaje homeotrópico iluminada con un haz gaussiano. Este sistema físico permite la creación de vórtices ópticos que son auto-inducidos y que tienen auto-alineamiento, así como la inducción de vórtices positivos en el cristal líquido.
En el primer capítulo se derivó desde principios fundamentales una ecuación que modela este sistema. Inicialmente se analizó el campo eléctrico aplicado y luego se derivó una ecuación de amplitud. Esta ecuación corresponde a una generalización de la ecuación de Ginzburg-Landau con un término anisotrópico y forzamiento espacial.

En el segundo capítulo la ecuación anisotrópica de Ginzburg-Landau fue estudiada, caracterizando la solución tipo vórtice. Dos tipos de vórtices positivos fueron identificados. Se calculó la energía de estas soluciones y se mostró cómo intercambian estabilidad a través de una bifurcación transcrítica degenerada dependiente del parámetro anisotrópico. Se caracterizó el vórtice negativo perturbativamente y se calculó su energía numéricamente.

En el tercer capítulo se realizó un análisis numérico de la ecuación anisotrópica forzada de Ginzburg-Landau. Se mostró cómo el forzamiento induce un sólo vórtice positivo en el centro del voltaje aplicado, lo que nos permitió comprender las observaciones experimentales. Este mecanismo de anclaje nos permitió concebir la posibilidad de crear redes programables de vórtices con una configuración espacial arbitraria. Esto fue experimentalmente confirmado usando una adecuada configuración de la LCLV. Posteriormente, se adaptó nuestra ecuación para considerar diferentes rayos de luz, lo que mostró numéricamente redes de vórtices en concordancia con las observaciones experimentales.

En el último capítulo se estudió la dinámica de dislocaciones en un patrón anisotrópico. Se derivó una ecuación de amplitud enmendada para la ecuación anisotrópica de Swift-Hohenberg. En esta ecuación de amplitud, las dislocaciones aparecen como vórtices cuya dinámica fue caracterizada, permitiendo predecir la existencia de pares de dislocaciones estacionarios, lo que fue confirmado numéricamente.

Los resultados obtenidos en esta tesis muestran que las singularidades de fase son un fenómeno omnipresente en la naturaleza, que pueden ser descritas en una manera unificada mediante ecuaciones de amplitud. A su vez, estas ecuaciones pueden relacionarse con el contexto físico específico, cerca de sus puntos críticos.

RESUMEN DE LA TESIS PARA OPTAR AL
GRADO DE: Magíster en Ciencias, mención Física
POR: Estefania Vidal Henríquez
FECHA: 06/03/2014
PROFESOR GUÍA: Marcel Clerc Gavilán

PHASE SINGULARITY DYNAMICS IN OUT OF EQUILIBRIUM ANISOTROPIC SYSTEMS

This thesis is devoted to the study of phase singularities in the context of self-organization in out of equilibrium systems. Our study was focalized on understanding the emergence of vortices in a nematic liquid crystal light valve (LCLV) with homeotropic anchoring illuminated by a gaussian beam. This physical system allows the creation of optical vortices that are self-induced and self-aligned, along with the induction of positive vortices in the liquid crystal texture.

In the first chapter a model equation for this system was derived from first principles. First, the electric field in the system was analysed and then, an amplitude equation was derived. This equation corresponds to a generalization of the well-know Ginzburg-Landau Equation with an anisotropic term and a spatial forcing.

In the second chapter the Anisotropic Ginzburg-Landau Equation was studied characterizing its vortex solutions. Two different types of positive vortices were identified. The energy of these solutions was calculated and it was shown how they exchange stability through a Degenerated Transcritical Bifurcation that depends on the anisotropic parameter. The negative vortex was characterized perturbatively and its energy calculated numerically.

In the third chapter numerical analysis of the Forced Anisotropic Amplitude Equation was performed. It was shown how the forcing parameter induces one single positive vortex in the center of the applied voltage which allows us to understand the experimental observations. This pinning mechanism allow us to envisage the possibility to create programmable vortex lattices with arbitrary spatial configuration. This was experimentally confirmed using an adequate configuration in a LCLV. Furthermore, adapting our equation to account for different light rays showed numerical vortex lattices in quite good agreement with the experimental observations.

In the last chapter the dislocation dynamics in an anisotropic pattern were studied. To do this an Amended Amplitude Equation for the Anisotropic Swift-Hohenberg Equation was derived, in this amplitude equation dislocations show up as vortices whose dynamic was characterized, allowing the prediction of stationary dislocation pairs, which were confirmed numerically.

The results obtained in this thesis showed that phase singularities are an ubiquitous phenomena in nature, which can be described in a unified way by amplitude equations. In turn, these equations can be related to the particular physical context close to its critical points.

To my parents.

Contents

List of Figures

Chapter 1

Introduction

1.1 Pitchfork Bifurcation

To introduce dynamical systems we will begin with a simple example: The Andronov's Pendulum [2]. Consider a ring of radius R rotating at a constant angular velocity ω like in Figure 1.1, in this ring there is a particle of mass m that can slide along the border of the ring, subject to viscous drag and gravitational pull.
In spherical coordinates this system is described by

$$mR\ddot{\theta} = -b\dot{\theta} - mg\sin(\theta) + mR\omega^2\sin(\theta)\cos(\theta),$$

where θ is the angle between the pendulum and the vertical axis, and b is a damping coefficient.We can rewrite this equation more clearly as

$$mR\ddot{\theta} + b\dot{\theta} = mg\sin(\theta)\left(\frac{R\omega^2}{g}\cos(\theta) - 1\right),$$

it is easy to see that the system has a stationary solution $\sin(\theta) = 0$, i.e $\theta = \{0, \pi\}$ but it also has the solution $\cos(\theta) = g/R\omega^2$ which only exists when $g/R\omega^2 < 1$, note that due to symmetry this last solution corresponds to two values of θ.

Let's analyse the stability of the solution $\theta = 0$ by taking $\theta = \varepsilon$ and linearizing in ε, we then get

$$mR\ddot{\varepsilon} + b\dot{\varepsilon} = mg\varepsilon\left(\frac{R\omega^2}{g} - 1\right),$$

here we can see that the solution $\theta = 0$ is only stable when $R\omega^2/g < 1$ or equivalently when $g/R\omega^2 > 1$, this means that this solution is stable only while the other solutions do not exist.
Now we analyse the stability of $\theta = \pi$ by takin $\theta = \pi + \varepsilon$ and linearizing in ε, we obtain

$$mR\ddot{\varepsilon} + b\dot{\varepsilon} = -mg\varepsilon\left(-\frac{R\omega^2}{g} - 1\right),$$

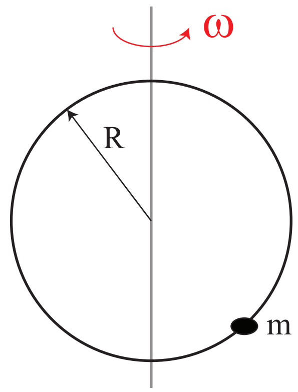

Figure 1.1: Andronov's Pendulum.

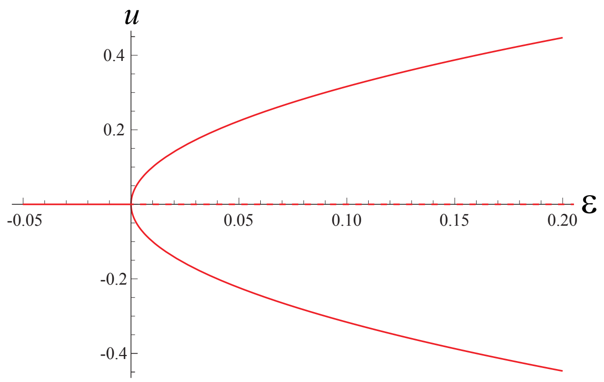

Figure 1.2: Bifurcation diagram for the Pitchfork Bifurcation. The dashed line represents an unstable solution, while the continuous line represents a stable one.

therefore the solution $\theta = \pi$ is always unstable. Finally we analyse the stability of $\cos(\theta) = g/R\omega^2$ by taking $\theta = \theta^* + \varepsilon$ where $\theta^* = \cos^{-1}(g/R\omega^2)$, we get

$$mR\ddot{\varepsilon} + b\dot{\varepsilon} = mg(\sin(\theta^*) + \cos(\theta^*)\varepsilon)\left(\frac{R\omega^2}{g}(\cos(\theta^*) - \sin(\theta^*)\varepsilon - 1\right),$$

linearizing in ε and using that $\theta^* = \cos^{-1}(g/R\omega^2)$ we get

$$mR\ddot{\varepsilon} + b\dot{\varepsilon} = -mg\sin^2(\theta^*)\varepsilon,$$

therefore this solution is stable regardless of the value of $\sin(\theta^*)$, which means that both possible values of θ^* are stable, when they exist.

The phenomenon that the solution $\theta = 0$ undergoes, when a solution changes its stability, is called a *bifurcation* [12, 36], particularly, in this case when a solution loses stability and two new stable solutions appear, it is called a *Supercritical Pitchfork Bifurcation* and it is common in systems with reflection symmetry. The bifurcation diagram for this kind of instability is shown in Figure 1.2, where solutions are represented by lines, continuous if they are stable or dashed if they are unstable. The simplest system that presents this bifurcation is [13]

$$\partial_t u = \mu u - u^3, \tag{1.1}$$

here we recognize the bifurcation parameter μ, the bifurcation that occurs at $\mu = 0$, and the reflection symmetry $u \to -u$. This equation is an example of an *Amplitude Equation*, which

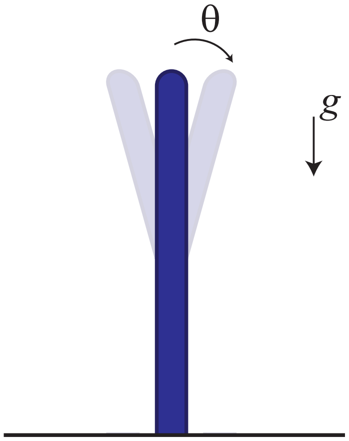

Figure 1.3: Euler's elastica in one dimension.

are equations that describe the behavior of a system close to a bifurcation [17].

Another natural example to describe such bifurcation is an elastic rod subjected to gravitational pull, like is shown in Figure 1.3. A simple model to describe this system is

$$I\ddot{\theta} = mlg\sin\theta - \kappa\theta,$$

where I stands for the rod inertia, θ is the angle deviation from the vertical, m is the rod mass, l its length, and κ an elastic constant. Approximating for small angle values we obtain

$$I\ddot{\theta} = (mgl - \kappa)\theta - \frac{mgl\theta^3}{3}.$$

This equation can easily be rearranged into the normal form Equation 1.1 by simply taking $\mu = (mgl - \kappa)/I$ and then scaling θ. Therefore this system presents the same phenomenology already discussed.

1.2 Degenerated Pitchfork Bifurcation

If now we try to imagine this bifurcation in a two dimension variable instead of just one, the system must have rotational invariance instead of just reflection symmetry, for example we can imagine the same vertical rod subject to gravitational pull, fixed in its base. If the rod is short it can stay straight, but if the rod is too long it will inevitable bend, but now because of the rotational symmetry, the rod can bend in any direction, or, in cylindrical coordinates, in any angle between 0 and 2π, as is schematically shown in Figure 1.4. Just like in the one dimensional case the competition between gravity pull and internal elasticity would account for the bifurcation parameter and how much the rod bends would correspond to the amplitude in the Amplitude Equation. The instability presented here is an example of a *Degenerated Pitchfork Bifurcation* which is schematically represented in Figure 1.5.

To describe a system such as this one we will need to introduce a complex parameter A

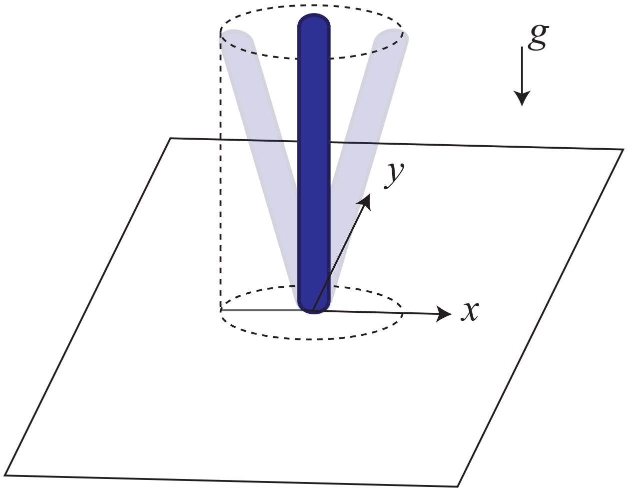

Figure 1.4: Euler's elastica in two dimensions.

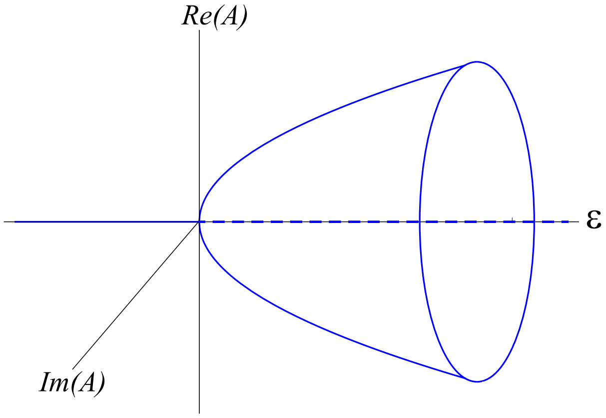

Figure 1.5: Bifurcation diagram for the Degenerated Pitchfork Bifurcation.

to take into account the two necessary directions, this way the real part of A can represent the deviation of the rod in the x-axis, and the imaginary part, the deviation in the other, perpendicular, y-axis. We will call this parameter A, *order parameter*, a concept that was first introduced by Ginzburg and Landau in the context of phase transitions [37]. This order parameter is usually a combination of the relevant fields in a particular system, in a way that important changes in the system can be easily visualized as changes in the order parameter. The equation that this parameter satisfies is the simplest equation that describes this kind of dynamic and it is "isomorphic" to other systems with the same dynamic through an adequate variable change [17] . For our example above, the system when the rod is straight is described with $A = 0$ and with the rod bending can be simply described with $|A| \neq 0$. The Amplitude Equation that describes this type of bifurcation is the following normal form

$$\partial_t A = \varepsilon A - |A|^2 A.$$

Continuing with our description of more complex systems that present similar bifurcations we can promote our variable to a field, considering now an extended system. First in 1-D,

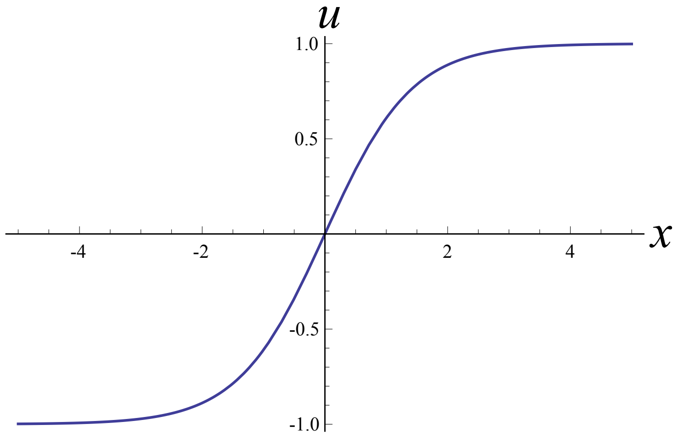

Figure 1.6: Kink solution for Eq.1.2 with $\varepsilon = 1$. This state connects the solutions $u = \sqrt{\varepsilon}$ and $u = -\sqrt{\varepsilon}$.

let's consider

$$\partial_t u = \varepsilon u - u^3 + \partial_{xx} u, \tag{1.2}$$

here we have a system similar to Eq.1.1, because it also presents the symmetry $u \to -u$. In this equation there are two symmetrical homogeneous solutions, when $\varepsilon > 0$, $u = \sqrt{\varepsilon}$ and $u = -\sqrt{\varepsilon}$, these solutions are both stable and have the same energy.

Because of initial conditions or fluctuations these two solutions can exist in different locations in the system simultaneously, these different locations are called *domains*. When this happens the two solutions need to be connected in a smooth way, this is accomplished through the *Kink Solution*, $u = \sqrt{\varepsilon}\tanh(x\sqrt{\varepsilon/2})$ which is shown in Figure 1.6. Due to the symmetry of the system, the analogous *Antikink* also exists $u = -\sqrt{\varepsilon}\tanh(x\sqrt{\varepsilon/2})$. If more than one kink (or antikink) exists in the system, they will attract if they are of different type, or repel if they are of the same type, in order to minimize the total free energy. This way, when two kinks of different type collide they annihilate leaving a homogeneous solution in the system, which is the global energy minimum.

More generically when the amplitude magnitude in an Amplitude Equation goes to zero that point is known as a *Defect*, because it breaks the translational invariance symmetry, these defects are very common in dynamical systems where some kind of symmetry exists. Defects present a very rich dynamic and will be the center of the following chapters. Finally, as a last step in raising the complexity of the system we will gather all the elements previously mentioned, considering the 2-D bifurcation in an extended system, the *Ginzburg-Landau Equation* with real coefficients

$$\partial_t A = \varepsilon A - |A|^2 A + \nabla^2 A,$$

the system above presents the previously mentioned Degenerated Pitchfork Bifurcation when $\varepsilon = 0$, which means that the homogeneous state $A = \sqrt{\varepsilon}\mathrm{e}^{\mathrm{i}\phi_0}$ can take any value of ϕ_0, or, if we imagine a polar representation of A in the plane, the arrow can take any direction as long as it has the appropriate size. And, just like in the example above, the system can take different directions in different zones. If there are two different directions (values of ϕ_0) in the system, they are connected through a wall solution $A = \mathrm{e}^{\mathrm{i}\phi_0}\sqrt{\varepsilon}\tanh(x\sqrt{\varepsilon/2})$, which is very similar to a kink, but extended, and therefore it is known as an extended defect, since there are infinite

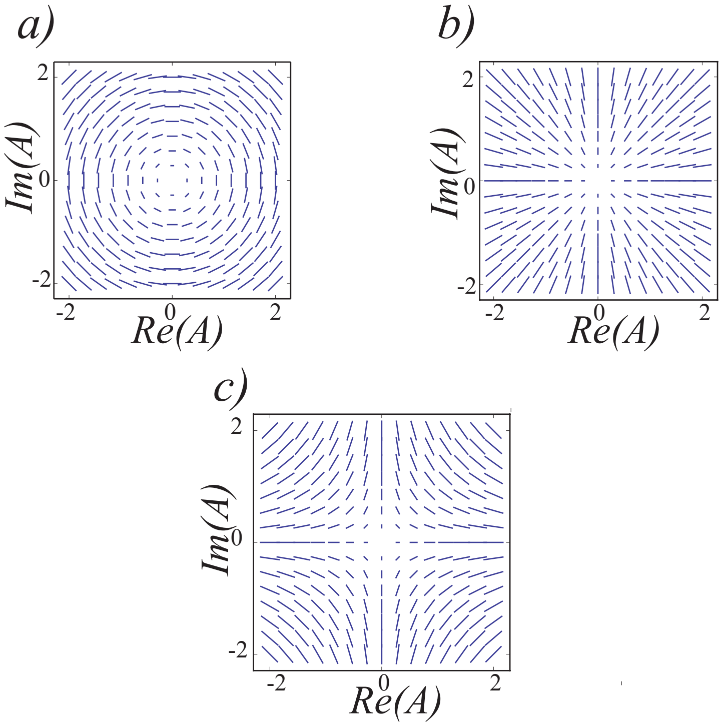

Figure 1.7: Different vortex solutions for the Ginzburg-Landau Equation. a) and b) show vortex of charge $m = +1$, while c) represent a vortex of charge $m = -1$.

points where the amplitude becomes zero.

This system also has localized defects, which occur when there are at least three different directions expressed locally in the system. In this case these different orientations are smoothly connected through a defect known as *Vortex* which is characterized by having a phase singularity in the point where the Amplitude goes to zero (See Figure 1.7). This singularity is described through its *charge* m [32], defined by

$$\oint_{\Gamma} \nabla\varphi = 2\pi m$$

where φ is the phase of A in the polar representation, and the path Γ encircles the vortex. This equation allows charges with $m \in \mathbb{Z}$ for the phase to be well defined. Some vortices are depicted in Figure 1.7, where b) simply is a rotation in $\pi/2$ of a) in order to show that there is an infinite number of vortices due to the rotational invariance of the system. The vortex solution is studied in depth in Chapter 3.

1.3 Liquid Crystals

Liquid Crystals are materials that have local position and/or orientation correlation, but not at large distances, thus allowing them to flow and also to present crystal-like properties [10, 25, 30]. They have been a great source of interest since their discovery in 1888 by

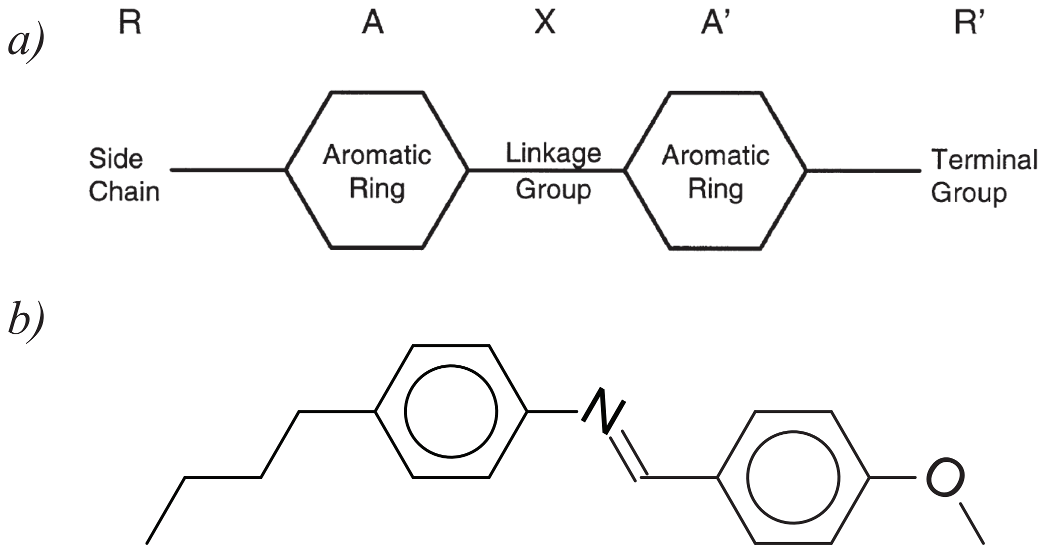

Figure 1.8: a) Molecular structure of a typical liquid crystal. After [25]. b) Molecular structure of MBBA (N-(4-Methoxybenzylidene)-4-butylaniline)

Friedrich Reinitzer due to their optical properties, which has spiked their use in technological applications, the most widely known being the Liquid Crystal Display (LCD) [38].

Liquid Crystals may appear in different phases depending on temperature, straining conditions, and the particular properties of the chemical compound, among other reasons. The three principal phases: nematic, cholesteric, and smectic; were classified by Friedel in 1922 [20], and even though since then several other phases have been reported, thanks to the discovery of new materials, this classification remains useful as a first approach [16]. The Nematic phase has the least order amount and highest symmetry, presenting only orientational order of the long molecular axis. The Cholesteric phase is similar to the Nematic in that it only presents orientational order, but with a chirality, meaning that it has a macroscopic helical structure. Finally, the smectic phase besides orientational order it also has positional order, thus having molecules ordered in layers [10, 30].
In particular we will be interested in nematic liquid crystals due to the experimental setup that motivates this work (see Section 2.1), the molecules in this case are usually elongated with a rod-like shape, as shown in Figure 1.8, which allows us to define the director vector $\vec{n}(\vec{r})$ that describes the average molecule position in the liquid crystal. Since the molecules are cuadripolar this vector has the symmetry $\vec{n} = -\vec{n}$, or in other words "it does not have an arrowhead".

Liquid crystals are a highly dissipative medium whose dynamic is characterized by minimizing their elastic energy, which was first described by Frank in 1958 [18]. In nematic materials there are three principal distinct director axis deformations: twist, splay, and bend; which are depicted in Figure 1.9, each of these deformations has its own elastic constant,

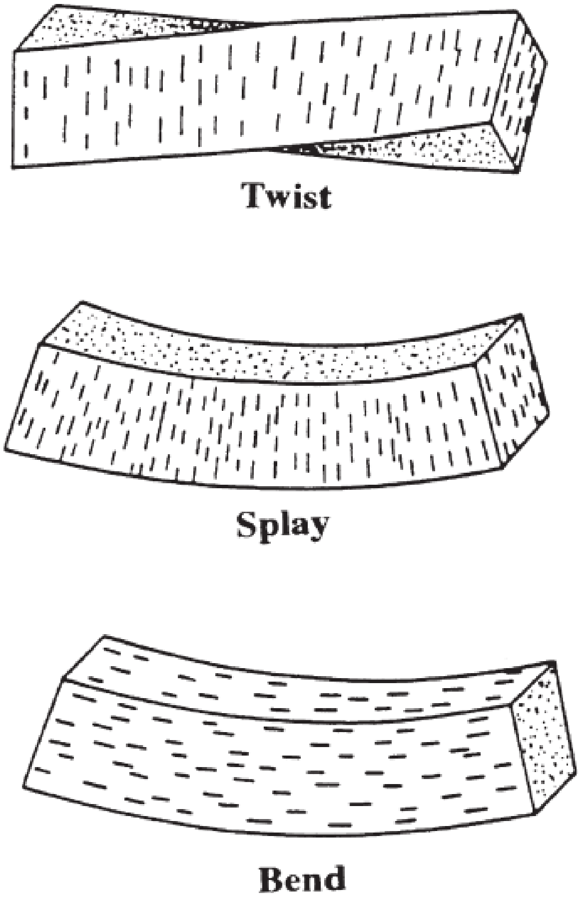

Figure 1.9: Principal deformations on a Nematic Liquid Crystal: Twist, Bend, and Splay. After [25]

giving rise to the Frank Free energy density

$$F = \frac{K_1}{2}(\nabla \cdot \vec{n})^2 + \frac{K_2}{2}(\vec{n} \cdot (\nabla \times \vec{n}))^2 + \frac{K_3}{2}(\vec{n} \times (\nabla \times \vec{n}))^2,$$

where K_1 corresponds to the splay deformation, K_2 to the twist deformation, and K_3 to the bend one. If the sample of liquid crystal is subject to electric or magnetic fields, then those energy densities are added accordingly. These constants are usually of the order of 10^{-6} dyne, for example for MBBA (Figure 1.8 b)) their values are 5.8×10^{-7}, 3.4×10^{-7}, and 7×10^{-7} dyne, for K_1, K_2, and K_3, respectively.

Chapter 2

Vortex Induction

2.1 Experimental Setup

One of the first reported experiences in liquid crystals was the observation of *schlieren textures* under crossed polarizers [26, 20]. This texture can occur in different configurations, particularly it occurs when a nematic mixture of liquid crystal is sandwiched between two glass plates that have been treated to provide an homeotropic anchoring to the molecules, this forces the molecules to be perpendicular to the glass plates. These plates have usually a surface of about $1-5cm^2$, while the separation between the plates is $5-50\mu m$, this provides a large area to observe the effects. Due to this anchoring and the elasticity of the material, the molecules inside the sample align themselves perpendicular to the glass plates, therefore if the sample is observed between crossed polarizers it appears black, since the light is not refracted inside the sample after it crosses the first polarizer and is cancelled by the second one.

If the material has a negative dielectric constant ε_a ($\varepsilon_a = \varepsilon_\| - \varepsilon_\perp$), then when a voltage is applied to the plates, the molecules will tend to align perpendicular to the electric field in order to reduce their energy. This electric force opposes the elasticity if there is homeotropic anchoring, therefore, for low voltages nothing happens and the sample remains dark, but if the voltage is increased a transition occurs at a voltage known as *Freedericksz Voltage* [19] and a schlieren texture as in Figure 2.1 appears. This transition is a *Degenerated Pitchfork Bifurcation* (see Section 1.1), where the molecules leave the vertical axis in an angle that depends on the magnitude of the voltage, but there is a cone of possible equilibrium positions for the molecules, therefore different directions are taken in different places in the sample. The dark lines observed correspond to the places where the molecules align with one of the polarizers, and the intersection of these lines correspond to the positions where the molecules remain perpendicular to the plates. These points are a kind of defect known mostly in the liquid crystal community as *umbilics*, these defects move through the sample and disappear by colliding among them or by reaching the boundaries of the sample.

The setup above described is very well known to experimentalists and also has been properly described by theory [7], particularly the dynamics of these defects. Because of the above

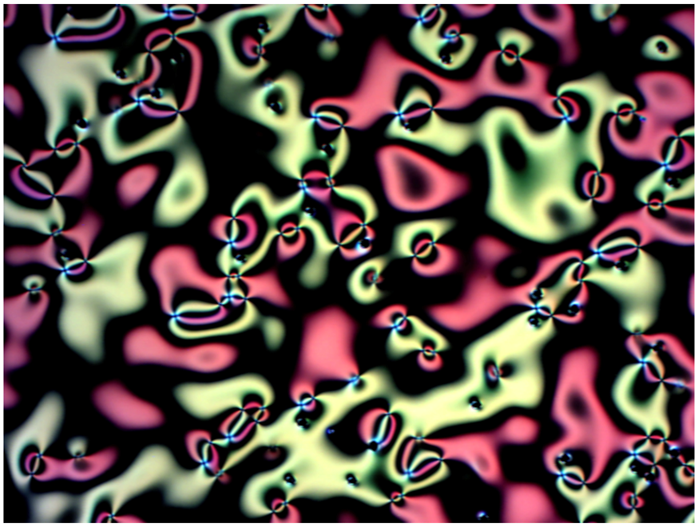

Figure 2.1: Schlieren texture in a sample of MBBA.

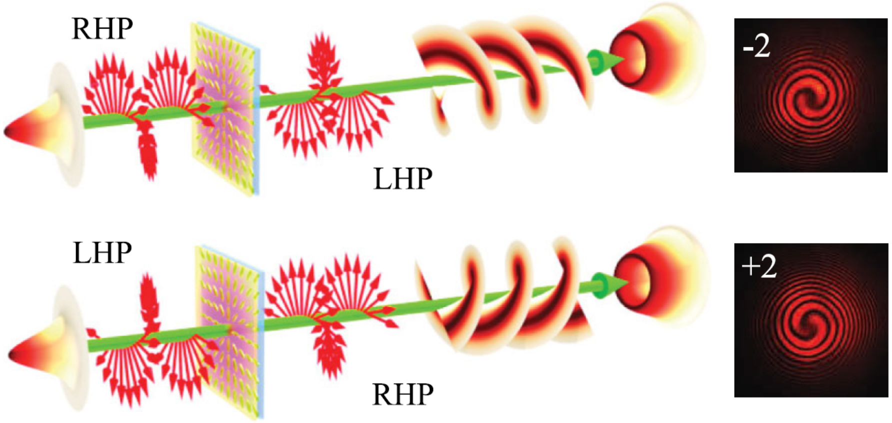

Figure 2.2: Schematic representation of the creation mechanism for optical vortices. Taken after [6].

mentioned, vortices are very difficult to control, since they appear everywhere in the sample and quickly move and disappear. A novel method to control vortices was reported in [5], where the setup is very similar to the one previously described, with the difference that one of the glass plates is replaced with a slab of a transparent photoconductor and the sample is held at a voltage lower than critical. Then, with the aid of a Spacial Light Modulator (SLM) a laser is directed to the photoconductor. The area illuminated by the laser is around $250\mu m$, this causes an additional voltage drop between the plates in the illuminated area. This allows the voltage in this area of the sample to rise above the critical voltage. In this area one single umbilical defect is created, and is always close to the center of the illuminated area, has a +1 charge, and remains fixed in that position.

The possibility of having one controlled vortex allows the creation of *Gauss-Laguerre* modes in the light once it has crossed the sample, as it is described in [5] and shown in Figure 2.2. These modes correspond to an optical vortex, light modes with a singularity at their center that carry angular momentum. They have several technological applications [39] and this method of creation guaranties the correct alignment between the light ray and the phase singularity.

From this point forward we will concentrate on understanding this isolated umbilical structure, why it appears, remains stable, and its characteristics. We begin by analysing the shape of the electric field inside the sample.

2.2 Electric Field Inside the Valve

The light that illuminates the Liquid Crystal Light Valve (LCLV) is a Gaussian beam, since this is the natural shape the light acquires when it travels through a medium (it is the solution to the paraxial equation [24]), which means that the voltage induced in the plate is not uniform, but bell-shaped. In order to calculate the electric field inside the cell we modeled the cell as two infinite planar parallel plates separated by a distance d in the z axis, where the photoconductor is in $z = \mathrm{d}$ and has a gaussian-shaped voltage drop, and the other plate is taken as reference (see Figure 2.4), thus the boundary conditions are

$$V(z,r) = V(z=\mathrm{d}) = V_0 + \alpha I(r),$$

$$V(z,r) = V(z=0) = 0,$$

where $I(r)$ is proportional to the light intensity that illuminates the sample and has a gaussian profile, $I(r) = I_0 \mathrm{e}^{-r^2/\omega^2}$, where I_0 is the intensity peak and ω is the waist of the beam.

Introducing cylindrical coordinates centered at the center of the gaussian beam, the voltage satisfies the anisotropic Laplace equation of the form

$$\partial_{zz} V + \frac{\varepsilon_\perp}{\varepsilon_\parallel} \nabla_\perp^2 V = 0;$$

where $\nabla_\perp^2 V$ is the laplacian in the transversal coordinates, $\varepsilon_\perp$ is the dielectric constant of the liquid crystal for the perpendicular electrical field and $\varepsilon_\parallel$ is the dielectric constant for the parallel one. Using the Fourier transform in the plane parallel to the plates we obtain the Fourier transform of the voltage

$$\widetilde{V}(z,k) = \frac{1}{\sqrt{2\pi}} \int_{-\infty}^{\infty} \mathrm{e}^{\mathrm{i}k\cdot r_\perp} V(z, r_\perp) \mathrm{d}r_\perp,$$

and for the laplacian equation we get

$$\partial_{zz}\widetilde{V} - \frac{\varepsilon_\perp}{\varepsilon_\parallel} k^2 \widetilde{V} = 0.$$

For the boundary condition $V(z=0) = 0$ we get that its Fourier transform is also zero, this way we retain only the odd modes of the solution, obtaining

$$\widetilde{V}(z,k) = A(k) \frac{\sinh\left(\sqrt{\frac{\varepsilon_\perp}{\varepsilon_\parallel}} kz\right)}{\sinh\left(\sqrt{\frac{\varepsilon_\perp}{\varepsilon_\parallel}} k\mathrm{d}\right)},$$

now to impose the other boundary condition we need to revert to the coordinate space using the inverse Fourier transform

$$V(z,r) = \frac{1}{\sqrt{2\pi}} \int_{-\infty}^{\infty} \mathrm{d}k \mathrm{e}^{-\mathrm{i}k\cdot r_\perp} A(k) \frac{\sinh\left(\sqrt{\frac{\varepsilon_\perp}{\varepsilon_\parallel}} kz\right)}{\sinh\left(\sqrt{\frac{\varepsilon_\perp}{\varepsilon_\parallel}} k\mathrm{d}\right)}, \tag{2.1}$$

and considering $z = \mathrm{d}$, we impose the boundary condition at the photoconductor.

$$V(\mathrm{d},r) = V_0 + \alpha I(r/\omega) = \frac{1}{\sqrt{2\pi}} \int_{-\infty}^{\infty} \mathrm{d}k \mathrm{e}^{-\mathrm{i}k\cdot r_\perp} A(k) \tag{2.2}$$

then using again the Fourier transform we obtain

$$A(k) = \frac{1}{\sqrt{2\pi}} \int_{-\infty}^{\infty} \mathrm{d}r_\perp \mathrm{e}^{\mathrm{i}k\cdot r_\perp} (V_0 + \alpha I(r_\perp/\omega)). \tag{2.3}$$

Replacing (2.3) in (2.1) we obtain the solution to the initial equation with the previously mentioned boundary conditions

$$V(z,r) = \frac{1}{2\pi} \int_{-\infty}^{\infty} \mathrm{d}k \mathrm{e}^{-\mathrm{i}k\cdot r_\perp} \frac{\sinh\left(\sqrt{\frac{\varepsilon_\perp}{\varepsilon_\parallel}} kz\right)}{\sinh\left(\sqrt{\frac{\varepsilon_\perp}{\varepsilon_\parallel}} k\mathrm{d}\right)} \left(\int_{-\infty}^{\infty} \mathrm{d}r_\perp^* \mathrm{e}^{\mathrm{i}k\cdot r_\perp^*} [V_0 + \alpha I(r_\perp^*/\omega)]\right)$$

We can now renormalize the variables using the width ω of the gaussian beam: $p = r^*/\omega$, $q = k\omega$, and obtain

$$V(z,r) = \frac{1}{2\pi} \int_{-\infty}^{\infty} \mathrm{d}q \mathrm{e}^{-\mathrm{i}q\cdot r_\perp/\omega} \frac{\sinh\left(\sqrt{\frac{\varepsilon_\perp}{\varepsilon_\parallel}} qz/\omega\right)}{\sinh\left(\sqrt{\frac{\varepsilon_\perp}{\varepsilon_\parallel}} q\mathrm{d}/\omega\right)} \left(\int_{-\infty}^{\infty} \mathrm{d}p \mathrm{e}^{\mathrm{i}q\cdot p} [V_0 + \alpha I(p)]\right).$$

This is the explicit solution of the Laplace Equation, however due to its complexity it is difficult to obtain intuitive results form it. Thus, we will consider a limit where we can figure out the effect of the photoconductor in the LCLV.

In the limit where the gaussian beam is very flat (very wide)($\omega \to \infty$) we can make the approximation

$$\frac{\sinh\left(\sqrt{\frac{\varepsilon_\perp}{\varepsilon_\parallel}} qz/\omega\right)}{\sinh\left(\sqrt{\frac{\varepsilon_\perp}{\varepsilon_\parallel}} q\mathrm{d}/\omega\right)} \approx \frac{z}{\mathrm{d}} + \mathcal{O}\left(\frac{1}{\omega^2}\right),$$

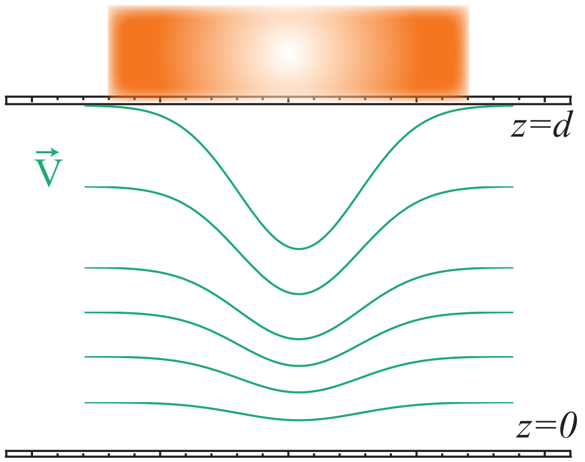

Figure 2.3: Voltage inside the Liquid Crystal Light Valve.

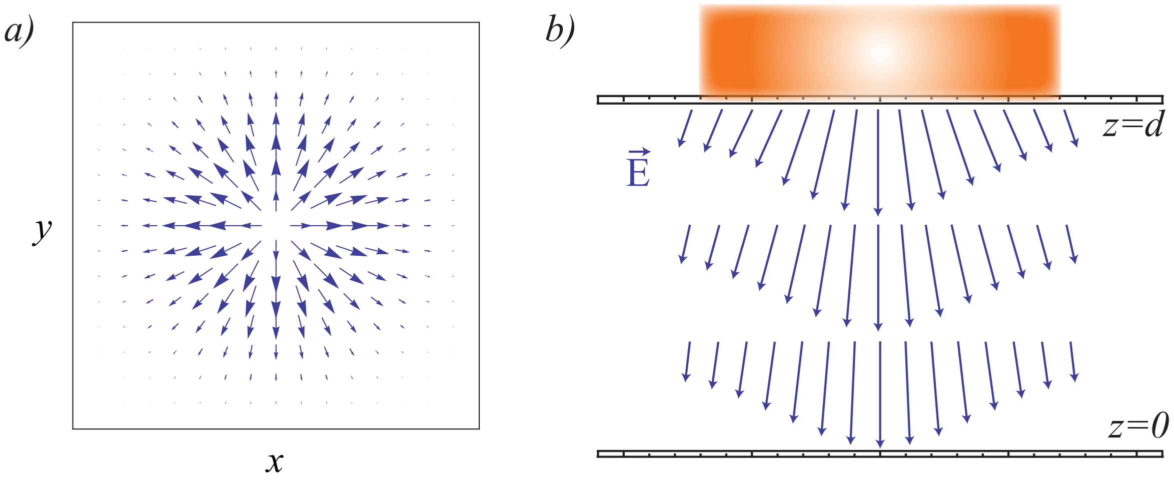

Figure 2.4: a) Top view and b) lateral cut view of the electromagnetic field inside the Liquid Crystal Light Valve.

this approximation is plausible because the gaussian beam is large compared to the size of a vortex in the liquid crystal. Using the previous approximation we get

$$V(z,r) \approx \frac{z}{\mathrm{d}}\frac{1}{2\pi}\int_{-\infty}^{\infty}\int_{-\infty}^{\infty}\mathrm{d}q\mathrm{d}p\mathrm{e}^{\mathrm{i}q(p-r/\omega)}(V_0+\alpha I(p)) = \frac{z}{\mathrm{d}}\int_{-\infty}^{\infty}\mathrm{d}p\delta(p-r/\omega)(V_0+\alpha I(p)),$$

solving the integral we obtain the voltage inside the valve at first order

$$V(z,r) \approx \frac{z}{\mathrm{d}}(V_0+\alpha I(r/\omega)).$$

This solution is shown in Figure 2.3 and corresponds to a gaussian profile that progressively losses strength as we move away from the incoming light beam.

Finally we obtain the electric field inside the valve using $E = -\nabla V = -\frac{\partial V}{\partial r}\widehat{r} - \frac{1}{r}\frac{\partial V}{\partial \theta}\widehat{\theta} - \frac{\partial V}{\partial z}\widehat{z}$

$$\boxed{E = \frac{-1}{\mathrm{d}}(V_0+\alpha I(r/\omega))\widehat{z} - \frac{z}{\mathrm{d}\omega}\alpha I'(r/\omega)\widehat{r}}$$

The electromagnetic field inside the LCLV is shown schematically in Figure 2.4 were we can appreciate the radial component and the vortex-like shape of the field due to the gaussian light profile. Hence we deduced that the light produces, by means of the photoconductor, an electric field with a vortex structure inside the valve.

2.3 Amplitude Equation Derivation

2.3.1 Linear Analysis

To describe the position of the liquid crystal inside the Light Valve we consider the director vector $\vec{n}(x,y)$ with $|\vec{n}| = 1$, which corresponds to the average position of the molecules at (x,y) and since it has a relaxation dynamic we begin with the system Frank-Oseen Free Energy Density [10]

$$F = \frac{K_1}{2}(\nabla\cdot\vec{n})^2 + \frac{K_2}{2}(\vec{n}\cdot(\nabla\times\vec{n}))^2 + \frac{K_3}{2}(\vec{n}\times(\nabla\times\vec{n}))^2 - \frac{\varepsilon_a}{2}(E\cdot\vec{n})^2.$$

The first three terms correspond to the elastic energy contribution (See Section 1.3) and the last one to the interaction with the electric field. The nonlinearities in this problem arise when we minimize the free energy while maintaining the norm of the director, thus we must consider

$$\gamma\frac{\mathrm{d}\vec{n}}{\mathrm{d}t} = -\frac{\delta F}{\delta\vec{n}}$$

with the restriction $|\vec{n}| = 1$, which is equivalent to

$$\gamma\frac{\mathrm{d}\vec{n}}{\mathrm{d}t} = -\frac{\delta F}{\delta\vec{n}} + \vec{n}\left(\vec{n}\cdot\frac{\delta F}{\delta\vec{n}}\right),$$

thus we obtain the following equation for the director [21]

$$\begin{aligned}\gamma\frac{\mathrm{d}\vec{n}}{\mathrm{d}t} = \; & K_3[\nabla^2\vec{n} - \vec{n}(\vec{n}\cdot\nabla^2\vec{n})] + (K_3-K_1)[\vec{n}(\vec{n}\cdot\nabla)(\nabla\cdot\vec{n}) - \nabla(\nabla\cdot\vec{n})]\\ & +(K_2-K_3)[2(\vec{n}\cdot\nabla\times\vec{n})(\vec{n}(\vec{n}\cdot\nabla\times\vec{n}) - \nabla\times\vec{n}) + \vec{n}\times\nabla(\vec{n}\cdot\nabla\times\vec{n})]\\ & -\varepsilon_a(\vec{n}\cdot\vec{E})(\vec{n}(\vec{n}\cdot\vec{E}) - \vec{E}),\end{aligned}$$

where $\varepsilon_a < 0$. We first find the point in the parameter space where the homeotropic position destabilizes due to the effect of the electric field, by doing a linear analysis, we set $\vec{n} = (u, v, 1-(u^2+v^2)/2)$ where u, v are small perturbations. Retaining the leading order we obtain

$$\gamma\dot{u} = K_3\partial_{zz}u - \varepsilon_a E^2 u,$$

$$\gamma\dot{v} = K_3\partial_{zz}v - \varepsilon_a E^2 v,$$

we now take an ansatz consistent with the homeotropic boundary conditions, $u = v = 0$ in $z = 0$ and $z = \mathrm{d}$, and find when it destabilizes. Thus we take a perturbation of the form $u = v = \mathrm{e}^{\sigma t}\sin(kz)$ with $k = \pi n/\mathrm{d}$, and obtain

$$\gamma\sigma = -K_3k^2 - E^2\varepsilon_a,$$

this shows the growing rate σ for all wavelengths, but only the ones mentioned before can appear in the system, of these the one that first destabilizes is $k_c = \pi/\mathrm{d}$. Solving for the electrical field, we obtain

$$E^2 = \frac{-K_3 k^2}{\varepsilon_a} = \frac{-K_3 \pi^2 n^2}{\mathrm{d}^2 \varepsilon_a},$$

then the minimum value of the field that causes movement in the molecules is for $n = 1$

$$E = \sqrt{\frac{-K_3 \pi^2}{\varepsilon_a \mathrm{d}^2}},$$

and thus obtaining the critical voltage, *Freedericksz Voltage* [19], $V_F = \sqrt{-K_3\pi^2/\varepsilon_a}$. This corresponds to the point were the electric force on the molecules is able to overcome the elastic force that tries to maintain the molecules perpendicular to the glass plates and thus, tilt the molecules in any possible direction like in the rod in Figure 1.5, therefore a Degenerated Pitchfork Bifurcation occurs at this voltage. This bifurcation is particularly useful to experimentally determine the value of K_3, since it is relatively easy to localize. To understand the liquid crystal dynamics close to the bifurcation we will perform a weakly nonlinear analysis.

2.3.2 Weakly Nonlinear Analysis

We can now set the voltage close to this critical value and perform a weakly nonlinear analysis, where we assume the deviation from the homeotropic state is small. We suppose

$$n = \begin{pmatrix} n_1 \\ n_2 \\ 1 - \dfrac{n_1^2 + n_2^2}{2} \end{pmatrix}$$

and neglecting higher orders in the radial electric field we obtain:

$$\begin{aligned}
\gamma \dot{n}_1 = K_3[\nabla^2 n_1 + n_1((\partial_z n_1)^2 + (\partial_z n_2)^2)] - (K_3 - K_1)[n_1 \partial_{zz}(n_1^2 + n_2^2)/2 + \partial_{xx} n_1 + \partial_{xy} n_2] \\
+(K_2 - K_3)[-\partial_{xy} n_2 + \partial_{yy} n_1] - \varepsilon_a n_1 E_z^2 (1 - n_1^2 - n_2^2) \\
-\varepsilon_a (2n_1^2 E_z E_x + 2n_1 n_2 E_z E_y - E_x E_z (1 - n_1^2/2 - n_2^2/2)),
\end{aligned}$$

$$\begin{aligned}
\gamma \dot{n}_2 = K_3[\nabla^2 n_2 + n_2((\partial_z n_1)^2 + (\partial_z n_2)^2)] - (K_3 - K_1)[n_2 \partial_{zz}(n_1^2 + n_2^2)/2 + \partial_{xy} n_1 + \partial_{yy} n_2] \\
+(K_2 - K_3)[\partial_{xx} n_2 - \partial_{xy} n_1] - \varepsilon_a n_2 E_z^2 (1 - n_1^2 - n_2^2) \\
-\varepsilon_a (2n_2^2 E_z E_y + 2n_1 n_2 E_z E_x - E_y E_z (1 - n_1^2/2 - n_2^2/2));
\end{aligned}$$

where the last terms correspond to the corrections due to the radial field. We now consider the ansatz $n_1 = X \sin(k_c z) + W_1, n_2 = Y \sin(k_c z) + W_2$ which describes the amplitude of the first unstable mode ($k_c = \pi/\mathrm{d}$), and $\overrightarrow{W} = (W_1, W_2)$ stands for higher order corrections, using $k = k_c$ to simplify notation, we then obtain

$$
\begin{aligned}
\gamma\dot{X}\sin(kz) = \;& (K_3\partial_{zz} - \varepsilon_a E_z^2)W_1 + K_3\sin(kz)[\nabla_\perp X - k^2X + k^2X(X^2+Y^2)\cos^2(kz)] \\
& -(K_3-K_1)\sin(kz)[Xk^2(X^2+Y^2)(\cos^2(kz)-\sin^2(kz)) + \partial_{xx}X + \partial_{xy}Y] \\
& +(K_2-K_3)\sin(kz)[\partial_{yy}X - \partial_{xy}Y] \\
& -\varepsilon_a X\sin(kz)E_z^2(1-(X^2+Y^2)\sin^2(kz)) \\
& +\varepsilon_a E_xE_z - \varepsilon_a\sin^2(kz)[2X^2E_zE_x + 2XYE_zE_y + E_xE_z(X^2+Y^2)/2],
\end{aligned}
$$

$$
\begin{aligned}
\gamma\dot{Y}\sin(kz) = \;& (K_3\partial_{zz} - \varepsilon_a E_z^2)W_2 + K_3\sin(kz)[\nabla_\perp Y - k^2Y + k^2Y(X^2+Y^2)\cos^2(kz)] \\
& -(K_3-K_1)\sin(kz)[Yk^2(X^2+Y^2)(\cos^2(kz)-\sin^2(kz)) + \partial_{xy}X + \partial_{yy}Y] \\
& +(K_2-K_3)\sin(kz)[\partial_{xx}Y - \partial_{xy}X] \\
& -\varepsilon_a Y\sin(kz)E_z^2(1-(X^2+Y^2)\sin^2(kz)) \\
& +\varepsilon_a E_yE_z - \varepsilon_a\sin^2(kz)[2Y^2E_zE_y + 2XYE_zE_x + E_yE_z(X^2+Y^2)/2].
\end{aligned}
$$

The linear operator acting on W is

$$
\mathcal{L} = \begin{pmatrix} K_3\partial_{zz} - \varepsilon_a E_z^2 & 0 \\ 0 & K_3\partial_{zz} - \varepsilon_a E_z^2 \end{pmatrix},
$$

if we define the inner product $\langle f|g\rangle = \int_0^{\mathrm{d}} f\cdot g$ this operator is self-adjoint and its kernel is $Ker\{\mathcal{L}^\dagger\} = \{(\sin(kz),0),(0,\sin(kz))\}$, we now use the Freedholm alternative projecting our system onto the kernel elements of the adjoint operator and considering that E_z is independent of z we obtain

$$
\begin{aligned}
\gamma\dot{X} = \;& K_3[\nabla_\perp X - k^2X + k^2X(X^2+Y^2)/4] \\
& -(K_3-K_1)[(\partial_{xx}X + \partial_{xy}Y) - Xk^2(X^2+Y^2)/2] + (K_2-K_3)[\partial_{yy}X - \partial_{xy}Y] \\
& -\varepsilon_a XE_z^2(1-3(X^2+Y^2)/4) + \varepsilon_a E_z\frac{2}{\mathrm{d}}\int_0^{\mathrm{d}} E_x\sin(kz)\mathrm{d}z \\
& -\frac{2}{\mathrm{d}}\varepsilon_a E_z[2X^2\int_0^{\mathrm{d}} E_x\sin(kz)^3\mathrm{d}z + 2XY\int_0^{\mathrm{d}} E_y\sin(kz)^3\mathrm{d}z \\
& +\frac{X^2+Y^2}{2}\int_0^{\mathrm{d}} E_x\sin(kz)^3\mathrm{d}z],
\end{aligned}
$$

$$
\begin{aligned}
\gamma\dot{Y} = \;& K_3[\nabla_\perp Y - k^2Y + k^2Y(X^2+Y^2)/4] \\
& -(K_3-K_1)[(\partial_{xy}X + \partial_{yy}Y) - Yk^2(X^2+Y^2)/2] + (K_2-K_3)[\partial_{xx}Y - \partial_{xy}X] \\
& -\varepsilon_a YE_z^2(1-3(X^2+Y^2)/4) + \varepsilon_a E_z\frac{2}{\mathrm{d}}\int_0^{\mathrm{d}} E_y\sin(kz)\mathrm{d}z \\
& -\frac{2}{\mathrm{d}}\varepsilon_a E_z[2Y^2\int_0^{\mathrm{d}} E_y\sin(kz)^3\mathrm{d}z + 2XY\int_0^{\mathrm{d}} E_x\sin(kz)^3\mathrm{d}z \\
& +\frac{X^2+Y^2}{2}\int_0^{\mathrm{d}} E_y\sin(kz)^3\mathrm{d}z].
\end{aligned}
$$

Using that the radial field has a linear dependence on z we get

$$\begin{aligned}
\gamma\dot{X} = \; & K_3[\nabla_\perp X - k^2 X + k^2 X(X^2+Y^2)/4] \\
& -(K_3-K_1)[(\partial_{xx}X + \partial_{xy}Y) - Xk^2(X^2+Y^2)/2] + (K_2-K_3)[\partial_{yy}X - \partial_{xy}Y] \\
& -\varepsilon_a X E_z^2(1-3(X^2+Y^2)/4) + \varepsilon_a \frac{2\mathrm{d}}{\pi z} E_x E_z \\
& -\varepsilon_a E_z \frac{4\mathrm{d}}{3\pi z}[2X^2 E_x + 2XYE_y + E_x(X^2+Y^2)/2],
\end{aligned}$$

$$\begin{aligned}
\gamma\dot{Y} = \; & K_3[\nabla_\perp Y - k^2 Y + k^2 Y(X^2+Y^2)/4] \\
& -(K_3-K_1)[(\partial_{xy}X + \partial_{yy}Y) - Yk^2(X^2+Y^2)/2] + (K_2-K_3)[\partial_{xx}Y - \partial_{xy}X] \\
& -\varepsilon_a Y E_z^2(1-3(X^2+Y^2)/4) + \varepsilon_a \frac{2\mathrm{d}}{\pi z} E_y E_z \\
& -\varepsilon_a E_z \frac{4\mathrm{d}}{3\pi z}[2Y^2 E_y + 2XYE_x + E_y(X^2+Y^2)/2].
\end{aligned}$$

Rewriting with the help of the complex parameter $A = X + \mathrm{i}Y$ and defining $\partial_\eta = \partial_x + \mathrm{i}\partial_y$, $\mu = -K_3k^2 - \varepsilon_a E_z^2$, and $a = (2K_1k^2 - 3\varepsilon_a E_z^2)/4$ we get

$$\begin{aligned}
\gamma\partial_t A = \mu A + \frac{K_1+K_2}{2}\nabla^2 A + \frac{K_1-K_2}{2}\partial_{\eta\eta}\overline{A} - aA|A|^2 \\
+ \varepsilon_a \frac{2\mathrm{d}}{\pi}\frac{E_r(z)}{z}E_z \mathrm{e}^{\mathrm{i}\theta} - \varepsilon_a E_z \frac{4\mathrm{d}}{3\pi}\frac{E_r(z)}{z}\left(2ARe(A\mathrm{e}^{-\mathrm{i}\theta}) + \frac{|A|^2\mathrm{e}^{\mathrm{i}\theta}}{2}\right),
\end{aligned}$$

finally dropping the smaller corrections and scaling, time, space, and the parameter A we obtain

$$\boxed{\partial_t A = \mu A + \nabla^2 A + \delta\partial_{\eta\eta}\overline{A} - A|A|^2 + b\frac{E_r(z)}{z}E_z\mathrm{e}^{\mathrm{i}\theta}}$$

where $\delta = (K_1 - K_2)/(K_1 + K_2)$ and $b = 2\varepsilon_a \mathrm{d}\sqrt{a}/\pi$. This is the *Forced Anisotropic Ginzburg-Landau Equation*, where μ is the bifurcation parameter, which accounts for the competition between the elastic and electric force, the second term corresponds to diffusion, which is a consequence of the elastic coupling, the fourth is the nonlinear saturation, the third is the anisotropic correction, a consequence of how the different deformations in the system have different energy, and the last corresponds to the forcing produced by the shape of the electric field inside the valve. Without forcing and anisotropy this equation corresponds to the *Ginzburg-Landau Equation* with real coefficients, a equation widely studied because of its importance in dynamical systems, as we have mentioned before. The properties of the *Anisotropic Ginzburg-Landau Equation* are studied in the following chapter.

It is noteworthy to mention that $\delta \in [-1, 1]$, the extreme cases occurring when one of the elastic constants (K_1 or K_2) diverges. This occurs when the liquid crystal goes through a phase transition from the nematic state to a smetic one, as can be seen in Figure 2.5.

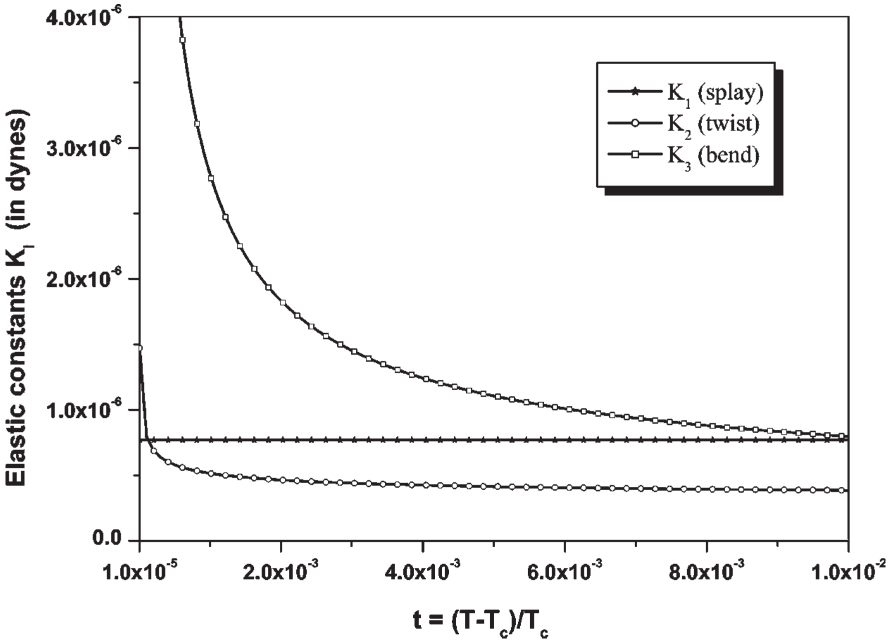

Figure 2.5: Elastic constants as a function of temperature in 8OCB in the vecinity of the Nematic - Smetic A transition. Experimental results by Madhusudana and Pratibha [27].

Chapter 3

Anisotropic Ginzburg-Landau Equation

To better understand the effects of both the anisotropy and the forcing in the *Ginzburg-Landau Equation* we will separate these effects, thus we now devote ourselves to the study of the *Anisotropic Ginzburg-Landau Equation*

$$\partial_t A = \mu A + \nabla^2 A + \delta \partial_{\eta\eta} \overline{A} - A|A|^2$$

with $\delta \neq 0$. This equation was first deduced in [21] for nematic liquid crystals and it has also been proposed for the self-assembly of microtubules and motors [4].

If $\delta = 0$ this is the well known *Ginzburg-Landau Equation* with real coefficients [22]. Before jumping into the anisotropic equation a quick overview of this isotropic model is necessary.

3.1 Ginzburg-Landau Equation with Real Coefficients

The *Complex Ginzburg-Landau Equation* appears in such different systems as fluids, superfluids, superconductors, granular matter, and liquid crystals. In 2-D this equation describes any stationary degenerate supercritical bifurcation [12], which appears in the most various systems that present vortices, understanding them as structures with zero amplitude and a phase discontinuity at their center, as has been presented in Section 1.1.
In particular we will be interested in the Ginzburg-Landau Equation with real coefficients that presents dissipative vortices in contraposition with the equation with pure imaginary coefficients that presents conservative vortices, which describes superfluids and superconductors, where it was first derived by Ginzburg and Pitaevskii [23]. For a complete review of this equation see Ref [3] and references therein. The Ginzburg-Landau Equation with real coefficients reads,

$$\partial_t A = \mu A + \nabla^2 A - A|A|^2. \tag{3.1}$$

It is important to mention that this equation has a Lyapunov functional $\mathcal{E}$ so that $\partial_t A =$

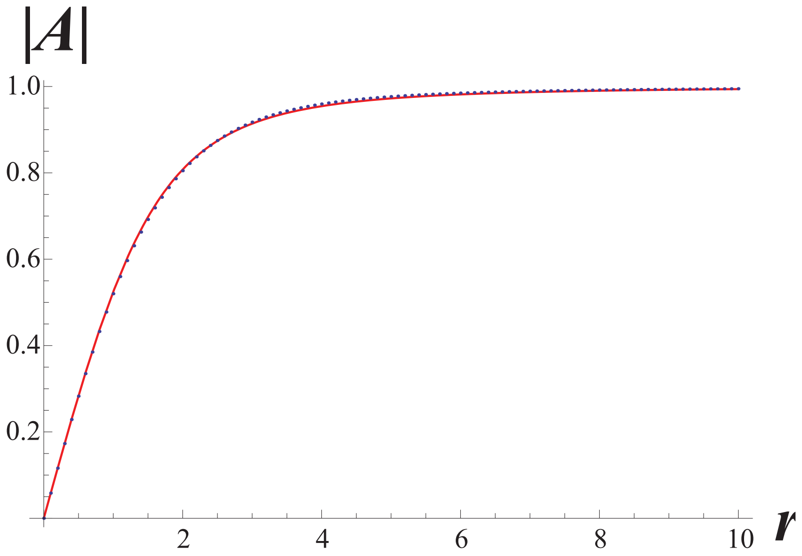

Figure 3.1: Numerical solution for the isotropic vortex profile R_v with $\mu = 1$ and charge $m = \pm 1$ in blue dots, Pade approximation in red continuous line.

$-\delta\mathcal{E}/\delta\overline{A}$, which means that the system is variational and has a relaxation dynamic, minimizing its free energy

$$\mathcal{E} = \int \left(-\mu |A|^2 + \frac{|A|^4}{2} + \nabla A \nabla \overline{A} \right) \mathrm{d}S,$$

where the minimal energy solution corresponds to the homogeneous one $A = \sqrt{\mu}\mathrm{e}^{\mathrm{i}\phi_0}$, where ϕ_0 is an arbitrary phase and thus this is a family of solutions parameterized by ϕ_0. This is a consequence of Equation 3.1 being phase invariant.

3.1.1 Vortex Solution

We now refer to the most studied and intricate particle type solution of this equation, the *Dissipative Vortex Solution.* A particle type solution is a localized solution parameterized by a set of continuous and discrete parameters such as position, width, and charge, to name a few.

We begin by looking for a stationary solution where the amplitude is axisymmetric and the phase grows continuously around the vortex, by taking $A = R(r)\mathrm{e}^{\mathrm{i}(m\theta+\theta_0)}$, where (r,θ) are polar coordinates and θ_0 is an arbitrary parameter, related to the symmetry of the system, that shows explicitly the position of the phase discontinuity or singularity. We obtain from 3.1

$$0 = \mathrm{e}^{\mathrm{i}(m\theta+\theta_0)} \left(\mu R - R^3 + \frac{\partial^2 R}{\partial r^2} + \frac{1}{r}\frac{\partial R}{\partial r} - \frac{m^2 R}{r^2} \right) \tag{3.2}$$

Unfortunately this equation does not have an analytic solution, however we can find its

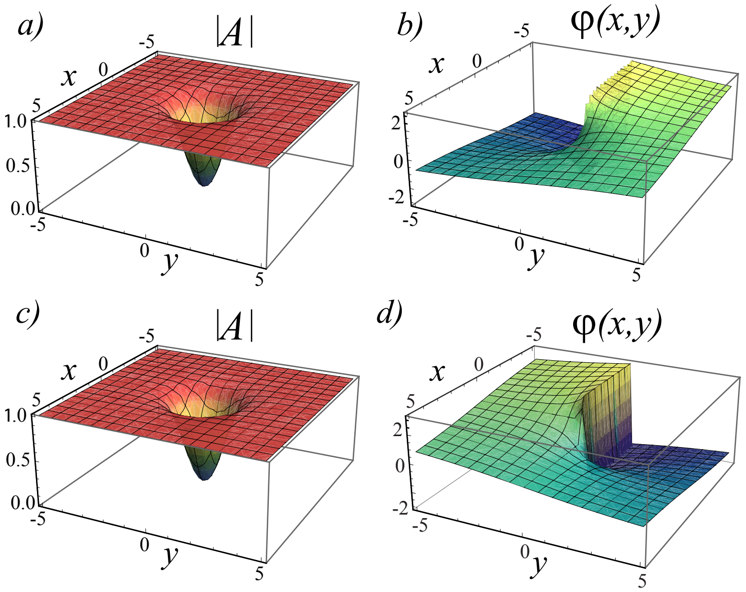

Figure 3.2: Numerical solution for the isotropic vortex with charge +1 and −1, Left: Amplitude, Right: Phase. a-b Positive Vortex, c-d Negative Vortex.

asymptotic behavior close to infinity and near to the origin.

$$R(r) \approx \begin{cases} \alpha_m r^{|m|} + \dots, & r \longrightarrow 0, \\ \sqrt{\mu} - \frac{m^2}{2} r^{-2} + \dots, & r \longrightarrow \infty, \end{cases}$$

where a_m is a positive constant that depends on μ. A good approximation developed by Pismen in [32] for $\mu = 1$ and charge $m = \pm 1$ in the form of a Pade approximation for the square of the amplitude magnitude is

$$R_v^2(r) \approx \frac{0.34r^2 + 0.07r^4}{1 + 0.42r^2 + 0.07r^4},$$

a numeric solution, also for $\mu = 1$ is shown in Figure 3.1 along with this approximation, showing quite good agreement. For different values of μ this approximation needs to be scaled as $R_\mu(r) = \sqrt{\mu} R_{\mu=1}(\sqrt{\mu} r)$. The complete 3D representation is shown in Figure 3.2. In order for the phase to be well defined we need $m \in \mathbb{Z}$, this is know as the vortex's *charge* or winding number. It is important to note that the amplitude of the vortex R_v does not depend on the sign of the charge, making them indistinguishable in the amplitude magnitude. Numerical simulations show that the only stable solutions are with $m = \pm 1$, all other charges are unstable.

Since this system minimizes its energy, we can calculate the energy $\mathcal{E}$ of the vortex, in order to simplify calculations we will use $\mu = 1$, without lose of generality, so we can rearrange the energy

$$\mathcal{E} = \frac{1}{2} \int \nabla A \nabla \overline{A} + \frac{1}{2} \left(1 - |A|^2\right)^2 \mathrm{d}S,$$

we now replace the vortex solution $A = R_v \mathrm{e}^{\mathrm{i} m \theta}$, where R_v corresponds to the profile of the vortex.

$$\mathcal{E} = \frac{1}{2} \int (\partial_r R_v)^2 + \frac{m^2 R_v^2}{r^2} + \frac{1}{2} \left(1 - R_v^2\right)^2 \mathrm{d}S,$$

since R_v depends only in the absolute value of m, we can see that the vortex energy only depends on the size of the charge and not on its sign. The first two terms in the energy are divergent in an infinite domain, so we will separate the energy in its diverging and finite parts and after we integrate in the angular dependence we obtain,

$$\mathcal{E}_1 = \pi \int_0^\infty \left((\partial_r R_v)^2 + \frac{m^2 R_v^2}{r^2} \right) r \mathrm{d}r$$

and

$$\mathcal{E}_2 = \frac{\pi}{2} \int_0^\infty \left(1 - R_v^2\right)^2 r \mathrm{d}r$$

respectively, $\mathcal{E}_2$ can be solved analytically using that R_v is the solution to Equation 3.2, to do this, first we integrate by parts

$$\mathcal{E}_2 = \pi \int_0^\infty \left(1 - R_v^2\right) R_v R_v' r^2 \mathrm{d}r$$

and now using Equation 3.2 we obtain

$$\mathcal{E}_2 = -\pi \int_0^\infty \left(r R_v' \frac{\mathrm{d}(r R_v')}{\mathrm{d}r} - m^2 R_v R_v' \right) \mathrm{d}r = \frac{\pi m^2}{2}.$$

Now, to calculate $\mathcal{E}_1$ we need to introduce a cut-off at a distance L because of the logarithmic divergency, that is, we consider the vortex in a domain of finite size. The result depends on a numerical constant a_0 that depends on the solution R_v, i.e. the specific shape of the vortex core, obtaining $\mathcal{E}_1 = \pi m^2 \ln L/a_0 > 0$, we then get

$$\mathcal{E}(Vortex) = \pi m^2 \left(\ln \frac{L}{a_0} + \frac{1}{2} \right) = \pi m^2 \ln \left(\frac{L\sqrt{\mathrm{e}}}{a_0} \right)$$

This tells us that vortices with charge $m = \pm 1$ are stable, result that has been confirmed numerically, the other charges being unstable. Still, this solution has more energy that the uniform state $A = \sqrt{\mu}$, and in order for the energy to reach its minimum the vortices must disappear by colliding between them or by reaching the boundaries of the system.

Since the vortex structure in two dimensions occurs in the intersection between two nullclines (lines where a field goes to zero, in this case, the fields $Im(A)$ and $Re(A)$) they are topologically stable solutions. This is because the only way an intersection of continuous lines in 2-D can disappear by continuously deforming them is through the collision with another intersection of the same lines. Any other deformation of the nullclines will only move the intersection but it will not make it disappear. This explains why vortices only annihilate with other vortices, or with the boundaries of the system.

The basis of this collision mechanism was described by Bodenschatz, et al. in Ref [9], vortices with same sign charge repel, and vortices with different sign attract. This kinematic law is given in Ref [9] and Ref [34].

$$v \ln \left(\frac{v}{v_0} \right) = \frac{q}{r}$$

where v_0 is a constant, v is the vortex velocity, and q sign depends whether the interaction is attraction or repulsion. This interaction acts at very large distances (long range interaction), since it has a polynomial decay, which makes particularly difficult the task of isolating a single pair of vortices. Recently, by means of a LCLV a pair of vortices have been isolated and this interaction has been characterized [7].

3.2 Anisotropic Ginzburg-Landau Equation

We now look to perform a similar analysis for the anisotropic equation

$$\partial_t A = \mu A + \nabla^2 A + \delta \partial_{\eta\eta} \overline{A} - A|A|^2.$$

This equation has lost the independent rotational symmetries $A \rightarrow A\mathrm{e}^{\mathrm{i}\theta}$ and $z \rightarrow z\mathrm{e}^{\mathrm{i}\theta}$ with $\theta \in (0, 2\pi)$, where z are the coordinates, retaining only the simultaneous symmetry $A(z) \rightarrow \mathrm{e}^{-\mathrm{i}\theta} A(z\mathrm{e}^{\mathrm{i}\theta})$

Just like its isotropic counterpart, the Anisotropic Ginzburg-Landau Equation has a relaxation dynamic given by $\partial_t A = -\delta\mathcal{E}_{\mathcal{A}}/\delta\overline{A}$, where, taking $\mu = 1$, the energy reads

$$\mathcal{E}_{\mathcal{A}} = \frac{1}{2}\int \nabla A \nabla \overline{A} + \frac{1}{2}(1 - |A|^2)^2 + \delta Re\{(\partial_\eta \overline{A})^2\} \mathrm{d}S,$$

where the minimum energy solution is the uniform state $A = 1$ with $\mathcal{E}_{\mathcal{A}}(A = 1) = 0$. Another uniform solution easy to see is the uniform state $A = 0$ which is unstable with $\mathcal{E}_{\mathcal{A}}(A = 0) = 1/2$.

This equation also has solutions in the form of domain walls

$$A(x, y) = \sqrt{\mu} \tanh \sqrt{\frac{\mu}{2(1+\delta)}} x, \;\; A(x, y) = \sqrt{\mu} \tanh \sqrt{\frac{\mu}{2(1-\delta)}} y,$$

these solutions are less common than the vortex solution and are harder to observe experimentally. They are unstable giving rise to vortices on their core, in the presence of noise.

3.3 Positive Vortex Solution in Anisotropic Ginzburg-Landau

Numerical simulations have shown that the vortex solutions are persistent when $\delta \neq 0$, therefore, we now devote ourselves to the study of this solution. We begin with the same Ansatz as before, imposing a positive charge $m = +1$ in the vortex $A = R(r)\mathrm{e}^{\mathrm{i}(\theta+\theta_0)}$ we obtain

$$0 = \mu R - R^3 + (1 + \delta \mathrm{e}^{-2\mathrm{i}\theta_0}) \left(R'' + \frac{R'}{r} - \frac{R}{r^2} \right)$$

where the imaginary part implies

$$0 = \delta \sin 2\theta_0 \left(R'' + \frac{R'}{r} - \frac{R}{r^2} \right),$$

then $\sin 2\theta_0 = 0$, giving the solutions

$$\theta_0 = \{0, \frac{\pi}{2}, \pi, \frac{3\pi}{2}\}.$$

For the real part we obtain

$$0 = \mu R - R^3 + (1 + \delta \cos 2\theta_0) \left(R'' + \frac{R'}{r} - \frac{R}{r^2} \right),$$

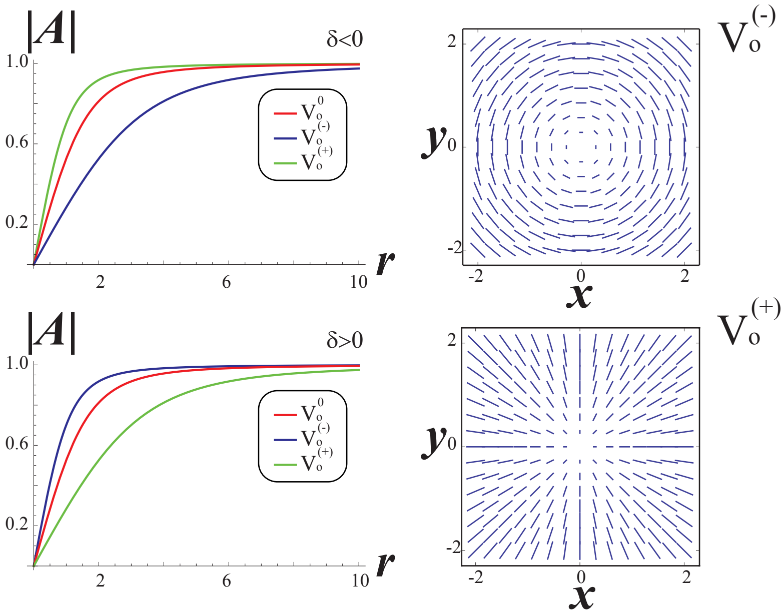

Figure 3.3: Left: Vortex profile of the two anisotropic positive vortices. Right: Top view of both vortices.

where the isotropic solution is recovered by scaling the space

$$R(r) = R_v\left(\frac{r}{\sqrt{1+\delta\cos 2\theta_0}}\right).$$

Then, the positive vortex solution can be summed up as

$$\boxed{A = R_v\left(\frac{r}{\sqrt{1\pm\delta}}\right)\mathrm{e}^{\mathrm{i}\left(\theta+\frac{\pi}{4}\mp\frac{\pi}{4}+n\pi\right)}}$$

with $n = 0, 1$.We will refer to these solutions as $V_0^{(+)}$ and $V_0^{(-)}$ for the solution with $\theta_0 = 0$ and $\theta_0 = \pi/2$, respectively. These solutions are shown in Figure 3.3, where we notice that even though the difference in the amplitude is only a scaling, the orientation of the molecules (right side) is significatively different. Note that the anisotropic system has a discrete number of solutions, in contrast with the isotropic system, which has an infinite number of solutions parameterized by a continuous parameter. These solutions are two positive vortices, one whose core is bigger than the isotropic one, and one whose core is smaller (see Figure 3.3).

We now follow the same procedure as before to characterize the energy of these vortices.

We can evaluate the energy of the system $\mathcal{E}_{\mathcal{A}}$

$$\mathcal{E}_{\mathcal{A}} = \frac{1}{2}\int \nabla A\nabla\overline{A} + \frac{1}{2}(1-|A|^2)^2 + \delta\mathrm{Re}\{(\partial_\eta\overline{A})^2\}\mathrm{d}S,$$

using $A = R_A(r)\mathrm{e}^{\mathrm{i}(\theta+\theta_0)}$, where R_A is the profile of the anisotropic vortex, i.e. a scaling of R_v, we then obtain

$$\mathcal{E}_{\mathcal{A}} = \frac{1}{2}\int (\partial_r R_A)^2 + \frac{R_A^2}{r^2} + \frac{1}{2}(1-R_A^2)^2 + \delta\cos(2\theta_0)\left(\partial_r R_A + \frac{R_A}{r}\right)^2\mathrm{d}S.$$

Unfortunately, just like in the isotropic case, the two first terms and also the last term of the above expression are infinite, this is solved by introducing a cut-off at $r = L$ with L much larger than the core size.

$$\mathcal{E}_{\mathcal{A}} = \pi \int_0^L (\partial_r R_A)^2 + \frac{R_A^2}{r^2} + \frac{1}{2}(1 - R_A^2)^2 + \delta \cos(2\theta_0) \left(\partial_r R_A + \frac{R_A}{r} \right)^2 r \mathrm{d}r,$$

using the scaling of the isotropic solution and changing variables we obtain

$$\begin{aligned} \mathcal{E}_{\mathcal{A}} =& \pi \int_0^{L/\sqrt{1\pm\delta}} (\partial_\rho R_v(\rho))^2 + \frac{R_v^2(\rho)}{\rho^2} + \frac{(1\pm\delta)(1 - R_v^2(\rho))^2}{2} \\ & \pm \delta \left(\partial_\rho R_v(\rho) + \frac{R_v(\rho)}{\rho} \right)^2 \rho \mathrm{d}\rho, \end{aligned}$$

similarly to the isotropic case we will separate this expression in its diverging, finite and anisotropic parts. Respectively

$$\mathcal{E}_{\mathcal{A}1} = \pi \int_0^{L/\sqrt{1\pm\delta}} (\partial_\rho R_v(\rho))^2 + \frac{R_v^2(\rho)}{\rho^2} \rho \mathrm{d}\rho,$$

$$\mathcal{E}_{\mathcal{A}2} = \frac{\pi(1\pm\delta)}{2} \int_0^{L/\sqrt{1\pm\delta}} (1 - R_v^2(\rho))^2 \rho \mathrm{d}\rho,$$

and

$$\mathcal{E}_{\mathcal{A}3} = \pm\delta\pi \int_0^{L/\sqrt{1\pm\delta}} \left(\partial_\rho R_v(\rho) + \frac{R_v(\rho)}{\rho} \right)^2 \rho \mathrm{d}\rho.$$

We can see that $\mathcal{E}_{\mathcal{A}1}$ corresponds to the term $\mathcal{E}_1$ in the isotropic case, but with a cutoff in $L/\sqrt{1\pm\delta}$ instead of in L, thus we obtain $\mathcal{E}_{\mathcal{A}1} = \pi \ln(L/a_o\sqrt{1\pm\delta})$.
For $\mathcal{E}_{\mathcal{A}2}$ we simply notice that $\mathcal{E}_{\mathcal{A}2} = (1\pm\delta)\mathcal{E}_2 = \pi(1\pm\delta)/2$. Finally for $\mathcal{E}_{\mathcal{A}3}$ we can simplify the expression

$$\mathcal{E}_{\mathcal{A}3} = \pm\delta\pi \int_0^{L/\sqrt{1\pm\delta}} \left((\partial_\rho R_v(\rho))^2 + \frac{R_v^2(\rho)}{\rho^2} + \frac{2R_v'(\rho)R_v(\rho)}{\rho} \right) \rho \mathrm{d}\rho,$$

here we notice that the first two terms correspond to $\mathcal{E}_{\mathcal{A}1}$ and that the last one is an exact derivative

$$\mathcal{E}_{\mathcal{A}3} = \pm\delta\mathcal{E}_{\mathcal{A}1} \pm \delta\pi \int_0^{L/\sqrt{1\pm\delta}} \partial_\rho[R_v^2(\rho)] \mathrm{d}\rho = \pm\delta\pi(\ln(L/a_o\sqrt{1\pm\delta}) + 1).$$

Regrouping all these terms we obtain the energy of the positive anisotropic vortex

$$\mathcal{E}_{\mathcal{A}} = \pi \ln\left(\frac{L}{a_0\sqrt{1\pm\delta}} \right) + \frac{\pi(1\pm\delta)}{2} \pm \pi\delta \left(\ln\left(\frac{L}{a_0\sqrt{1\pm\delta}} \right) + 1 \right),$$

$$\mathcal{E}_{\mathcal{A}} = (1\pm\delta)\pi \ln\left(\frac{L\sqrt{\mathrm{e}}}{a_0\sqrt{1\pm\delta}} \right) \pm \delta\pi, \tag{3.3}$$

where the ± sign stands for + for $\theta_0 = \{0, \pi\}$ and − for $\theta_0 = \{\pi/2, 3\pi/2\}$. This shows that the scaling that makes the core smaller is the one with less energy and, therefore, preferred by

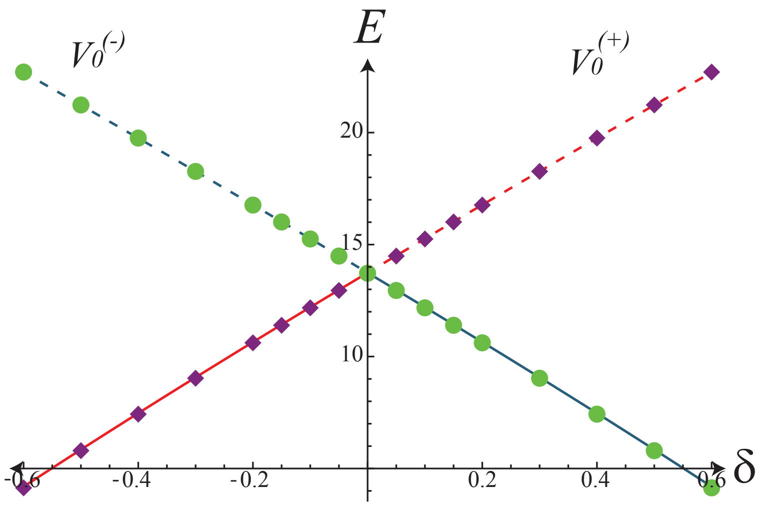

Figure 3.4: Numerical calculations (diamonds and circles) and theoretical prediction (continuous and dashed lines) for the energy of both positive vortex. The continuous line indicates a stable vortex, while the dashed one indicates an unstable one.

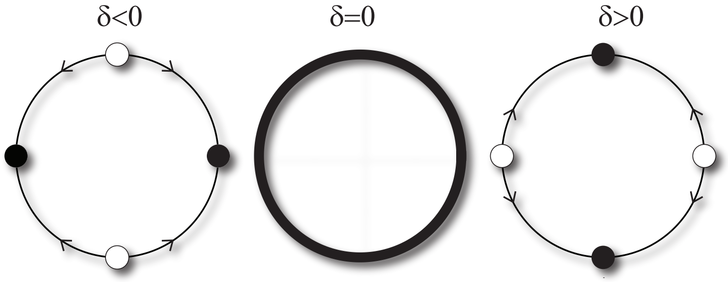

Figure 3.5: Bifurcation Diagram for the *Degenerated Transcritical Bifurcation* that the parameter θ_0 undergoes. The black circles represent stable solutions, while the white ones represent unstable ones.

the system. This way, if $\delta < 0$ ($\delta > 0$) the stable solution is the one with $\theta_0 = 0$ ($\theta_0 = \pi/2$). We understand this as the system prefers the homogeneous state (the minimal energy solution is $A = \sqrt{\mu}$) it reduces the vortex so its core occupies the least space, this way the homogeneous state occupies a bigger part of the system, therefore reducing the energy of the system even though the gradients are bigger in the smaller core than in the larger one.
The energy calculated numerically for different δ is shown in Figure 3.4 along with the theoretical prediction given by Equation (3.3), which shows quite good agreement, the stable and unstable vortices are shown with a continuous and dashed line, respectively.

3.3.1 Bifurcation Diagram

It has been shown that there are two degenerated positive vortex solutions that exist for every value of δ with $|\delta| < 1$. This solutions exchange stability at $\delta = 0$, where $\theta_0 = 0$ goes from stable to unstable, and viceversa for $\theta_0 = \pi/2$. The way these solutions exchange stability is not by the usual collision of solutions and exchange of stability of the *Transcritical Bifurcation* [36], but rather by passing through a very degenerated point at $\delta = 0$ where an infinite number of solutions exists (θ_0 can take any value between 0 and 2π) that connects

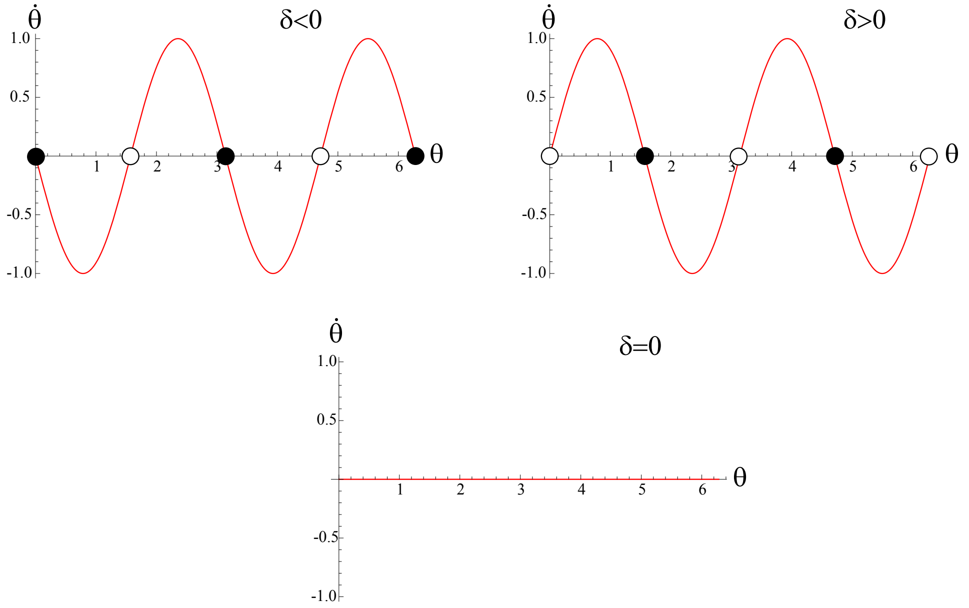

Figure 3.6: Simple dynamical system that also present a Degenerated Transcritical Bifurcation.

the existing ones. We call this bifurcation a ***Degenerated Transcritical Bifurcation*** and it is schematically shown in Figure 3.5.

To illustrate this type of instability we consider a prototype model that undergoes a similar bifurcation,

$$\dot{\theta} = \delta \sin(2\theta)$$

where the steady solutions are $\theta = \{0, \pi/2, \pi, 3\pi/2\}$ and exist for every value of δ. An analysis of the potential V,

$$\dot{\theta} = -\frac{\mathrm{d}V}{\mathrm{d}\theta}$$

with $V = \delta \cos(2\theta)/2$ indicates that the solutions $\theta = \{0, \pi\}$ are stable for $\delta < 0$ and unstable for $\delta > 0$. At $\delta = 0$, θ is solution $\forall \theta \in [0, 2\pi]$, and these solutions connect the already existent ones making the stability exchange possible, this system is shown in Figure 3.6. Therefore this system also has the bifurcation diagram shown in Figure 3.5, that is, this model exhibits a Degenerated Transcritical Bifurcation.

3.4 Negative Vortex Solution in Anisotropic Ginzburg-Landau

Due to the complexity of the equations for the negative vortex, a perturbatively approach will be used. We look for an approximate solution with negative charge for small δ, by inserting the following ansatz $A \approx [R_v(r) + \delta g(r, \theta)]\mathrm{e}^{-\mathrm{i}[\theta - \delta\Theta(r,\theta)]}$, where g and Θ are corrections to the isotropic negative vortex, and with the condition that Θ has no charge, ie

$$\oint_{\Gamma} \nabla\Theta \mathrm{d}l = 0$$

when the path Γ encircles the vortex core. Taking the leading order in δ we obtain

$$\begin{aligned}
0 =& \mathrm{e}^{-\mathrm{i}\theta}[\mu g - 3R_v^2 g + \frac{\partial^2 g}{\partial r^2} + 2\mathrm{i}\frac{\partial \Theta}{\partial r}\frac{\partial R_v}{\partial r} + \mathrm{i}R_v\frac{\partial^2 \Theta}{\partial r^2} + \frac{1}{r}\frac{\partial g}{\partial r} + \frac{\mathrm{i}R_v}{r}\frac{\partial \Theta}{\partial r} + \frac{1}{r^2}\frac{\partial^2 g}{\partial \theta^2} \\
&- \frac{2\mathrm{i}}{r^2}\frac{\partial g}{\partial \theta} + \frac{\mathrm{i}R_v}{r^2}\frac{\partial^2 \Theta}{\partial \theta^2} + \frac{2R_v}{r^2}\frac{\partial \Theta}{\partial \theta} - \frac{g}{r^2}] + \mathrm{e}^{3\mathrm{i}\theta}\left[\frac{\partial^2 R_v}{\partial r^2} + \frac{3R_v}{r^2} - \frac{3}{r}\frac{\partial R_v}{\partial r}\right],
\end{aligned}$$

separating the real and imaginary parts, the equations read

$$\begin{aligned}
0 =& \mu g - 3R_v^2 g + \frac{\partial^2 g}{\partial r^2} + \frac{1}{r}\frac{\partial g}{\partial r} + \frac{1}{r^2}\frac{\partial^2 g}{\partial \theta^2} + \frac{2R_v}{r^2}\frac{\partial \Theta}{\partial \theta} - \frac{g}{r^2} \\
&+ \cos(4\theta)\left[\frac{\partial^2 R_v}{\partial r^2} + \frac{3R_v}{r^2} - \frac{3}{r}\frac{\partial R_v}{\partial r}\right],
\end{aligned}$$

$$\begin{aligned}
0 =& 2\frac{\partial \Theta}{\partial r}\frac{\partial R_v}{\partial r} + R_v\frac{\partial^2 \Theta}{\partial r^2} + \frac{R_v}{r}\frac{\partial \Theta}{\partial r} - \frac{2}{r^2}\frac{\partial g}{\partial \theta} + \frac{R_v}{r^2}\frac{\partial^2 \Theta}{\partial \theta^2} \\
&+ \sin(4\theta)\left[\frac{\partial^2 R_v}{\partial r^2} + \frac{3R_v}{r^2} - \frac{3}{r}\frac{\partial R_v}{\partial r}\right],
\end{aligned}$$

the angular dependency is easily solved doing variable separation, by setting $g(r,\theta) = g_4(r)\cos(4\theta)$ and $\Theta(r,\theta) = \theta_4(r)\sin(4\theta)$, thus we obtain equations for the radial dependency

$$0 = \mu g_4 - 3R_v^2 g_4 + \frac{\partial^2 g_4}{\partial r^2} + \frac{1}{r}\frac{\partial g_4}{\partial r} - \frac{16 g_4}{r^2} + \frac{8R_v\theta_4}{r^2} - \frac{g_4}{r^2} + \frac{\partial^2 R_v}{\partial r^2} + \frac{3R_v}{r^2} - \frac{3}{r}\frac{\partial R_v}{\partial r}$$

$$0 = 2\frac{\partial \theta_4}{\partial r}\frac{\partial R_v}{\partial r} + R_v\frac{\partial^2 \theta_4}{\partial r^2} + \frac{R_v}{r}\frac{\partial \theta_4}{\partial r} + \frac{8 g_4}{r^2} - \frac{16 R_v\theta_4}{r^2} + \frac{\partial^2 R_v}{\partial r^2} + \frac{3R_v}{r^2} - \frac{3}{r}\frac{\partial R_v}{\partial r}.$$

At $r \to \infty$ this functions behave as follows

$$g_4(r) \sim \frac{9}{4r^2}, \theta_4(r) \sim \frac{3}{16}.$$

A numerical solution for g_4 is shown in Figure (3.7). The next important corrections to the modulus correspond to $g_8(r)\cos(8\theta)$ and to $g_{12}(r)\cos(12\theta)$, the amplitudes of these corrections are shown in Figure 3.8.

Unlike its positive counterpart, the negative vortex can have any value of the parameter θ_0, recovering the solution already obtained for $\theta_0 = 0$ by a simple rotation of the axis, obtaining

$$A \approx [R(r) + \delta g_4(r)\cos(4\theta - 2\theta_0)]\mathrm{e}^{\mathrm{i}(-\theta + \theta_0 + \delta\theta_4 \sin(4\theta - 2\theta_0))}.$$

All of these rotations have the same energy. Using numerical simulations we can calculate the energy $\mathcal{E}_{\mathcal{A}}$ of the negative vortex, this is presented in Figure 3.9. This energy is symmetrical with respect to the y axis, thus saying that $\mathcal{E}_{\mathcal{A}}$ depends only on $|\delta|$ within numerical error. From here we can also observe that the negative vortex always has more energy than the stable positive vortex, only being the same at $\delta = 0$. Nonetheless, the vortices always appear in pairs of opposite charge, in order to maintain the topological charge of the system. Hence, this model presents a mechanism of particle creation by pairs with opposite topological charge and different energies.

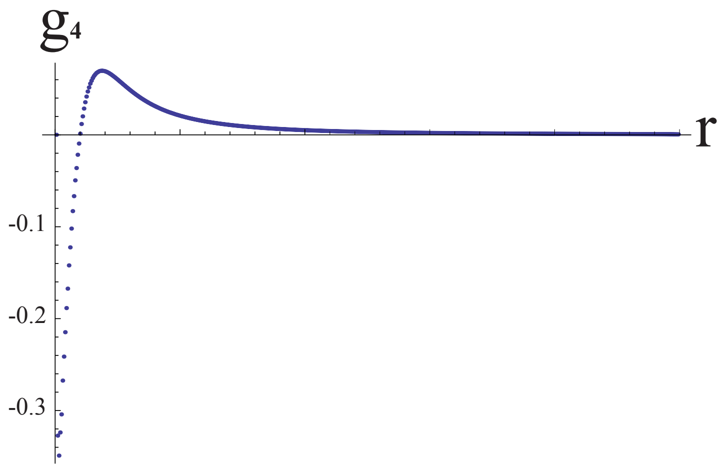

Figure 3.7: Numerical solution for the leading correction to the amplitude of the negative vortex.

3.5 Relation to Previous Results in Liquid Crystals

The idea that the positive and negative vortices are not identical is not new for experimentalists, who have known this for a while thanks to the use of different techniques, such as circular polarizers [28], measuring their different speeds at collision [15], or simply due to the different colors the vortices present under white light and crossed polarizers. However, very few attempts have been made to characterize them theoretically when the elastic constants are different. Remarkably in this group are the works of Saupe and Rapini, who obtained different properties of the anisotropic vortices using the Frank-Oseen free energy of liquid crystals.

Saupe and Nehring [29] found the vortex solutions by minimizing the volume integral over the energy density of the system and fixing the deviation of the director vector from the perpendicular axis, which translates in our model to maintaining the amplitude fixed, leaving only one degree of freedom, the phase φ, i.e. they looked for a *coreless* solution. Using this approximation they found that only integer charges are permitted. They also showed that after the one constant approximation ($K_1 = K_2 = K_3$ equivalent to $\delta = 0$) is dropped, only some of the positive vortex remain an exact solution of their model:

$$\varphi = \theta + n\frac{\pi}{2}$$

with $n \in \mathbb{Z}$, and $\varphi = 2\theta + \theta_0$. The first of these solutions corresponds to our findings of the positive vortex, that only some positions are permitted for the phase discontinuity, but they neglect the modified center in the structure of the amplitude. Their second solution is not valid in our model.

They also found an approximation for the other charges, linear in ε, a parameter that measures the anisotropy of the system, similar to our δ,

$$\varphi \approx m\theta + \theta_0 + \varepsilon\left(\frac{m(2-m)}{4(m-1)^2}\sin\left[2(\theta(m-1)+\theta_0)\right] + \theta_1\right),$$

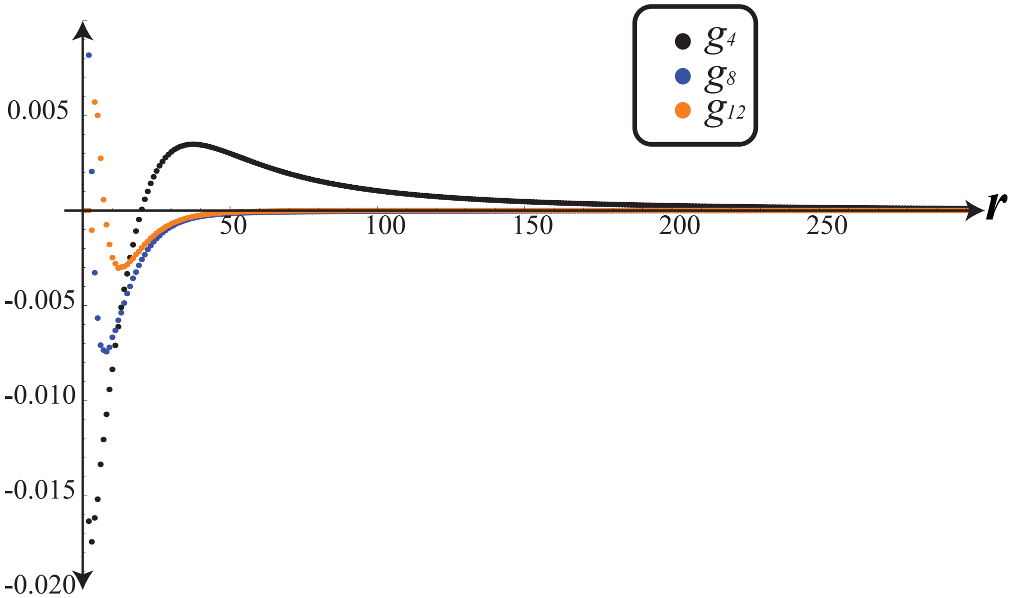

Figure 3.8: The three first leading corrections to the amplitude of the negative vortex for $\delta = 0.5$ obtained by numerical simulation and then numerical integration with the corresponding mode.

where m is the vortex charge and θ_0 and θ_1 are arbitrary constants. If we take the negative vortex in this approximation ($m = -1$) we obtain

$$\varphi \approx -\theta + \theta_0 + \varepsilon \left(\frac{3}{16} \sin\left[4\theta - 2\theta_0\right] + \theta_1 \right),$$

which is equivalent to our solution for the negative vortex when $r \to \infty$, i.e. far from the core, except for the freedom θ_1, which probably comes from taking the amplitude as a constant.

Finally, they calculated the energy of the vortices, obtaining for the positive vortex

$$E = E_0 + \pi \mathrm{d} k [1 + \delta \cos(2\theta_0)] \log(R/r_c)$$

where k is a parameter that depends on the elastic constants and the deviation from the vertical axis; d is the thickness of the sample, r_c the core radius, and R the sample radius. This result is qualitatively similar to ours, but with a simpler dependency in the anisotropy, and captures the same bifurcation diagram. For different charges, they claim that the energy is independent of the anisotropy, this is not consistent with our numerical results.

The year after Saupe, in 1973 [35] A. Rapini studied vortices in a similar way by taking the amplitude of the first unstable mode, separating its radial and angular components, and minimizing the Frank-Oseen Energy. He then searched for positive vortices setting the phase $\varphi = \theta + \theta_0$ and obtained the same equation for the vortex profile as in the Ginzburg-Landau Equation. What is interesting is that he founds a complicated equation for a parameter called K, which he claims is "roughly proportional to the energy" [35], and he founds the minima of this parameter, thus obtaining that if $K_1 < K_2$ then $\theta_0 = 0$ is a stable solution, and if $K_1 > K_2$, then $\theta_0 = \pi/2$ is stable. This is equivalent to our findings in Section 3.3. Sadly Rapini fails to point out that these two are in fact the only two positive solutions of the system, or how this modifies their core size. Finally Rapini calculates this parameter

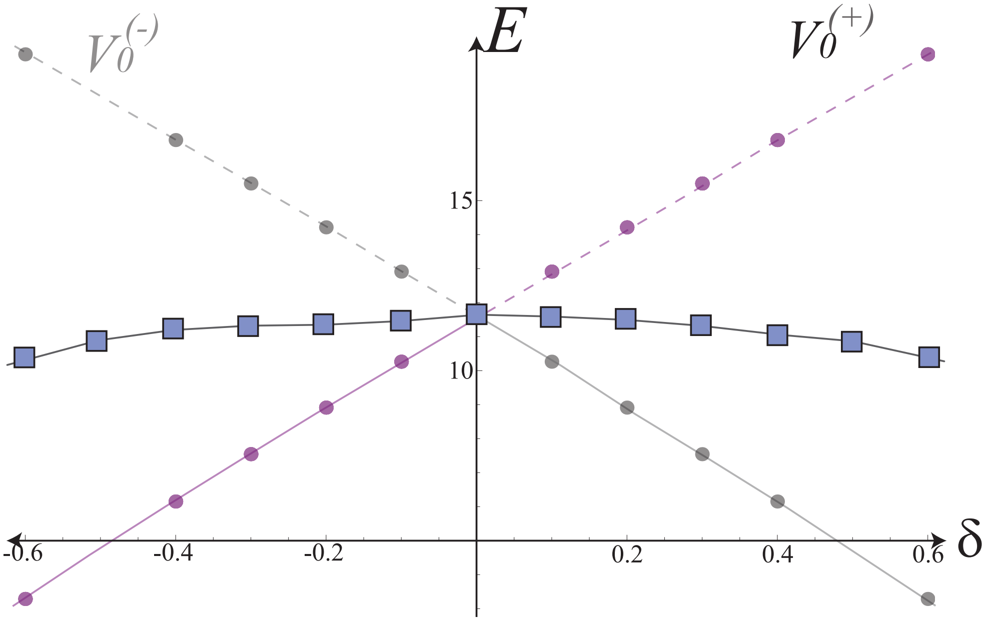

Figure 3.9: Energy $\mathcal{E}_{\mathcal{A}}$ of the negative (squares) and positive anisotropic vortices (circles).

K for the negative vortex and finds that it has always more energy than the stable positive vortex.

Chapter 4

Forced Anisotropic Ginzburg-Landau Equation

4.1 Forced Ginzburg-Landau Equation

To understand the effect of this particular forcing in the Ginzburg-Landau Equation, numerical simulations were performed with an additional, and artificial, parameter in the forcing, φ_0. Thus, the equation becomes

$$\partial_t A = \mu A + \nabla^2 A - |A|^2 A + b\frac{E_r(z)}{z} E_z \mathrm{e}^{\mathrm{i}(\theta+\varphi_0)}.$$

When there is no forcing ($E_r = 0$) and starting from the uniform and unstable state $A = 0$, in the presence of noise a great number of vortices of charge +1 and −1 appear in the system, which subsequently collide and annihilate or disappear through the borders of the simulation, depending on boundary conditions.
On the contrary, in the presence of forcing ($E_r \neq 0$) even though several vortices are initially created, only one positive vortex remains after the annihilation process. This vortex has its phase discontinuity aligned with the parameter φ_0, instead of any random direction like in the case without forcing, i.e $\theta_0 = \varphi_0$ instead of $\theta_0 \in \{0, 2\pi\}$. This vortex remains stable and pinned in the center of the forcing E_r, which has a gaussian profile. This positive vortex differs with the previously studied isotropic vortex $A = R_v \mathrm{e}^{\mathrm{i}(\theta+\varphi_0)}$ only in R_v which roughly takes the form of the root of the forcing amplitude, i.e. a gaussian profile with zero amplitude at its center.

This induction is explained by analysing the shape of the forcing, which has vorticity itself. If we look at the system from the top, the minimum energy is reached when the molecules are aligned with the local electric field (and equivalently with the forcing), but looking perpendicular to the plates, we see that there is an angle between the field and the molecules. This is the energy minimum when the radial electric field (forcing) is applied.

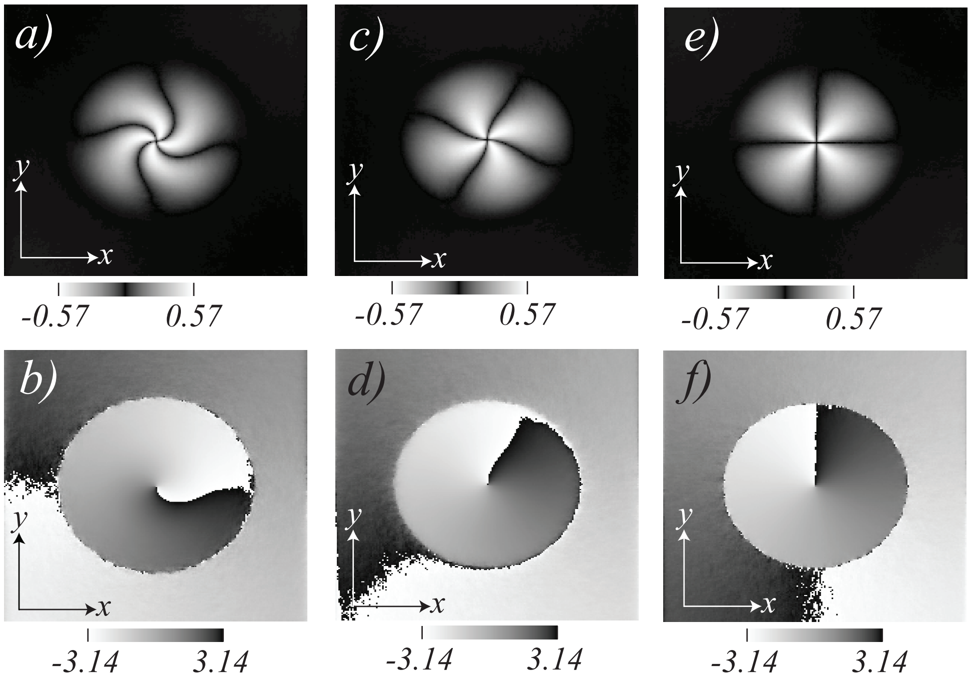

Figure 4.1: Stable solutions of the Forced Anisotropic Ginzburg-Landau Equation for different values of φ_0 and $\delta > 0$. A single positive vortex is induced in the center of the gaussian profile, whose phase depends on the value of φ_0. The nullcline $(Re(A)Im(A))$ and phase field are presented for $\varphi_0 = 0$ (a,b), $\varphi_0 = \pi/4$ (c,d), and $\varphi_0 = \pi/2$ (e,f), respectively.

4.2 Forced Anisotropic Ginzburg-Landau Equation

Let us consider the amplitude equation

$$\partial_t A = \mu A + \nabla^2 A + \delta \partial_{\eta\eta} \overline{A} - A|A|^2 + b\frac{E_r(z)}{z} E_z e^{i(\theta+\varphi_0)}.$$

As was explained in the previous section, the forcing induces a single vortex along with a preferred direction for the phase jump θ_0, in the case of our experiment $\varphi_0 = 0$, but we will study this equation for any value of $\varphi_0 \in \{0, 2\pi\}$. This phase jump may or may not coincide with the phase jump preferred by the anisotropy (which depends only in the sign of δ as was shown in Section 3.3).

When these two effects do not agree, numerical simulations have shown that the vortex starts to turn in order to align its phase jump close to the center with the preferred value for the anisotropy, but maintaining the phase jump imposed by the forcing in the border of the illuminated area. This is shown in Figure 4.1, where we can observe that when there is no mismatch between φ_0 and θ_0 (Figure 4.1 e) and f))the vortex maintains its shape ($\varphi_0 = \theta_0 = \pi/2$). But when they differ like in Figure 4.1 a) and b), where $\varphi_0 = 0$ and $\theta_0 = \pi/2$, the vortex reaches a compromise between the two states, by first beginning with the phase jump imposed by the electric field ($\theta_0 = \varphi_0$) and then turning the vortex in order to lower the energy of the system. This time dependent process is shown in Figure 4.2, the vortex starts to rotate from its center which stops when its local phase jump is vertical; this phenomenon

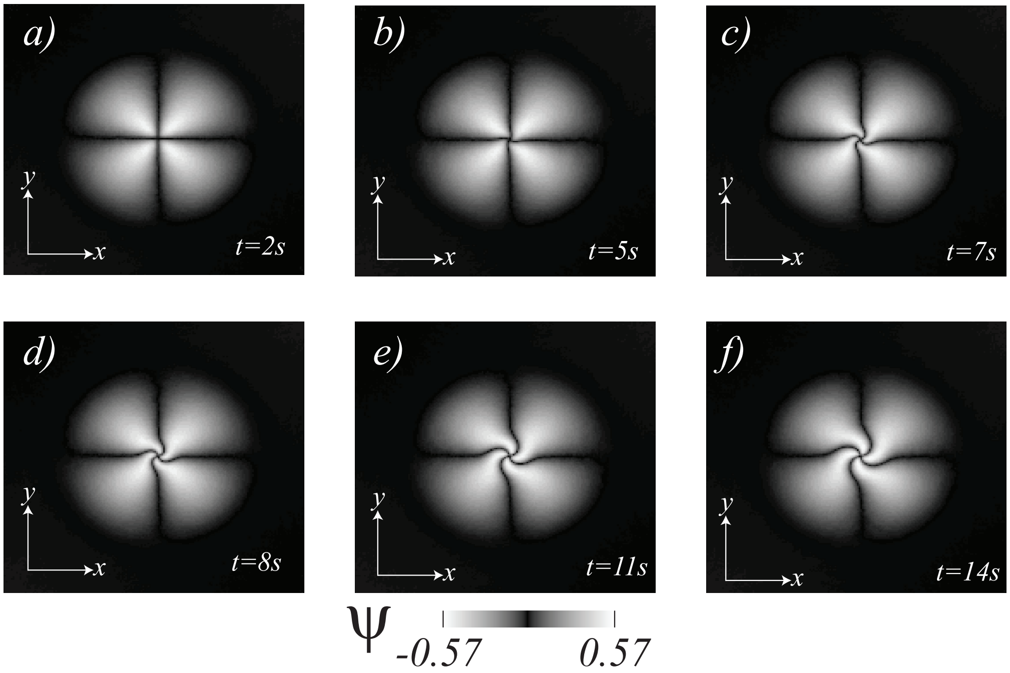

Figure 4.2: Time evolution of the induced positive vortex for positive anisotropy ($\delta > 0$) and $\varphi_0 = 0$.

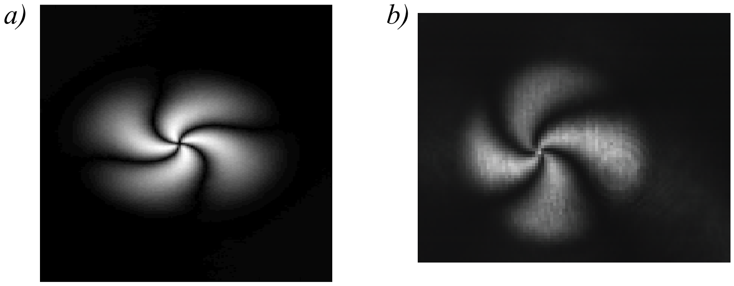

Figure 4.3: a) Numerical simulation of a vortex with swirling arms, b) Experimental observation.

gives rise to a vortex with swirling arms, which is a stationary state. This state shows quite good agreement with the experimental observations, as is shown in Figure 4.3.

We understand this rotation process in terms of energy minimization, since the effect of the anisotropy depends on the derivative of A it is stronger in the core of the vortex, thus this is the section of the vortex that contributes the most to the energy of the system. Therefore, locally turning the vortex allows to minimize the energy by making the core smaller, even though it introduces some radial dependency in the phase. In the outer regions of the vortex the gradients of the amplitude are smaller, thus making the effect of the forcing the prevalent one.

A similar effect of vortex rotating has been reported in nematic liquid crystals subjected to magnetic forcing [31]. In that experiment small circular magnets are positioned above and below a nematic liquid crystal cell, this way a magnetic field with a vorticity is applied to the cell, in a very similar way to the electric field in our experiment. This induces vortices in the cell as an initial condition for the experiment. Then, the magnets are removed, since they

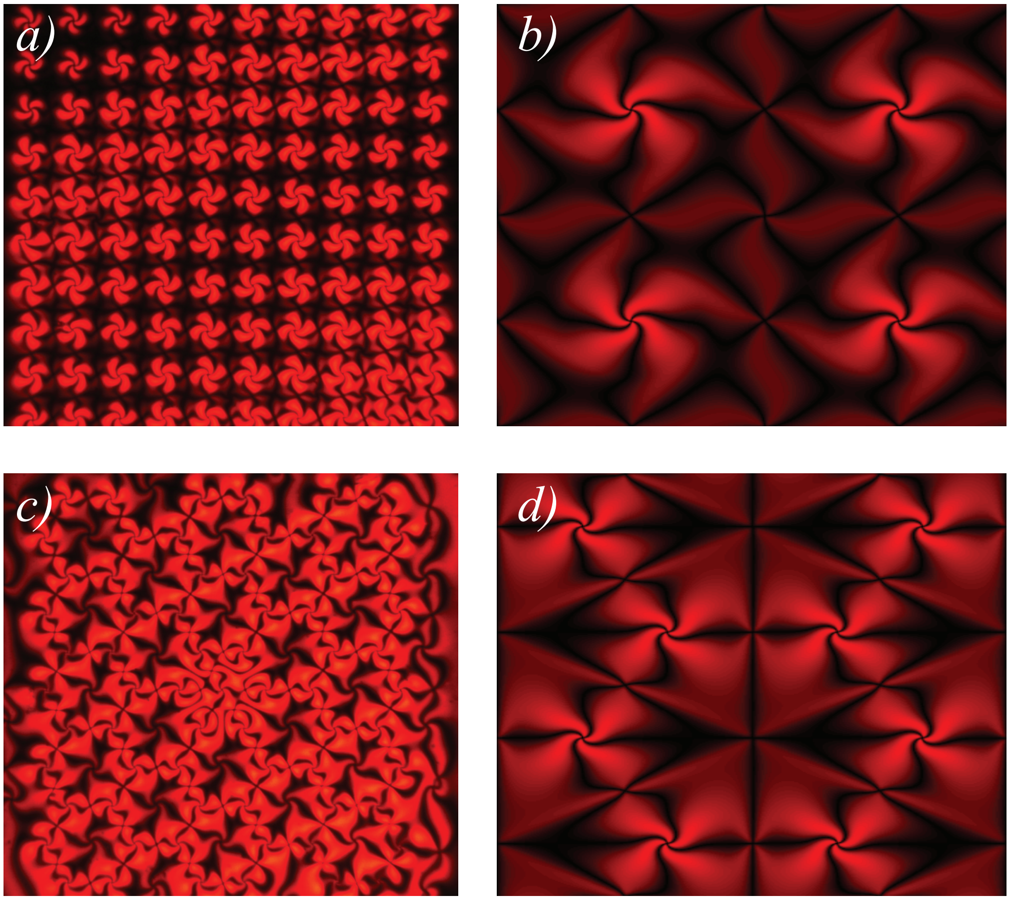

Figure 4.4: a)Experimental and b) numerical simulation of an square array of vortices. c) Experimental and d) numerical simulation of an hexagonal array of vortices.

do not allow a direct observation of the experiment, and an electric field is applied in the whole system in order to overcome the Freedericksz transition, due to this the vortices start to turn similarly to our experiment. We expect that this experiment is described in a similar way to our own: the initial condition imposed by the magnets creates positive vortices that are not stable when the electric field is applied and thus turn to become the stable positive vortex that we have already described.

4.3 Numerical Vortex Lattices

By including more than one gaussian beam in our simulations we are capable of creating vortex lattices with arbitrary spatial configurations, similar to the ones observed experimentally. This is done simply by superimposing several $E_r e^{i\theta}$ and $\mu(r)$ centred on different positions of the system, thus replicating the effect of illuminating the sample with several laser beams.

Once the system has relaxed and each center contains one positive vortex, we recreate the effect of increasing the voltage applied to the sample by upgrading the parameter $\mu(r) \rightarrow \mu(r) + \mu_0$, with $\mu_0 > 0$, this way the places on the system that were not illuminated before can now cross the Freedericksz transition and form vortices. Since the forcing is still in place the positive vortices remain in their original positions, while in the rest of the sample negative and positive vortices appear, in order to make the total topological charge of the system, depending on the overall forcing. Therefore, the vortices interact through attraction and repulsion depending on their charge, but keeping the already pinned vortices, fixed; this way, negative vortex locate in between positive vortices, and new positive vortices appear in between negative vortices. Finally, a stable arrange of vortices is created, these lattices compare well with the experiments as is shown in Figure 4.4

Chapter 5

Other Anisotropic Systems

5.1 Anisotropic Patterns in Out of Equilibrium Systems

Out of equilibrium systems are characterized by having continuous injection and dissipation of energy and momentum. This allows the existence of the most varied solutions, in particular, patterns appear in a wide variety of systems in nature, ranging from the skin of different animals to the formation of mountains (see Figure 5.1). The study of these patterns is a complicated task, because when the pattern emerges, it usually can appear in any direction (isotropic systems, where a privileged direction does not exists), when the direction or the size of the pattern in an area does not coincide with the rest of the pattern, a defect is created in order to join the pattern domains. A pattern in an isotropic system can present a wide variety of defects such as dislocations, disclinations, and dominion walls, among others, leading up to 10 type of defects [14, 36], this makes the study of defects in patterns a thorny task.

A somewhat simpler system to study patterns is in an anisotropic system, where one direction of the pattern is privileged above the other directions. This can occur physically for different reasons, for example if the wind in a beach blows predominantly in one direction, sand will develop a pattern with stripes in that particular direction; the anisotropy can also come from the boundary conditions of the system, like in the stripes of a zebra, where they take a particular direction depending on the area of the animal they appear. What is interesting about these systems is that since the anisotropy already fixed the direction of the stripes, only one type of defect can appear, dislocations [33]. Therefore dislocations appear between stripes of different wavelengths, i.e. they conciliate different wavelengths inside the pattern. These dislocations also correspond to a phase singularity, just like vortices in the *Ginzburg-Landau Equation.*

A simple model equation for anisotropic patterns is the *Anisotropic Swift-Hohemberg Equation*

$$\partial_t u = \varepsilon u - u^3 - (\partial_{xx} + q^2)^2 u + \partial_{yy} u, \tag{5.1}$$

where a wavelength is clearly defined in the x-axis [11] (see Figure 5.2). This equation was first proposed in its isotropic form by Swift and Hohemberg, in the context of Rayleigh-

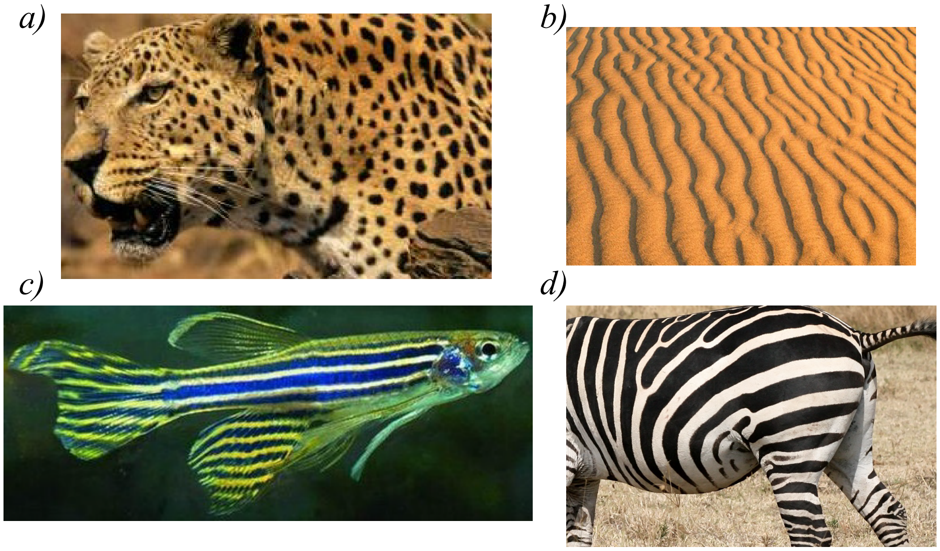

Figure 5.1: Different patterns that appear in nature. a) Patterns on the skin of a leopard, b) Anisotropic patterns in sand, c) Anisotropic pattern on the skin of a zebrafish, and d) Pattern on zebra skin.

Bernard convection [13, 14, 33], and has been widely used to study anisotropic patterns in different contexts [14].

To study dislocation dynamics the *Ginzburg-Landau Equation* has been commonly used [9, 33], since this equation describes the amplitude, or envelope, of the pattern close to the bifurcation; therefore vortices occur if a dislocation exists in the original equation. However, these descriptions present several problems, mostly related to trying to describe an anisotropic system with an isotropic one, therefore vortices are likely to occur in any position in the system and can move in any direction with the same probability, this is very different from dislocations where the movement across the pattern (glide) and along the pattern (climb) are clearly distinguished. In order to obtain a better description of the movement of dislocations we will retain the nonresonant terms of the amplitude equation so we can break the isotropy of the system.

5.2 Amended Amplitude Equation

Beginning with the *Anisotropic Swift-Hohemberg* equation

$$\partial_t u = \varepsilon u - u^3 - (\partial_{xx} + q^2)^2 u + \partial_{yy} u,$$

we would like to obtain the equation for the pattern amplitude; in order to do this we insert an Ansatz that separates the amplitude from the main spatial frequency oscillation, $u = A(X, Y, t)\mathrm{e}^{\mathrm{i}qx} + W(A, X) + c.c.$, here we assume that A depends slowly in its variables and W are non-linear corrections, with $W \ll 1$. We then get

$$\begin{aligned}\partial_t A\mathrm{e}^{\mathrm{i}qx} =& [\varepsilon A - 3|A|^2 A - A^3\mathrm{e}^{2\mathrm{i}qx} + \partial_{yy}A - \partial_{xxxx}A \\ & - 4\mathrm{i}q\partial_{xxx}A + 4q^2\partial_{xx}A]\mathrm{e}^{\mathrm{i}qx} - (\partial_{xx} + q^2)^2 W,\end{aligned}$$

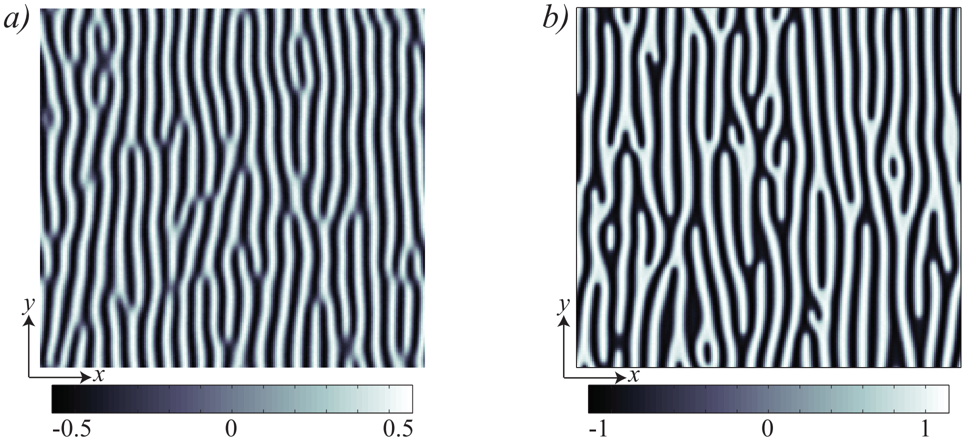

Figure 5.2: Numerical simulations of Equation 5.1 showing an anisotropic pattern for $q = 0.7$. a) $\varepsilon = 0.22$, b) $\varepsilon = 1$.

the linear operator acting on W is $\mathcal{L} = (\partial_{xx} + q^2)^2$. Introducing the inner product

$$\langle f|g\rangle = \frac{q}{2\pi n}\int_X^{X+2\pi n/q} \overline{f(x)}g(x)\mathrm{d}x,$$

then $\mathcal{L}$ is a self adjoint operator which Kernel is $\{\mathrm{e}^{\mathrm{i}qx}, \mathrm{e}^{-\mathrm{i}qx}\}$.

We then apply solvability condition by doing the inner product between the equation and the Kernel element $\langle \mathrm{e}^{\mathrm{i}qx}|$; in this product we can recognize two kinds of elements: those that are proportional to $\mathrm{e}^{\mathrm{i}qx}$ (resonant terms) and those who have other phase (nonresonant terms).

When the solvability condition is applied to a resonant term we obtain, using the Laplace Integral [8] which corresponds to the mean value theorem,

$$\langle \mathrm{e}^{\mathrm{i}qx}|f(A)\mathrm{e}^{\mathrm{i}qx}\rangle = \lim_{q\to+\infty}\frac{q}{2\pi n}\int_X^{X+2\pi n/q} f(A)\mathrm{d}x = \frac{q}{2\pi n}f(A)\frac{2\pi n}{q} = f(A(X)).$$

And when is applied to nonresonant terms we can use the stationary phase approximation [8] and obtain the following series

$$\langle \mathrm{e}^{\mathrm{i}qx}|f(A)\mathrm{e}^{\mathrm{i}mqx}\rangle = \lim_{q\to+\infty}\frac{q}{2\pi n}\int_X^{X+2\pi n/q} f(A)\mathrm{e}^{\mathrm{i}qx(m-1)}\mathrm{d}x$$

$$= \lim_{q\to+\infty}\frac{q}{2\pi n}\left(\frac{f(A)\mathrm{e}^{\mathrm{i}qx(m-1)}}{\mathrm{i}q(m-1)}\Big|_X^{X+2\pi n/q} - \int_X^{X+2\pi n/q}\frac{f'(A)\mathrm{e}^{\mathrm{i}qx(m-1)}}{\mathrm{i}q(m-1)}\mathrm{d}x\right)$$

$$= \lim_{q\to+\infty}\frac{q}{2\pi n}\{\frac{f(A)\mathrm{e}^{\mathrm{i}qx(m-1)}}{\mathrm{i}q(m-1)}\Big|_X^{X+2\pi n/q} - \frac{f'(A)\mathrm{e}^{\mathrm{i}qx(m-1)}}{(\mathrm{i}q(m-1))^2}\Big|_X^{X+2\pi n/q}$$
$$+ \int_X^{X+2\pi n/q}\frac{f''(A)\mathrm{e}^{\mathrm{i}qx(m-1)}}{(\mathrm{i}q(m-1))^2}\mathrm{d}x\},$$

this series in $1/q$ is convergent when the pattern and the amplitude have different scales. Therefore it can be approximated by its first terms, as follows

$$\begin{aligned}\langle \mathrm{e}^{\mathrm{i}qx}|f(A)\mathrm{e}^{\mathrm{i}mqx}\rangle =&\frac{q}{2\pi n}\Big\{\frac{\mathrm{e}^{\mathrm{i}qx(m-1)}}{\mathrm{i}q(m-1)}[f(A(X+2\pi n/q))-f(A(X))]\\&-\frac{\mathrm{e}^{\mathrm{i}qx(m-1)}}{(\mathrm{i}q(m-1))^2}[f'(A(X+2\pi n/q))-f'(A(X))]\\&+\mathcal{O}(1/q^3)\Big\}\\\approx&\frac{\mathrm{e}^{\mathrm{i}qx(m-1)}}{\mathrm{i}q(m-1)}\left(f'(A(X))-\frac{f''(A(X))}{\mathrm{i}q(m-1)}\right).\end{aligned}$$

Applying these results to the amplitude equation we obtain

$$\begin{aligned}\partial_t A =&\varepsilon A-3|A|^2A+\partial_{yy}A-\partial_{xxxx}A\\&-4\mathrm{i}q\partial_{xxx}A+4q^2\partial_{xx}A-\frac{\mathrm{e}^{2\mathrm{i}qx}\partial_x(A^3)}{2\mathrm{i}q}.\end{aligned}$$

Finally keeping the terms to the leading order and scaling both variable and space, we obtain the amended equation for the amplitude of the pattern, we will refer to this as *Amended Ginzburg-Landau Equation*

$$\boxed{\partial_t A=\varepsilon A-|A|^2A+\nabla^2A-\frac{\mathrm{i}\partial_{xxx}A}{2q^2}-\frac{\mathrm{e}^{4\mathrm{i}q^2x}A^2\partial_x A}{4\mathrm{i}q^2}.}$$

At first sight we can notice how the amended terms break the symmetry between x and y, because of this we expect to recover some features of the original Swift-Hohenberg Equation that are lost in the Ginzburg-Landau description. It is also noteworthy that we can not derive this equation from a Lyapunow Functional, therefore it does not have a relaxation dynamic and some permanent dynamic might appear.

Numerical simulations of this equation have shown that vortices are a persistent solution. In this equation, vortices have no longer rotational symmetry, instead, a small pattern perturbation can be observed on the amplitude (see Figure 5.6), close to the vortex core. This pattern has twice the wavelength of the original pattern, q.

5.3 Dislocation Dynamics

Using this equation we can study the movement of dislocations following the previous studies done in the *Isotropic Ginzburg-Landau Equation* by Bodenchatz et al in [9]. We then follow the same procedure and consider the last term as a perturbation as we have seen numerically that vortex still are a solution, we insert the Ansatz of a vortex moved by a phase disturbance:

$$A=R(\vec{r}-\vec{r_0}(t))\mathrm{e}^{\mathrm{i}\vec{k}\cdot\vec{r}}+W$$

where R is the vortex solution of the Isotropic Ginzburg-Landau equation, $k = Q\hat{x} + P\hat{y}$ is a phase disturbance and W are small nonlinear corrections.
Inserting the ansatz into the equation we obtain to the leading order

$$\begin{aligned} -\dot{x_0}\partial_x R - \dot{y_0}\partial_y R =&(\varepsilon W - R^2\overline{W} - 2|R|^2 W + \nabla^2 W) + 2\mathrm{i}Q\partial_x R + 2\mathrm{i}P\partial_y R \\ &- (Q^2 + P^2)R - \frac{R^2\partial_x R\mathrm{e}^{4\mathrm{i}q^2 x}}{4\mathrm{i}q^2}. \end{aligned}$$

The linear operator acting on W is

$$\mathcal{L} = \begin{pmatrix} \varepsilon - 2|R|^2 + \nabla^2 & -R^2 \\ -\overline{R}^2 & \varepsilon - 2|R|^2 + \nabla^2 \end{pmatrix}$$

and the Kernel of its conjugate is

$$Ker\{\mathcal{L}\dagger\} = \left\{ \begin{pmatrix} \partial_x R \\ \partial_x \overline{R} \end{pmatrix}, \begin{pmatrix} \partial_y R \\ \partial_y \overline{R} \end{pmatrix} \right\}$$

with the inner product already defined.
Using solvability condition with the first and the second of the kernel elements we obtain respectively

$$\begin{aligned} 0 =&\dot{x_0}(\langle \partial_x R|\partial_x R\rangle + \langle \partial_x \overline{R}|\partial_x \overline{R}\rangle) + 2\mathrm{i}P(\langle \partial_x R|\partial_y R\rangle - \langle \partial_x \overline{R}|\partial_y \overline{R}\rangle) \\ &- \frac{1}{4\mathrm{i}q^2}(\langle \partial_x R|R^2\partial_x R\mathrm{e}^{4\mathrm{i}q^2 x}\rangle - \langle \partial_x \overline{R}|\overline{R}^2\partial_x \overline{R}\mathrm{e}^{-4\mathrm{i}q^2 x}\rangle), \end{aligned}$$

$$\begin{aligned} 0 =&\dot{y_0}(\langle \partial_y R|\partial_y R\rangle + \langle \partial_y \overline{R}|\partial_y \overline{R}\rangle) + 2\mathrm{i}Q(\langle \partial_y R|\partial_x R\rangle - \langle \partial_y \overline{R}|\partial_x \overline{R}\rangle) \\ &- \frac{1}{4\mathrm{i}q^2}(\langle \partial_y R|R^2\partial_x R\mathrm{e}^{4\mathrm{i}q^2 x}\rangle - \langle \partial_y \overline{R}|\overline{R}^2\partial_x \overline{R}\mathrm{e}^{-4\mathrm{i}q^2 x}\rangle), \end{aligned}$$

where the first inner product in each equation corresponds to the mobility of the solution and requires a renormalization of the phase in order to be calculated [9]. Naming this mobility M_x and M_y respectively and solving the other inner products we obtain

$$\boxed{\begin{aligned} 0 =&\dot{x_0}M_x - 4P\pi m(\varepsilon - P^2 - Q^2) - C\frac{\sin 4q^2 x_0}{2q^2} \\ 0 =&\dot{y_0}M_y + 4Q\pi m(\varepsilon - P^2 - Q^2) - D\frac{m\cos 4q^2 x_0}{2q^2} \end{aligned}}$$

where $m = \pm 1$ is the charge of the solution and the values of C and D are given by

$$\begin{aligned} C =& -\int_0^\infty R^2(\partial_r R)^2\frac{\pi}{8q^4 r}\left(4q^2 r J_1(4q^2 r) + (16q^4 r^2 - 6)J_2(4q^2 r)\right)\mathrm{d}r \\ &+ \int_0^\infty \frac{\pi R^4}{8q^4 r^3}\left(4q^2 r J_1(4q^2 r) - 6J_2(4q^2 r)\right)\mathrm{d}r \end{aligned}$$

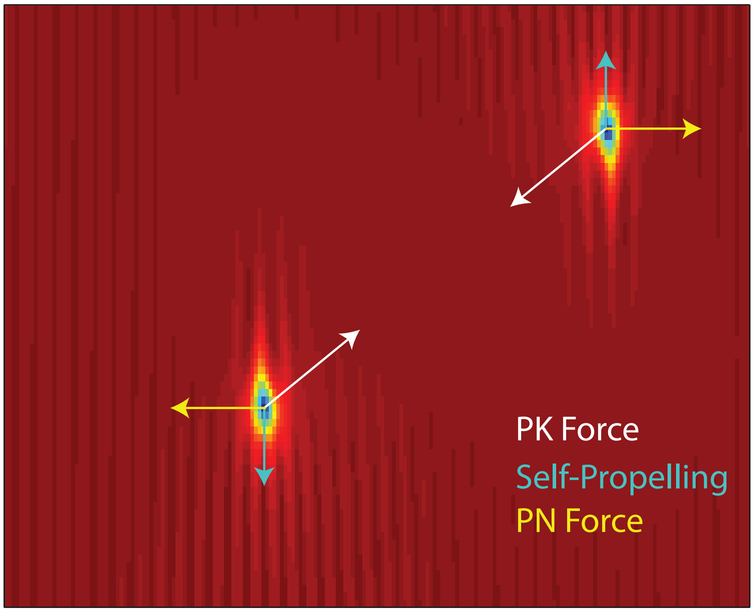

Figure 5.3: Graphic representation of the interacting forces in a blocked pair. Since the vortices are of different charge they experiment a radial attractive force, of Peach-Köehler type. A Peierls Nabarro force opposes to the movement across the pattern (horizontal axis) and a self-propelling force makes the vortices climb along the pattern.

and

$$D = \int_0^\infty \frac{2\pi J_2(4q^2r) - q^2 r J_3(4q^2r)}{4q^4r} R^2 \frac{(r\partial_r R)^2 - R^2}{2r^2} \mathrm{d}r + \int_0^\infty 2\pi J_2(4q^2r) R^3 \partial_r R \mathrm{d}r.$$

In this last expression we identified two types of forces acting on the vortex. A Peach-Köehler type of force that acts perpendicular to the wavelength induced by the vortex (Q and P) and a Peierls Nabarro type of force that comes from the underlying pattern that the dislocations observe and, therefore, depends on q. These two forces can oppose each other in some situations, producing pairs of vortices that do not change their relative distance, as is shown in Figure 5.6. Therefore, we expect a minimum distance $\mathrm{d}_c(q)$ to exist, in a way that if two vortices are separated by a distance $\mathrm{d} < \mathrm{d}_c$ they will attract and annihilate, due to the Peach-Köehler force. But, if they are separated by a distance $\mathrm{d} > \mathrm{d}_c$, then they can produce a vortex pair. This was confirmed using numerical simulations as is shown in Figure 5.6, there, two distances at which vortices pairs exist can be observed.

The magnitude of the parameters C and D are depicted in Figure 5.4 and 5.5 for different combinations of q and ε. In this last image we can observe how the force due to the periodic forcing increases with ε, which is consistent with the increasing size of the oscillation which goes with $\sqrt{\varepsilon}$, therefore at bigger values of ε is easier to find blocked dislocations pairs as is shown in Figure 5.7, unfortunately in that region of parameters other phenomena appear and dislocations are not the only defect that can exist as it can be seen in Figure 5.2 b).

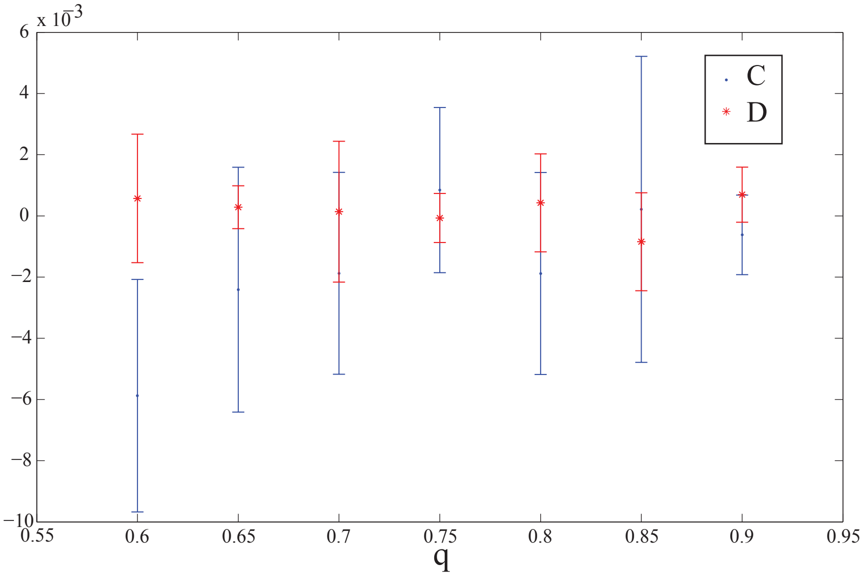

Figure 5.4: Values of C and D obtained through numerical integration for $\varepsilon = 0.22$ and different values of q.

Finally, from our kinematic law we can also see that the force imposed by the underlaying pattern oscillates at twice the frequency of the original pattern, which predicts two possible equilibrium positions for the dislocations, this has been confirmed numerically as it is shown in Figure 5.8.

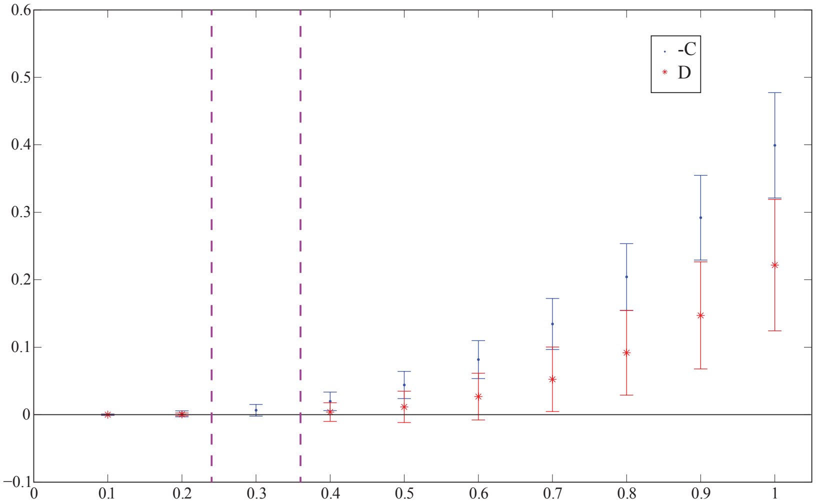

Figure 5.5: Values of C and D obtained through numerical integration for $q = 0.7$ and different values of ε.

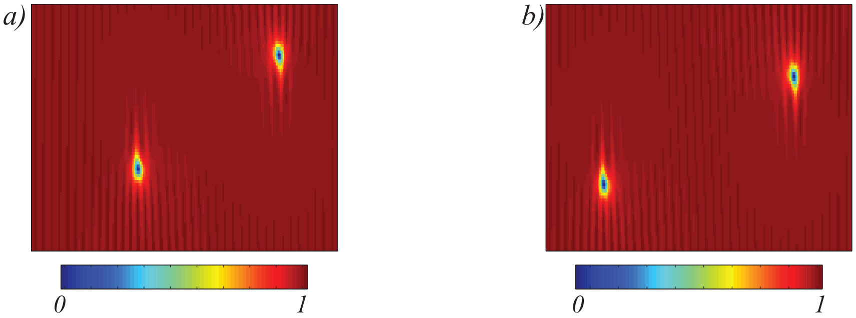

Figure 5.6: Two stationary vortex pairs with different relative distances. Due to periodic boundary conditions the vortex pair travels along the vertical direction (climbing) maintaining their relative distance.

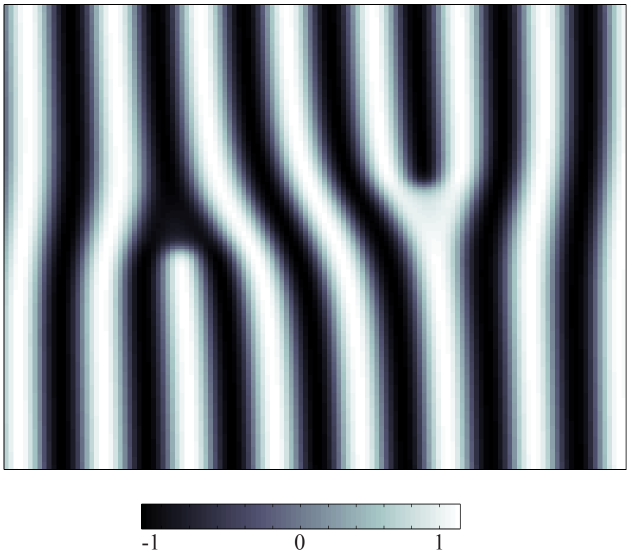

Figure 5.7: Stationary dislocation pair for $q = 0.7$ and $\varepsilon = 1$.

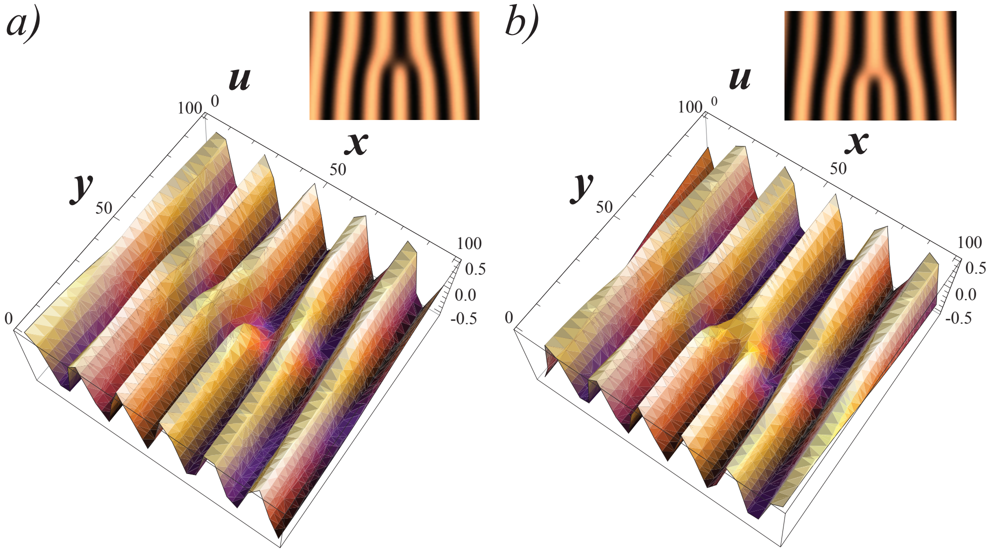

Figure 5.8: Two symmetrical types of dislocations. a) When the dislocation appears in a pattern minimum and b) when the dislocation is in a pattern maximum.

Chapter 6

Conclusions

Due to inherent fluctuations in macroscopic systems and coexistence of different spatial structures, defects are a common feature in dynamical systems appearing in pattern formation. In particular, in rotational invariance systems vortices or phase singularities are the most common local defects. This thesis is devoted to the study of phase singularities in the context of self-organization in out of equilibrium systems, these defects are well described in an unified manner by modified Ginzburg-Landau equations. This type of model was the mathematical framework for the present thesis.

Our study was focalized in the understanding of the emergence of vortices in a nematic liquid crystal light valve (LCLV) with homeotropic anchoring illuminated with a gaussian beam. This physical system allows the creation of optical vortices that are self-induced and self-aligned, along with the induction of positive vortices in the liquid crystal texture. A model equation for this system was derived from first principles. First, the electric field in the system was analysed and then, an amplitude equation was derived, close to the onset of the Freedericksz transition. This equation corresponds to a generalization of the well-know Ginzburg-Landau Equation with an anisotropic term to stand for the difference between the elastic constants and a spatial forcing term as a result of the particular electric field shape inside the cell.

This Anisotropic Ginzburg-Landau Equation was studied, characterizing its vortex solutions. Two different types of positive vortices were identified, these solutions are a scaling of the already known vortex in the Isotropic Ginzburg-Landau Equation. The energy of these solutions was calculated and it was shown how they exchange stability through a Degenerated Transcritical Bifurcation depending on the anisotropic parameter. The negative vortex was characterized perturbatively and its energy calculated numerically. This showed how the negative vortex losses its rotational invariance in the anisotropic equation, making both charges (positive and negative) no longer indistinguishable in their magnitude.

Numerical analysis of the Forced Anisotropic Amplitude Equation showed how the forcing term induces one single positive vortex in the center of the applied voltage which allows us to understand the experimental observations of light-induced matter vortices in a LCLV.

This vortex was always of the same type and consistent with the shape of the electric field inside the sample, all other vortices created by noise are quickly expelled from the system, consistent with the experimental observations. In the region of parameters our experiment takes place the induced vortex is unstable and therefore the molecules rearrange to form the stable positive vortex; since this is not consistent with what is imposed by the field, the system reaches a compromise between the two possible positive solutions forming a vortex with bent arms. This pinning mechanism allow us to envisage the possibility to create programmable vortex lattices with arbitrary spatial configuration. This was experimentally confirmed using an adequate configuration in a Liquid Crystal Light Valve. Furthermore, adapting our equation to account for different light rays showed numerical vortex lattices in quite good agreement with the experimental observations.

In the last chapter the dislocation dynamics in an anisotropic pattern was studied. To do this an Amended Amplitude Equation for the Anisotropic Swift-Hohenberg Equation was derived, in this amplitude equation dislocations show up as vortices whose dynamic was characterized, allowing the prediction of stationary dislocation pairs, which were confirmed numerically.

The results obtained in this thesis showed that phase singularities are a ubiquitous phenomena in nature, which can be described in a unified way by amplitude equations. In turn, these equations can be related to the particular physical context close to its critical points.

Bibliography

[1] Image by the liquid crystals group at the glenn h. brown liquid crystal institute at kent state university. http://www.lci.kent.edu/defect.html. Accessed: 2013-08-09.

[2] Aleksandr Aleksandrovich Andronov. *Theory of oscillators*, volume 4. Courier Dover Publications, 1987.

[3] Igor S Aranson and Lorenz Kramer. The world of the complex ginzburg-landau equation. *Reviews of Modern Physics*, 74(1):99, 2002.

[4] Igor S Aranson and Lev S Tsimring. Theory of self-assembly of microtubules and motors. *Physical Review E*, 74(3):031915, 2006.

[5] R Barboza, U Bortolozzo, G Assanto, E Vidal-Henriquez, MG Clerc, and S Residori. Vortex induction via anisotropy stabilized light-matter interaction. *Physical review letters*, 109(14):143901, 2012.

[6] R Barboza, U Bortolozzo, G Assanto, E Vidal-Henriquez, MG Clerc, and S Residori. Harnessing optical vortex lattices in nematic liquid crystals. *Physical review letters*, 111(9):093902, 2013.

[7] R Barboza, T Sauma, U Bortolozzo, G Assanto, MG Clerc, and S Residori. Characterization of the vortex-pair interaction law and nonlinear mobility effects. *New Journal of Physics*, 15(1):013028, 2013.

[8] Carl M Bender and Steven A Orszag. *Advanced mathematical methods for scientists and engineers I: Asymptotic methods and perturbation theory*, volume 1. Springer, 1999.

[9] E Bodenschatz, W Pesch, and L Kramer. Structure and dynamics of dislocations in an anisotropic pattern-forming systems. *Physica D: Nonlinear Phenomena*, 32(1):135–145, 1988.

[10] S. Chandrasekhar. *Liquid Crystals*. Cambridge University Press, 1992.

[11] MG Clerc, Claudio Falcón, D Escaff, and Enrique Tirapegui. Noise induced rolls propagation. *The European Physical Journal-Special Topics*, 143(1):171–179, 2007.

[12] John David Crawford. Introduction to bifurcation theory. *Reviews of Modern Physics*, 63(4):991, 1991.

[13] Mark C Cross and Pierre C Hohenberg. Pattern formation outside of equilibrium. *Reviews of Modern Physics*, 65(3):851, 1993.

[14] Michael Cross and Henry Greenside. *Pattern formation and dynamics in nonequilibrium systems*. Cambridge University Press, 2009.

[15] I Dierking, M Ravnik, E Lark, J Healey, GP Alexander, and JM Yeomans. Anisotropy in the annihilation dynamics of umbilic defects in nematic liquid crystals. *Physical Review E*, 85(2):021703, 2012.

[16] Ingo Dierking. *Textures of liquid crystals*. John Wiley & Sons, 2006.

[17] C Elphick, E Tirapegui, ME Brachet, P Coullet, and G Iooss. A simple global characterization for normal forms of singular vector fields. *Physica D: Nonlinear Phenomena*, 29(1):95–127, 1987.

[18] Frederick C Frank. I. liquid crystals. on the theory of liquid crystals. *Discuss. Faraday Soc.*, 25:19–28, 1958.

[19] V Freedericksz and V Zolina. Forces causing the orientation of an anisotropic liquid. *Transactions of the Faraday Society*, 29(140):919–930, 1933.

[20] MG Friedel. Les états mésomorphes de la matière. *Annales de Physique*, 18:273, 1922.

[21] T Frisch, S Rica, P Coullet, and JM Gilli. Spiral waves in liquid crystal. *Physical review letters*, 72:1471–1474, 1994.

[22] VL Ginzburg and LD Landau. On the theory of superconductivy. *Sov. Phys. Journal of Experimental and Theoretical Physics*, 20:1064, 1950.

[23] VL Ginzburg and LP Pitaevskii. On the theory of superfluidity. *Sov. Phys. Journal of Experimental and Theoretical Physics*, 7(5):858–861, 1958.

[24] Joseph Goodman. Introduction to fourier optics. 2008.

[25] Iam-Choon Khoo. *Liquid Crystals*. John Wiley & Sons, Inc., 2006.

[26] O Lehmann. Über fließende krystalle. *Zeitschrift für Physikalische Chemie*, 4:462–472, 1889.

[27] NV Madhusudana and R Pratibha. Elasticity and orientational order in some cyanobiphenyls: Part iv. reanalysis of the data. *Molecular Crystals and Liquid Crystals*, 89:249–257, 1982.

[28] Robert B Meyer. On the existence of even indexed disclinations in nematic liquid crystals. *Philosophical Magazine*, 27(2):405–424, 1973.

[29] Jürgen Nehring and Alfred Saupe. On the schlieren texture in nematic and smectic liquid crystals. *Journal of the Chemical Society, Faraday Transactions 2: Molecular and Chemical Physics*, 68:1–15, 1972.

[30] Patrick Oswald and Pawel Pieranski. *Nematic and cholesteric liquid crystals: concepts and physical properties illustrated by experiments.* CRC press, 2006.

[31] P Pieranski, B Yang, L-J Burtz, A Camu, and F Simonetti. Generation of umbilics by magnets and flows. *Liquid Crystals*, 40(12):1593–1608, 2013.

[32] Len M Pismen. *Vortices in nonlinear fields: From liquid crystals to superfluids, from non-equilibrium patterns to cosmic strings*, volume 100. Oxford University Press, 1999.

[33] Len M Pismen. *Patterns and interfaces in dissipative dynamics.* Springer, 2006.

[34] LM Pismen and JD Rodriguez. Mobility of singularities in the dissipative ginzburg-landau equation. *Physical Review A*, 42(4):2471, 1990.

[35] A Rapini. Umbilics: static properties and shear-induced displacements. *Journal de Physique*, 34(7):629–633, 1973.

[36] Steven Strogatz. *Nonlinear dynamics and chaos: with applications to physics, biology, chemistry and engineering.* Perseus Books Group, 2001.

[37] Dirk ter Haar. *Collected papers of LD Landau.* Pergamon Press London, 1965.

[38] Shin-Tson Wu and Deng-Ke Yang. *Fundamentals of liquid crystal devices.* John Wiley & Sons, 2006.

[39] Alison M Yao and Miles J Padgett. Orbital angular momentum: origins, behavior and applications. *Advances in Optics and Photonics*, 3(2):161–204, 2011.

Appendix A

Vortex Induction via Anisotropy Stabilized Light-Matter Interaction

This Appendix is the paper entitled "Vortex Induction via Anisotropy Stabilized Light-Matter Interaction" published in Physical Review Letters.

Vortex Induction via Anisotropy Stabilized Light-Matter Interaction

R. Barboza,[1,2] U. Bortolozzo,[1] G. Assanto,[2] E. Vidal-Henriquez,[3] M. G. Clerc,[3] and S. Residori[1]
[1]*INLN, Université de Nice-Sophia Antipolis, CNRS, 1361 Route des Lucioles, 06560 Valbonne, France*
[2]*NooEL-Nonlinear Optics and OptoElectronics Lab, University Roma Tre, Via della Vasca Navale 84, 00146 Rome, Italy*
[3]*Departamento de Física, FCFM, Universidad de Chile, Casilla 487-3, Santiago, Chile*
(Received 3 July 2012; published 1 October 2012)

By sending circularly polarized light beams onto a homeotropic nematic liquid crystal cell with a photosensitive wall, we are able to locally induce spontaneous matter vortices that remain, each, stable and trapped at the chosen location. We discuss the dual light-matter nature of the created vortices and demonstrate the ability of the system to create optical vortices with opposite topological charges that, consistent with angular momentum conservation, both derive from the same defect created in the liquid crystal texture. Theoretically, we identify a self-stabilizing mechanism for the matter vortex, which is provided by the concurrency of light-induced gradients and anisotropy of the elastic constants that characterize the deformation of the liquid crystal medium.

DOI: 10.1103/PhysRevLett.109.143901 PACS numbers: 42.25.−p, 42.50.Tx, 42.70.Df, 42.70.Gi

Optical vortices [1–3] are receiving considerable attention in view of their potential applications. We can mention, for instance, the exchange of angular momentum between light and matter [4], the realization of optical tweezers [5–7], the implementation of quantum computational schemes [8], the improvement of astronomical imaging [9], and wave front sensors [10]. Among the different methods envisaged to produce optical vortices, Marrucci *et al.* realized *ad hoc* matter defects with pre-imposed director orientation in liquid crystal (LC) samples, the so-called q-plates, and demonstrated that they can efficiently perform the transfer from spin-to-orbital angular momentum for circularly polarized beams [11]. This approach exploits the anisotropic nature of LC media. However, besides anisotropy, which is at the basis of their large electro-optic response, LCs are also characterized by their self-reconfiguring capability, either under the action of light [12] or of electric fields [13]. In this framework, optical vortices are expected to derive directly from the appearance of defects in the LC texture, for instance, under the application of an electric field, as it was shown for dislocations in cholesteric LCs [14] and, more recently, for umbilics in homeotropic nematics [15,16]. In particular, the umbilic defect naturally possesses a vortex-like morphology, making it attractive for realizing the matter template able to impress a helical structure on an incoming wave front. Nonetheless, major problems arise when practical implementations are aimed at, because soft-matter defects are dissipative structures that obey a complex Ginzburg-Landau equation (CGLE) and undergo a coarsening dynamics ruled by their mutual interaction and annihilation [17]. Therefore, they are unstable (see, e.g., Refs. [2,13]), usually limited to a single defect pair per sample or a defect-free sample, and without the possibility of controlled addressing.

In this Letter, we propose a novel approach for robust vortex induction, which relies on the association of nematic LCs with a photosensitive substrate, to realize a homeotropic light-valve geometry. By transforming the intensity of the incoming light into a voltage that locally applies only across the illuminated regions, the LC light valve (LCLV) enables the local induction of stable and positionally reconfigurable matter vortices, trapped at each chosen location. These matter vortices, in turn, give rise to optical vortices via the transfer of spin-to-orbital angular momentum onto the incoming light. We demonstrate the ability to control optical vortices of opposite topological charges that, consistent with angular momentum conservation, both derive from the same matter defect created in the LC layer. Then, we show the possibility of inducing adjacent independent vortices, with input beams separated by a transverse distance of the same order of their size. Our experimental results are supported by a theoretical explanation of matter vortex stability, which, on the basis of a modified Ginzburg-Landau model with anisotropic terms [18], identifies a self-stabilizing and self-centering mechanism. The latter derives from the concurrency of light-induced gradients and anisotropy of the elastic constants that describe the deformation of the LC medium. As a result, equilibrium vortex positions are found near the center of the illuminated region. Note that, compared to other techniques, our method to create optical vortices has several advantages, such as self-induction, reconfigurability, and self-centering properties, together with the low power of the beams that induce the vortices.

Experimental setup.— The setup for vortex induction is sketched in Fig. 1(a). The LCLV is prepared by interposing a $d = 15\ \mu\text{m}$ layer of nematic LC (MLC 6608 from Merck) in between two parallel interfaces, a glass plate and a slab of the transparent photoconductor $Bi_{12}SiO_{20}$ (BSO), $25 \times 25\ \text{mm}^2$, thickness 1 mm. The interior surfaces are

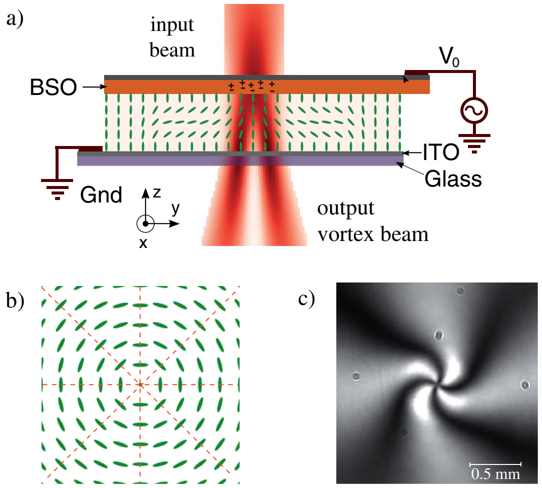

FIG. 1 (color online). (a) Schematic setup for vortex induction: a circularly polarized beam is incident on the photoconductive side of the LCLV; the voltage V_0 is such that only the illuminated region undergoes the Fréedericksz transition; when reorienting, the LC molecules follow the circular pattern associated with the electric field and create a matter vortex; this, in turn, induces an optical vortex at the exit. Matter vortex: (b) schematic sketch of the molecular director in the x-y plane; the dashed lines represent the transverse lines of the electric field; (c) intensity profile measured under white light illumination, crossed polarizers.

treated to obtain the homeotropic anchoring of the LC, that is, with the nematic director orthogonal to the confining walls. The outer surface of the photoconductor and inner surface of the glass plate are uniformly coated with thin indium-tin-oxide transparent electrodes for applying a voltage V_0 across the cell. The employed LC has a negative dielectric anisotropy, $\epsilon_a = \epsilon_{\|} - \epsilon_{\perp} < 0$, with $\epsilon_{\|}$ and $\epsilon_{\perp}$ the dielectric susceptibility for the electric fields parallel and orthogonal, respectively, to the molecular director.

When a bias V_0 is applied to the LCLV beyond the Fréedericskz transition voltage of the cell V_{FT}, the molecules tend to reorient perpendicularly to the (low frequency) electric field because of the negative ϵ_a; hence, since $\vec{E} = V_s/d\hat{z}$ (with V_s the voltage at the LC-BSO interface) is applied along the longitudinal z direction and the 2π azimuthal degeneracy imposes rotational invariance around it, the LC molecules can arbitrarily align in any direction, spontaneously forming spatial domains separated by walls, loops, and umbilic defects or vortices [13]. In the present experiment, we keep $V_0 \lesssim V_{FT}$ in order to avoid the spontaneous reorientation while bringing the molecules close to the transition point. When a light beam is incident onto the photosensitive wall of the LCLV, due to the photo-generated charges, there is a slight increase of the voltage, which effectively drops across the LC region underneath: the Fréedericskz threshold is locally overcome and the molecules start reorienting, following the intensity gradients associated with the Gaussian beam profile. Moreover, if the input beam is circularly polarized, the reorienting molecules follow the rotational structure of the associated electric-field lines. Hence, a vortex-like defect is spontaneously induced in the matter texture. A schematic sketch of the molecular director in the x-y plane is shown in Fig. 1(b), while Fig. 1(c) reports an experimental vortex profile observed under white light illumination and crossed polarizers.

Vortex induction.—To prove the vortex induction, a laser beam of wavelength $\lambda = 632$ nm and power $P = 0.55$ mW is focused on a diameter of 395 μm onto the photoconductive side of the LCLV. The input beam polarization is taken to be either right-handed (RH) or left-handed (LH) circular. Typical snapshots of the output beams observed in the two cases are shown in Fig. 2 for $V_0 = 24$ V rms at a frequency of 100 Hz. The intensity profiles, Figs. 2(a) and 2(b), show that the two beams are Gauss-Laguerre—like modes with complex amplitude of the form $\Phi(x, y, z) = \psi(r, z)\exp(ikz + m\theta)$, with ψ, k, and m representing, respectively, the amplitude, the wave vector, and the topological charge. Here, (r, θ, z) are the cylindrical coordinates associated to (x, y, z). The output beam polarization for a LH (RH) circular input beam has been verified to be RH (LH) circular. The topological charge can be estimated from the interference patterns displayed in Figs. 2(c)–2(f), for spherical and respectively planar wave front of the reference beam. The two-arm spirals in the first case and the two dislocations in the fringe patterns in the second case are robust and

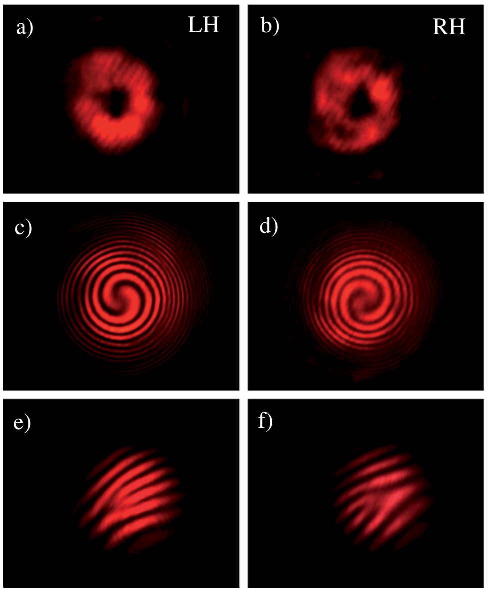

FIG. 2 (color online). Experimental observation of optical vortices induced by left-handed, LH (right-handed, RH), circularly polarized input beams: (a, b) output intensity showing Gauss-Laguerre beams, (c, d) fringe patterns after interference with a curved wave front, (e, f) patterns after interference with a planar wave front; (c, e) $m = +2$, (d, f) $m = -2$; $V_0 = 24$ V_{pp}, $P = 0.55$ mW.

reproducible. The topological charge transferred to the output beam is $m = +2$ ($m = -2$) for the LH (RH) circularly polarized input beam. Correspondingly, the spin-to-orbital angular momentum conversion is consistent with a q plate with charge $q = +1$ [11] and the matter vortex is an umbilic-like defect with winding number $+1$. Note that due to the nature of the matter vortex, $m = \pm 2$ are the only possible values for the transferred topological charge.

The efficiency of the spin-to-orbital angular momentum transfer is quantified by recording the power of the output Gauss-Laguerre mode P_{GL02} when varying the voltage V_{pp} applied to the LCLV and for various input powers. The measurements are carried out by placing a $\lambda/4$ wave plate on the path of the output beam, projecting the circularly converted RH (LH) for LH (RH) input, and the residual polarization components into two orthogonal linear polarizations, and measuring the intensity of the one carrying the topological charge [11]. The results are plotted in Fig. 3, where the value of the input power is marked along each curve. The threshold voltage V_{FT} slightly depends on the input power. The peak of the response curves corresponds to a π overall phase retardation between the ordinary and extraordinary components in the LC layer. Finally, by launching two adjacent input beams, we verify that two stable and independent vortices are obtained. Figure 4 shows the vortices induced for two RH [Fig. 4(a)], two LH [Fig. 4(b)], and LH and RH [Fig. 4(c)] input beams, respectively. The minimal separation at which the two vortices can be induced coincides approximately with the size of the individual input spots.

Mechanism for self-stabilization of the matter vortex.—To describe the mechanism of the creation and pinning of matter vortices, we derive a model in the vicinity of the Fréedericksz transition, a limit where analytical results are accessible, as nematic LC molecules are weakly tilted from the longitudinal axis $\hat{z}$ and backflow effects can be neglected. The dynamical equation for the molecular director $\vec{n}$ reads [13] $\gamma\partial_t\vec{n} = K_3[\nabla^2\vec{n} - \vec{n}(\vec{n}\cdot\nabla^2\vec{n})] + (K_3 - K_1)[\vec{n}(\vec{n}\cdot\vec{\nabla})(\vec{\nabla}\cdot\vec{n}) - \vec{\nabla}(\vec{n}\cdot\vec{\nabla})] + 2(K_2 - K_3)\times[(\vec{n}\cdot\vec{\nabla}\times\vec{n})(\vec{n}(\vec{n}\cdot\vec{\nabla}\times\vec{n}) - \vec{\nabla}\times\vec{n}) + \vec{n}\times\vec{\nabla}(\vec{n}\cdot\vec{\nabla}\times\vec{n})] + \epsilon_a(\vec{n}\cdot\vec{E})[\vec{E} - \vec{n}(\vec{n}\cdot\vec{E})]$, where γ is the LC rotational viscosity, and $\{K_1, K_2, K_3\}$ are the NLC elastic constants. Under uniform illumination, $\vec{E} = V/d\hat{z} \equiv E_z\hat{z}$, and the homeotropic state $\vec{n} = \hat{z}$ undergoes a stationary instability for critical values of the voltage, which match the Fréedericksz threshold $V_{FT} = \sqrt{-K_3\pi^2/\epsilon_a}$. Close to the transition point, we introduce the ansatz

$$\vec{n} \approx \begin{pmatrix} u(\vec{r}, t)\sin\left(\frac{\pi z}{d}\right) \\ v(\vec{r}, t)\sin\left(\frac{\pi z}{d}\right) \\ 1 - \frac{(u^2+v^2)}{2}\sin^2\left(\frac{\pi z}{d}\right) \end{pmatrix},$$

with $\vec{r} = (x, y)$ the transverse coordinates. By using the complex field $A(\vec{\rho}, t) = (u + iv)/\sqrt{4d^2\gamma/\pi^2(2K_1 - 3K_3)}$ and scaling the space as $\vec{\rho} = \vec{r}\sqrt{2/(K_1 + K_2)}$, after straightforward calculations we obtain the anisotropic CGLE [18]

$$\partial_t A = \mu_0 A - |A|^2 A + \nabla_\perp^2 A + \delta\partial_{\eta,\eta}\bar{A}, \qquad (1)$$

where $\mu_0 \equiv (-\epsilon_a E_z^2 - K_3\pi^2/d^2)/\gamma$ is the bifurcation parameter, $\delta \equiv (K_1 - K_2)/(K_1 + K_2)$ accounts for the elastic anisotropy, $\partial_\eta = \partial_x + i\partial_y$, and $\nabla_\perp^2 \equiv \partial_{xx} + \partial_{yy} = \partial_\eta\partial_{\bar{\eta}}$. When neglecting anisotropy, $\delta = 0$, the above model reduces to the CGLE with real coefficients, which admits stable dissipative vortex solutions with topological charge (winding number) ± 1 [2]. The presence of anisotropy breaks the symmetry, and the $+1$ vortex is energetically favored with respect to -1. Anisotropy, therefore, strongly influences the system response.

When the illumination has a Gaussian profile, in order to calculate the nonuniform voltage V across the LC layer, we have to consider the Laplace equation

$$\nabla^2 V + \frac{\epsilon_a}{\epsilon_\perp}\partial_z^2 V = 0, \qquad (2)$$

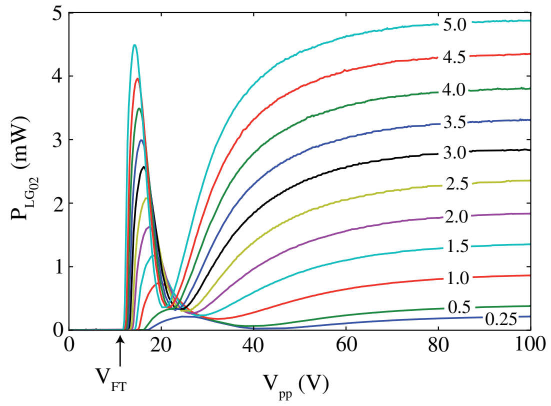

FIG. 3 (color online). Efficiency of spin-to-orbital angular momentum transfer versus experimental parameters. The power of the output Gauss-Laguerre mode P_{GL02} is plotted as a function of the voltage V_{pp} applied to the light valve and for various input powers as marked (in mW) on each curve; V_{FT} is the Fréedericksz transition voltage.

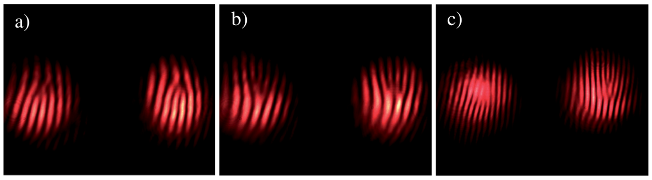

FIG. 4 (color online). Observed adjacent vortex beams for (a) right-handed (RH), (b) left-handed (LH), (c) one RH and one LH input beams; $V_0 = 24\ V_{pp}$, $P = 0.55$ mW.

where we neglect the effect of director reorientation. By taking the boundary conditions $V(x, y, 0) = 0$ and $V(x, y, d) = V_s(x, y)$, with V_s the voltage distribution at the surface, we can find a solution of the form

$$V(x, y, z) = \int \frac{\sinh(\alpha q z)}{\sinh(\alpha q d)} V_s(\vec{q}) e^{i\vec{q}\cdot\vec{r}} d\vec{q}^2, \tag{3}$$

with $\alpha = \sqrt{1 + \epsilon_a/\epsilon_\perp}$. In the limit of slow gradient, we can approximate $\sinh(\alpha q d) \sim \alpha q d$ and, therefore, take $V(x, y, z) = V_s(x, y)z/d$; that is, we can separate the transverse contribution of the electric field from its vertical one. We can, then, calculate the pinning force of a radially symmetric potential on a stationary vortex. The total energy of the system can be written as $W = W_D + W_{\text{INT}}$, with $W_D = \frac{1}{2}\int K_1(\nabla^2 \cdot \vec{n}) + K_2(\vec{n} \cdot \nabla \times \vec{n}) + K_3(\nabla \times \vec{n})^2$ and $W_{\text{INT}} = -\frac{1}{2}\epsilon_a \int (\vec{n} \cdot \nabla V)^2$ the deformation and the interaction energy, respectively. By taking as an ansatz for $V_s(x, y)$ a Gaussian profile of width w and amplitude V_1, that is, $V_s(\vec{r}) = V_{s_0} + V_1 \exp(-2r^2/w^2)$, and by inserting it into the expression for W_{INT}, after straightforward calculations, we find $W_{\text{INT}} = -\frac{\pi}{4}\epsilon_a d V_1^2[\cos(2\chi) \times \exp(-4L^2/w^2) + 1]$, where L is the distance of the vortex core from the center of the radially symmetric potential and χ is the angle of the nematic director in the transverse plane with respect to the radial lines of the electric field. Since in our case, $\epsilon_a < 0$, the defect has a minimum energy when $\chi = \pi/2$ [19]; that is, the director is orthogonal to the field lines [see Fig. 1(b)]. By accounting for this transverse correction, the bifurcation parameter is modified as follows:

$$\mu(\rho) = \mu_o + \epsilon_a d^2(1/3 - 1/2\pi^2)|\partial_\eta E_z|^2/\gamma \equiv \mu_0 + \mu_1, \tag{4}$$

which incorporates light-induced gradients, with μ_0 the same as before and $E_z = V_s(\vec{r})/d$. A circular region is below or above the Fréedericksz transition threshold when $\mu_0 + \mu_1 < 0$ or $\mu_0 + \mu_1 > 0$, respectively. Moreover, first-order corrections introduce in Eq. (1) transverse pinning and forcing terms that have the form of $(1/3 - 1/\pi^2)(\partial_\eta E_z)^2 \bar{A} + 2L/\pi E_z \partial_\eta E_z$ [20].

We perform numerical simulations of the modified Eq. (1), starting from an initial homeotropic condition $A = 0$ in the presence of noise and for $\mu_0 + \mu_1 > 0$. At the beginning, we observe the creation of a large number of vortices, later accompanied by a coarsening evolution through the annihilation of oppositely charged vortices, after which a few vortices survive. In the isotropic case, $\delta = 0$ and no transverse pinning terms, we observe that the vortices move away from the center, then they disappear by exiting through the edges, and finally there would be no vortex left in the system. However, when we consider the joint effects of transverse pinning and anisotropy, $\delta \neq 0$, the scenario changes. While the negatively charged vortices continue to move towards the perimeter of the circle, where they finally vanish, the vortices with positive charges repel each other and also disappear at the edges, but one of them remains pinned at an equilibrium position close to the center, with a small but finite offset.

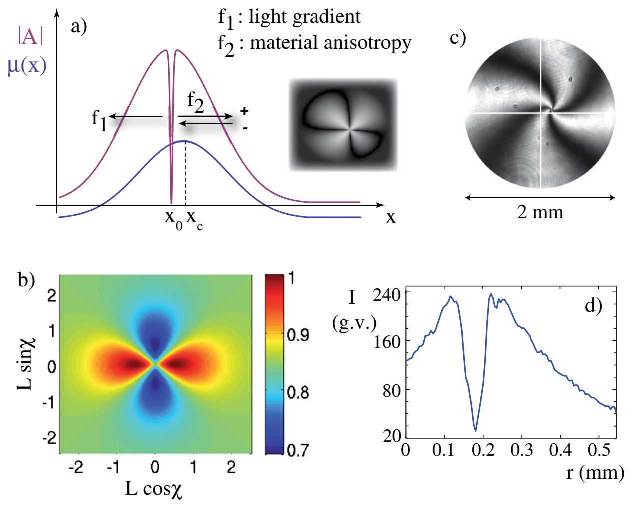

FIG. 5 (color online). Effect of the anisotropy on vortex stabilization. (a) Calculated vortex profile; f_1 and f_2 are the forces generated by the parameter gradients and anisotropy, respectively; a numerically simulated vortex is shown in the inset. (b) Pinning potential showing the equilibrium vortex positions near the center; χ is the angle of the nematic director in the transverse plane. (c) Photograph of a stable experimental vortex; the cross indicates the center of the illuminated region. (d) Corresponding intensity profile versus the radial coordinate r; g.v. stands for gray values on the camera.

Figure 5 illustrates the role of anisotropy on vortex stabilization. The equilibrium position can be interpreted as resulting from the balance of two forces: a radial force induced by the parameter gradients, which tend to push the vortices to the edges of the illuminated region, and a force induced by the anisotropic deformation, which is opposite to the light gradients. In Fig. 5(a), the numerically calculated vortex profile is plotted together with parameter variation, with the arrows indicating the forces caused by light gradients and anisotropy respectively. The direction of the force due to anisotropy depends on the vortex charge. Because of the balance between the two opposite forces, the vortex core is at an equilibrium position x_0 close to but not exactly coincident with the center x_c of the illuminated region. Figure 5(b) shows the numerically calculated potential, in which four equilibrium vortex positions near the center are visible. An experimental example of a stable experimental vortex is shown in Fig. 5(c). The corresponding intensity profile is plotted in Fig. 5(d) against the radial coordinate r.

Conclusions.—By using a nematic LC in a homeotropic LV geometry, we experimentally demonstrated a novel robust phenomenon of controlled vortex induction, which is, at the same time, low power, self-induced, self-stabilizing, and positionally stable. We have highlighted the relative role of the matter vortex and optical vortex. The latter is mediated by the spin-to-orbital angular momentum transfer of photons. Besides, we have pinpointed the theoretical basis of the vortex stability by means of a generalized Ginzburg-Landau model that takes into account medium anisotropy.

M. G. C., U. B., and S. R. acknowledge financial support from the ANR international program Project No. ANR-2010-INTB-402-02 (ANR-CONICYT39), “COLORS.” M. G. C. acknowledges funding from the FONDECYT Project No. 1120320 and Anillo Grant No. ACT127. G. A. acknowledges travel funding from the Program for Internationalisation at University Roma Tre.

[1] J. F. Nye and M. V. Berry, Proc. R. Soc. A **336**, 165 (1974).
[2] L. M. Pismen, *Vortices in Nonlinear Fields* (Oxford Science Publications, New York, 1999).
[3] M. S. Soskin and M. V. Vasnetov, Prog. Opt. **42**, 219 (2001).
[4] L. Allen, M. W. Beijersbergen, R. J. C. Spreeuw, and J. P. Woerdman, Phys. Rev. A **45**, 8185 (1992).
[5] N. B. Simpson, L. Allen, and M. J. Padgett, J. Mod. Opt. **43**, 2485 (1996).
[6] J. E. Curtis, B. A. Koss, and D. G. Grier, Opt. Commun. **207**, 169 (2002).
[7] D. G. Grier, Nature (London) **424**, 810 (2003).
[8] H. H. Arnaut and G. A. Barbosa, Phys. Rev. Lett. **85**, 286 (2000).
[9] F. Tamburini, G. Anzolin, G. Umbriaco, A. Bianchini, and C. Barbieri, Phys. Rev. Lett. **97**, 163903 (2006).
[10] K. Murphy and C. Dainty, Opt. Express **20**, 4988 (2012).
[11] L. Marrucci, C. Manzo, and D. Paparo, Phys. Rev. Lett. **96**, 163905 (2006).
[12] I. C. Khoo, *Optics and Nonlinear Optics of Liquid Crystals* (World Scientific, Singapore, 1993).
[13] P. G. de Gennes and J. Prost, *The Physics of Liquid Crystals* (Oxford Science Publications, New York, 1993), 2nd. ed.
[14] D. Voloschenko and O. D. Lavrentovich, Opt. Lett. **25**, 317 (2000).
[15] E. Brasselet and C. Loussert, Opt. Lett. **36**, 719 (2011).
[16] E. Brasselet, Phys. Rev. Lett. **108**, 087801 (2012).
[17] I. Dierking, O. Marshall, J. Wright, and N. Bulleid, Phys. Rev. E **71**, 061709 (2005).
[18] T. Frisch, S. Rica, P. Coullet, and J. M. Gilli, Phys. Rev. Lett. **72**, 1471 (1994).
[19] S. Chandrasekhar, *Liquid Crystals* (Cambridge University, New York, 1977).
[20] The full model derivation will be reported elsewhere.

Appendix B

Harnessing Optical Vortex Lattices in Nematic Liquid Crystals

This Appendix is the paper entitled "Harnessing Optical Vortex Lattices in Nematic Liquid Crystals" published in Physical Review Letters.

Harnessing Optical Vortex Lattices in Nematic Liquid Crystals

R. Barboza,[1,2] U. Bortolozzo,[1] G. Assanto,[2] E. Vidal-Henriquez,[3] M. G. Clerc,[3] and S. Residori[1]
[1]INLN, Université de Nice-Sophia Antipolis, CNRS, 1361 Route des Lucioles, 06560 Valbonne, France
[2]NooEL-Nonlinear Optics and OptoElectronics Lab, University Roma Tre, Via della Vasca Navale 84, 00146 Rome, Italy
[3]Departamento de Física, FCFM, Universidad de Chile, Casilla 487-3 Santiago, Chile

(Received 14 June 2013; published 26 August 2013)

By creating self-induced vortexlike defects in the nematic liquid crystal layer of a light valve, we demonstrate the realization of programable lattices of optical vortices with arbitrary distribution in space. On each lattice site, every matter vortex acts as a photonic spin-to-orbital momentum coupler and an array of circularly polarized input beams is converted into an output array of vortex beams with topological charges consistent with the matter lattice. The vortex arrangements are explained on the basis of light-induced matter defects of both signs and consistent topological rules.

DOI: 10.1103/PhysRevLett.111.093902 PACS numbers: 42.25.−p, 42.50.Tx, 42.70.Df, 42.70.Gi

Optical vortices are singular points where the electromagnetic field goes to zero and around which the phase forms an n-armed spiral profile, with n the topological charge [1–3]. In low-order Gauss-Laguerre beams, a single optical vortex corresponds to a phase singularity on the axis of the beam. Vortex beams attract a lot of attention in view of their applications [4], including the exchange of angular momentum between light and matter [5], optical tweezers [6–8], quantum computation [9], data transmission [10], and enhancement of astronomical images [11]. To date, optical vortices were generated mainly by using spiral phase plates [12] or diffractive elements [13,14]. The introduction of q plates, planar elements with a preset radial director orientation [15], as well as the exploitation of umbiliclike defects [16] in nematic liquid crystals has opened new promising avenues, these approaches providing both tunability and high efficiency. Direct optical trapping of liquid crystal defects, first reported in nematics [17] and then extended to other textures, as cholesterics and smectics [18], was also demonstrated. However, the alignment of the incoming beam with the "vortex-making" element remains critical in certain conditions, for instance, in the presence of atmospheric turbulence as required by coronagraph applications [19]. By exploiting reorientational nonlinearities in the nematic liquid crystal (LC) layer of a light valve, we have recently realized vortex beams that are self-induced, and hence, self-aligned with the impinging light beam [20]. In this Letter, we show that a similar approach can be successfully exploited to create closely packed lattices of optical vortices with arbitrary and reconfigurable geometric distributions. As long as LC reorientation occurs only in the illuminated areas (which happens for relatively low amplitudes of the voltage applied to the light valve), the vortices on adjacent lattice sites are independent from one another and all have the same sign. Conversely, when reorientation occurs in the whole liquid crystal layer (for increased applied voltages), all the vortices become tightly coupled together, leading to the spontaneous generation of defects with opposite signs in between adjacent lattice sites. The resulting vortex arrangements are consistent with simple topological conservation rules accounting for the reconnection of reorientation lines in the distorted nematic layer. Similar rules were recently reported in topological colloids, where particles of various shapes were introduced in a nematic host [21], as well as in nematic samples submitted to magnetic fields created by small magnets [22]. Remarkably, in our case, all the topological reconnections are reconfigurable, optically addressable, and tunable via the voltage applied to the light valve. Moreover, the induced defect lattices act as arrays of photonic spin-to-orbital angular momentum couplers with both signs of the topological charge.

The vortex induction process is schematically represented in Fig. 1(a). The liquid crystal light valve (LCLV) is filled with a nematic mixture exhibiting negative dielectric anisotropy $\Delta\varepsilon = \varepsilon_{\parallel} - \varepsilon_{\perp} < 0$. In such a valve, the transparent interfaces are treated in order to provide the homeotropic alignment of the liquid crystals, that is, with the nematic director (optic axis) perpendicular to the confining walls, one of which is a photoconductive $Bi_{12}SiO_{20}$ (BSO) slab. Owing to this photoconductive substrate, when the LCLV is illuminated by a Gaussian light beam, the effective voltage drop across the LC layer acquires a bell shaped profile, peaked in the center of the illuminated area and able to overcome the critical value of the Fréedericksz transition for which the molecules start to reorient owing to the torque exerted by the electric field [23]. As we employ a liquid crystal with $\Delta\varepsilon < 0$, the torque exerted along the short molecular axis is larger than that on the long axis; therefore, the molecules tend to (re)align perpendicularly to the electric field, leading to a 2π-degenerate reorientation and the formation of topological defects in the nematic texture [24]. Besides, the Gaussian profile of the incoming beam also produces a transverse component of the electric field, thus giving rise to an effective potential able to pin the topological defect close to the optical intensity peak [20,25].

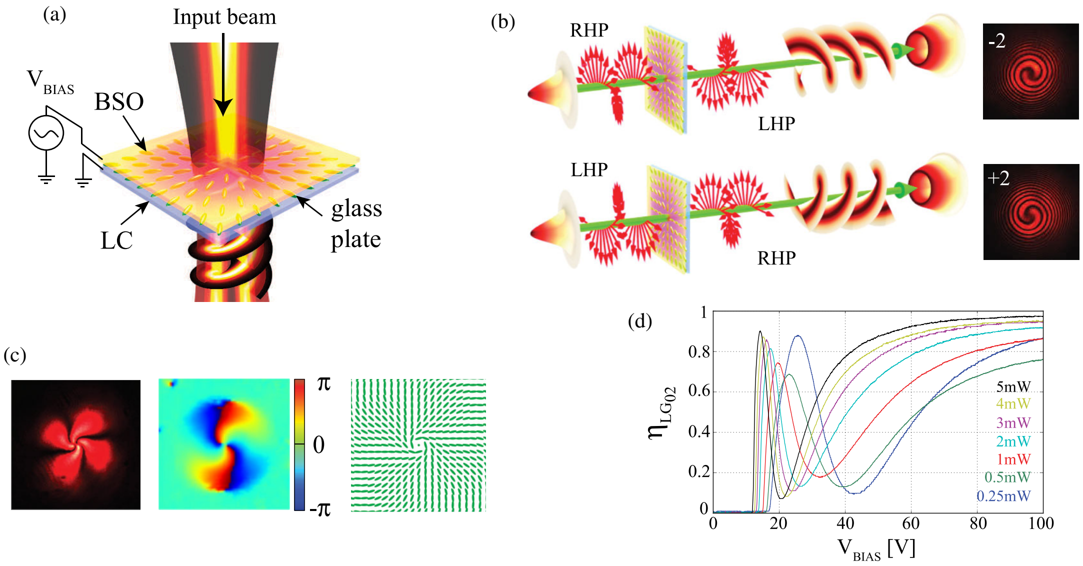

FIG. 1 (color online). Schematic representation of (a) optical vortex self-induction and (b) spin-to-orbital angular momentum transfer through the induced defect: An RHP (LHP) beam is converted into an LHP (RHP) beam with a phase singularity of charge -2 $(+2)$; experimental interferograms are shown beside the respective panels. (c) A matter defect observed under crossed polarizers (left); spatially resolved polarimetry (middle); reconstructed molecular organization (right). (d) Spin-to-orbital angular momentum conversion efficiency measured versus voltage bias and for various input intensities.

The created defect, in turn, couples orbital and spin components of the optical angular momentum; hence, the outgoing beam acquires a helical wavefront. The matter-defect–optical-vortex duality and their mutual coupling are illustrated in Fig. 1(b). An input Gaussian beam produces a vortexlike distribution of the LC molecules (a defect) and, because of the different phase retardations undergone by ordinary and extraordinary waves, a right-handed (left-handed) RHP (LHP) circularly polarized beam gets transformed into a Gauss-Laguerre beam of opposite polarization and carrying a phase singularity of topological charge -2 $(+2)$. Actual snapshots of output beams with spiraling interference fringes are shown beside the respective panels in Fig. 1(b). The opposite signs of the optical vortices are revealed by the opposite rotations of the spiral arms. The matter defect was initially characterized by observing it under crossed polarizers [left panel of Fig. 1(c)]. The black cross appearing in these conditions is the signature of a umbiliclike defect, which can be produced by two different types of deformations of the nematic texture, corresponding to ± 1 signs, or winding numbers, of the defect [26]. In order to discriminate the sign of the defect, we carried out spatially resolved polarimetry [27]: using quarter-wave plates, we analyzed the local birefringence and reconstructed the phase distribution around the defect [central panel of Fig. 1(c)]. The polarimetric profile shows that the defect is, indeed, umbiliclike and of winding number $q = +1$. Note that the reconstructed phase is proportional to 2θ, with θ the liquid crystal tilt in the transverse plane; therefore, the 4π phase jump around the singularity indicates a 2π change of the LC tilt angle θ. Correspondingly, the reconstructed molecular organization in the transverse plane has an azimuthal distribution [right panel of Fig. 1(c)]; hence, the defect acts as a q plate, to which a Jones matrix can be associated [28]. It can be shown that for a circularly polarized input $\vec{e}_\sigma = (\alpha/\sqrt{2})(\vec{x} + i\sigma\vec{y})$, where α is the amplitude and $\sigma = +1$ (-1) stands for the LHP (RHP), the exit field is given by $\vec{e}_{\text{out}} = \alpha\cos(\delta/2)\vec{e}_\sigma + \exp(2iq\sigma\xi)\alpha\exp(2i\sigma\theta_0)\sin(\delta/2)\vec{e}_{-\sigma}$; that is, the incoming circular polarization is converted to the opposite one with a helical phase $\exp 2iq\xi$ through a conversion factor $\sin^2(\delta/2)$, δ being the overall phase shift between ordinary and extraordinary components. The conversion efficiency, measured by recording the intensity of the output (converted) beam for different input powers, is plotted versus voltage bias in Fig. 1(d). For small input powers, the Fréedericksz threshold is large due to the voltage drop over the BSO slab. For higher powers, the vortex appears sooner due to the increased conductivity of the BSO. In each curve, the first peak is reached when δ is an odd multiple of π. Saturation occurs at high voltages.

In order to describe the mechanism of the optical vortex self-induction, we have derived from first principles a forced Ginzburg-Landau equation [25]

$$\gamma\partial_t A = \mu A - aA|A|^2 + K\nabla_\perp^2 A + \Delta K \partial_{\eta,\eta}\bar{A} + b\frac{E_r(r,z)}{z}E_z e^{i\theta}, \qquad (1)$$

where A is the amplitude of the LC director field deformation, μ is the bifurcation parameter describing the Fréedericksz transition, a is the saturation parameter, $b \equiv \Delta\varepsilon 2d/\pi$, E_z and E_r are the longitudinal, respectively, transverse electric fields, $\partial_\eta \equiv \partial_x + i\partial_y$ is the derivative on the transverse (x, y) plane, $\nabla_\perp \equiv \partial_{\eta,\bar{\eta}}$, z is the longitudinal coordinate, $K \equiv (K_1 + K_2)/2$, and $\Delta K \equiv (K_1 - K_2)/2$ accounts for the elastic anisotropy K_i, $i = \{1, 2, 3\}$ being the LC elastic constants. Without the last two terms, the above equation is the well-known Ginzburg-Landau equation, a prototype model widely employed to describe dissipative vortex dynamics [2]. The inclusion of the last two terms accounts for the elastic anisotropy of the LC and the effective electric potential induced by the light impinging on the photoconductor, which are responsible for the pinning of the matter vortex at the center of the illuminated areas [20].

The setup for generating vortex lattices is sketched in Fig. 2. The beam of a diode-pumped frequency-doubled solid-state (DPSS) laser at wavelength $\lambda = 532$ nm is expanded, collimated, and directed to a spatial light modulator (SLM). The SLM is computer driven by intensity masks (an example is shown in the inset, the lattice period is 0.5 mm, and the diameter of the vortex core is 1.2 μm) which, through a lens, are imaged onto the BSO side of the LCLV. The vortex beams at the LCLV output are recorded by a CCD camera. In order to observe the whole orientational structure inside the LC layer, the LCLV is also illuminated by white light and the transmitted field is imaged at the CCD plane. Polarizers and red filters discriminate the green vortex beams from the white light transmitted through the valve. A He-Ne laser at wavelength $\lambda = 632$ nm is used to realize an interferometer, through which the phase singularities are visualized by making the whole vortex lattice interfere with an expanded collimated beam.

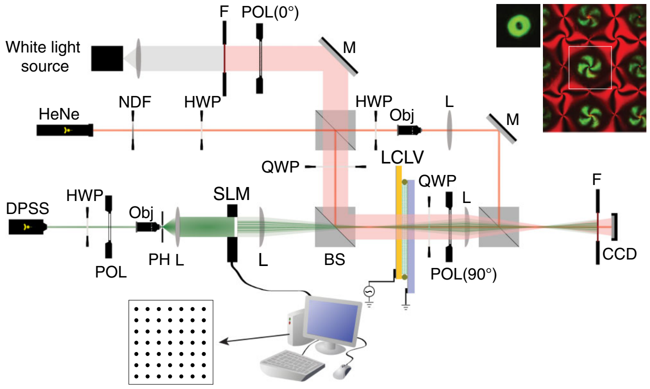

FIG. 2 (color online). Experimental setup. Obj, objective; BS, beam splitter; M, mirror; SLM, spatial light modulator; NDF, neutral density filter; F, filter transmitting the red components of the white light source for background illumination of the sample; POL, polarizer; HWP, half-wave plate; QWP, quarter-wave plate; PH, pinhole; L, lens; and CCD, charge-coupled device camera. Bottom inset: Example of square modulation mask as input to the SLM. Upper inset: Enlarged view of the sample observed under crossed polarizers when illuminated by the square grid (bright spots from the DPSS green laser) and white light background; on the left is an enlarged view of a single vortex.

Defect lattices were generated with various symmetries and spatial distributions, specifically designing the intensity masks for the SLM in order to achieve close packing of the vortices. Examples of hexagonal vortex lattices are displayed in Fig. 3. At low voltage, the vortices are independent from one another and can be individually addressed [Figs. 3(a) and 3(b)]. When the voltage is increased, adjacent vortices become coupled through reorientation in the whole nematic background. Because of the topological constraints associated with the reconnection of reorientation lines, two (initially generated) adjacent vortices of equal sign induce a vortex of opposite charge in between them. An example of fully connected network of vortices with alternating signs is visible in Fig. 3(c). Figure 3(d) presents the interferogram obtained with a plane reference wave. The spatially resolved polarimetry of the vortex distributions in Figs. 3(e) and 3(f) shows the

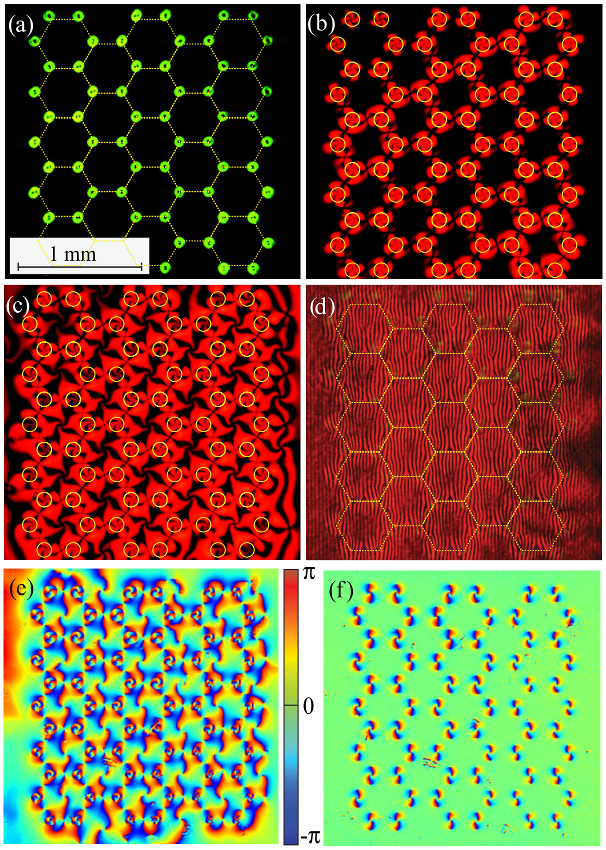

FIG. 3 (color online). Hexagonal vortex lattices: (a) Laser intensity distribution $V = 19$ V; (b),(c) white light images under crossed polarizers, (b) independent vortices $V = 18$ V and (c) fully coupled lattice $V = 22$ V; (d) interferogram $V = 12$ V; and (e),(f) spatially resolved polarimetry, (e) $V = 22$ V and (f) $V = 18$ V. The dashed lines mark the lattice structure, and the circles indicate the positions of the addressing light spots; the input intensity is $I = 250$ μW/cm^2.

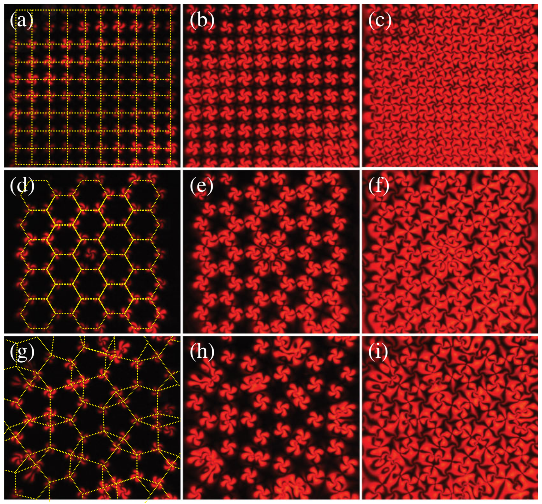

FIG. 4 (color online). Vortex lattices with various spatial distributions; the images were taken through crossed polarizers; input intensity $I = 250\ \mu\text{W/cm}^2$. Squares for (a)–(c) $V = 14$, 18, 22 V, hexagons with a defect in the center for (d)–(f) $V = 14$, 18, 22 V, and Penrose lattice for (g)–(i) $V = 14$, 18, 22 V.

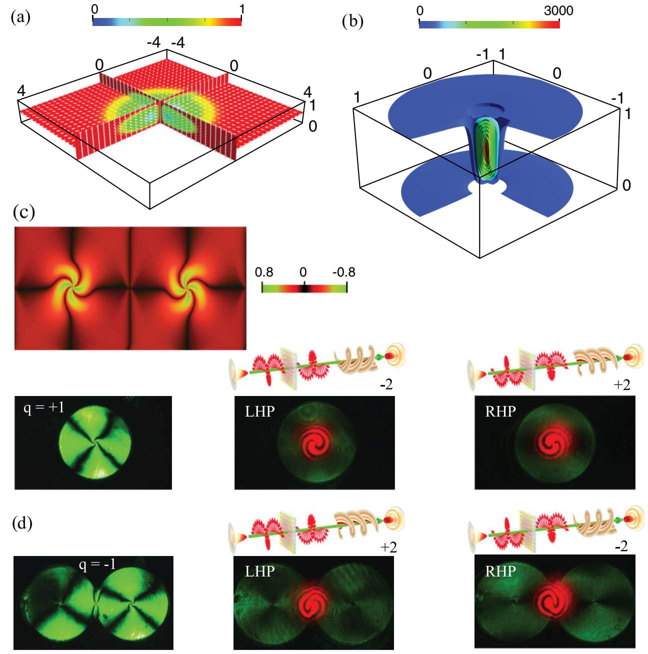

FIG. 5 (color online). Numerical distribution of (a) the molecular director and (b) energy density around the defect; lengths are normalized to the cell thickness. (c) Simulated vortex structure and spatial arrangement; two $+1$ vortices are initially addressed, with a -1 spontaneously appearing in between them. (d) Experimental demonstration of spin-to-orbital angular momentum transfer. Left panels: A $q = +1$ defect is created in the center of an illuminated area; a $q = -1$ defect is generated in between two spots. Central (right) panels: For an input LHP (RHP), the $q = +1$ defect yields an optical vortex with charge -2 $(+2)$, and the $q = -1$ defect produces an optical vortex with charge $+2$ (-2).

sign of each vortex by the direction of circulation of the phase arms.

Employing suitably designed intensity masks, we realized vortex lattices with various distributions. Figure 4 shows the cases of square, Penrose, and hexagonal lattices with a topological frustration in the center. Again, as the bias was increased from low to high voltages, we observed the transition from independent vortices to a fully connected network of adjacent vortices of alternating signs. In hexagonal lattices, a topological frustration is induced by addressing a defect in the center of a hexagonal cell. If this is done when the fully connected network is already established, the addressed defect undergoes a topological frustration with respect to the defect with opposite sign that was present at the same site. As a consequence, the unmatched reorientation lines reorganize themselves and give rise to a transient unwinding dynamics of the defect spiral arms, until the system is able to self-heal into a stationary configurational tradeoff [29].

Figures 5(a) and 5(b) display a numerical simulation of the vortex structure obtained by using the three-dimensional molecular director dynamics, illustrating, respectively, the molecular orientation around the defect core and the energy density of the associated deformation. Figure 5(c) shows the numerical solution of Eq. (1) [25]: the two initially addressed (by Gaussian beams) $q = +1$ vortices appearing in the middle of each illuminated area spontaneously induced an additional $q = -1$ vortex between them, owing to the topological constraints that force the reconnection of adjacent orientation lines in the nematic texture. These constraints could be exploited to establish the experimental induction of a $q = -1$ vortex, thereby demonstrating spin-to-orbital angular momentum transfer for $q = \pm 1$ matter defects, as shown in Fig. 5(d) for individual lattice sites (the extension to all lattice sites is cumbersome but straightforward). A $q = +1$ defect is created in the center of an illuminated area, whereas a $q = -1$ defect is generated in between two adjacent illuminated spots. Correspondingly, for a LHP input, the $q = +1$ $(q = -1)$ defect produces an optical vortex of topological charge -2 $(+2)$; for a RHP input, the $q = +1$ $(q = -1)$ defect yields an optical vortex of charge $+2$ (-2). Noteworthily, manipulation and control of optical vortices can be achieved either by changing the polarization of the input beam or by employing matter defects with opposite signs.

In conclusion, we have shown that optical vortex lattices can be realized in a liquid crystal light valve. The optical vortices are driven by their counterparts in the nematic texture, where umbiliclike defects are created in closely packed configurations of various geometrical distributions. Every defect on each lattice site acts as a spin-to-orbital momentum coupler and can be harnessed either via optical addressing or by tuning the voltage applied to the light valve. These photonic structures, easily reconfigurable and self-healing, can encompass the parallel processing of a large number of optical signals.

U. B., S. R., and M. G. C. acknowledge financial support from the ANR international program, Project No. ANR-2010-INTB-402-02 (ANR-CONICYT39), "COLORS," and FONDECYT No. 1120320. R. B. and G. A. acknowledge travel funding from the Internationalization Program of University Roma Tre.

[1] J. F. Nye and M. V. Berry, Proc. R. Soc. A **336**, 165 (1974).

[2] L. M. Pismen, *Vortices in Nonlinear Fields* (Oxford Science Publications, New York, 1999).

[3] M. S. Soskin and M. V. Vasnetov, Prog. Opt. **42**, 219 (2001).

[4] A. S. Desyatnikov, Y. S. Kivshar, and L. Torner, Prog. Opt. **47**, 291 (2005).

[5] L. Allen, M. W. Beijersbergen, R. J. C. Spreeuw, and J. P. Woerdman, Phys. Rev. A **45**, 8185 (1992).

[6] D. G. Grier, Nature (London) **424**, 810 (2003).

[7] V. G. Shvedov, A. V. Rode, Y. V. Izdebskaya, A. S. Desyatnikov, W. Krolikowski, and Y. S. Kivshar, Phys. Rev. Lett. **105**, 118103 (2010).

[8] M. Padgett and R. Bowman, Nat. Photonics **5**, 343 (2011).

[9] H. H. Arnaut and G. A. Barbosa, Phys. Rev. Lett. **85**, 286 (2000).

[10] J. Wang, J.-Y. Yang, I. M. Fazal, N. Ahmed, Y. Yan, H. Huang, Y. Ren, Y. Yue, S. Dolinar, M. Tur, and A. E. Willner, Nat. Photonics **6**, 488 (2012).

[11] F. Tamburini, G. Anzolin, G. Umbriaco, A. Bianchini, and C. Barbieri, Phys. Rev. Lett. **97**, 163903 (2006).

[12] M. W. Beijersbergen, L. Allen, H. E. L. O. van der Veen, and J. P. Woerdman, Opt. Commun. **96**, 123 (1993).

[13] V. Y. Bazhenov, M. V. Vasnetsov, and M. S. Soskin, JETP Lett. **52**, 429 (1990).

[14] Z. Sacks, D. Rozas, and G. A. Swartzlander, J. Opt. Soc. Am. B **15**, 2226 (1998).

[15] L. Marrucci, C. Manzo, and D. Paparo, Phys. Rev. Lett. **96**, 163905 (2006).

[16] E. Brasselet, Phys. Rev. Lett. **108**, 087801 (2012).

[17] J. Hotta, K. Sasaki, and H. Masuhara, Appl. Phys. Lett. **71**, 2085 (1997).

[18] I. I. Smalyukh, D. S. Kaputa, A. V. Kachynski, A. N. Kuzmin, and P. N. Prasad, Opt. Express **15**, 4359 (2007).

[19] E. Serabyn, D. Mawet, and R. Burruss, Nature (London) **464**, 1018 (2010).

[20] R. Barboza, U. Bortolozzo, G. Assanto, E. Vidal-Henriquez, M. G. Clerc, and S. Residori, Phys. Rev. Lett. **109**, 143901 (2012).

[21] B. Senyuk, Q. Liu, S. He, R. D. Kamien, R. B. Kusner, T. C. Lubensky, and I. I. Smalyukh, Nature (London) **493**, 200 (2012).

[22] P. Pieranski, B. Yang, L.-J. Burtz, A. Camu, and F. Simonetti, Liq. Cryst. **2012**, 1 (2012).

[23] P. G. de Gennes and J. Prost, *The Physics of Liquid Crystals* (Oxford Science Publications, New York, 1993), 2nd ed.

[24] R. Barboza, T. Sauma, U. Bortolozzo, G. Assanto, M. G. Clerc, and S. Residori, New J. Phys. **15**, 013028 (2013).

[25] See Supplemental Material at http://link.aps.org/supplemental/10.1103/PhysRevLett.111.093902 for the complete model derivation.

[26] S. Chandrasekhar, *Liquid Crystals* (Cambridge University Press, New York, 1977), p. 119.

[27] M. S. Soskin, V. G. Denisenko, and R. I. Egorov, Proc. SPIE Int. Soc. Opt. Eng. **5458**, 79 (2004).

[28] L. Marrucci, Mol. Cryst. Liq. Cryst. **488**, 148 (2008).

[29] See Supplemental Material at http://link.aps.org/supplemental/10.1103/PhysRevLett.111.093902 for a movie that shows an example of the unwinding dynamics of a defect under topological frustration.

Appendix C

Symmetry breaking of nematic umbilical defects through an amplitude equation

This Appendix is the paper entitled "Symmetry breaking of nematic umbilical defects through an amplitude equation" published in Physical Review E.

PHYSICAL REVIEW E **90**, 012507 (2014)

Symmetry breaking of nematic umbilical defects through an amplitude equation

Marcel G. Clerc[*] and Estefania Vidal-Henriquez
Departamento de Física, Facultad de Ciencias Físicas y Matemáticas, Universidad de Chile, Casilla 487-3, Santiago, Chile

Juan Diego Davila and Michał Kowalczyk
Departamento de Ingeniería Matemática and CMM, Universidad de Chile, Casilla 170 Correo 3, Santiago, Chile

(Received 23 April 2014; published 18 July 2014)

The existence, stability properties, and bifurcation diagram of the nematic umbilical defects is studied. Close to the Fréedericksz transition of nematic liquid crystals with negative anisotropic dielectric constant and homeotropic anchoring, an anisotropic Ginzburg-Landau equation for the amplitude of the tilt of the director away from the vertical axis is derived by taking the three-dimensional (3D) to 2D limit of the Frank-Oseen model. The anisotropic Ginzburg-Landau equation allows us to reveal the mechanism of symmetry breaking of nematic umbilical defects. The positive defect is fully characterized as a function of the anisotropy, while the negative defect is characterized perturbatively. Numerical simulations show quite good agreement with the analytical results.

DOI: 10.1103/PhysRevE.90.012507 PACS number(s): 61.30.Jf, 05.45.−a

I. INTRODUCTION

Macroscopic systems with injection and dissipation of energy and momenta exhibit instabilities leading to spontaneous symmetry breaking and pattern formation [1]. Due to the inherent fluctuations of these macroscopic systems, different organizations may emerge in distinct regions of the same sample; hence, spatial structures are usually characterized by domains, separated by interfaces, as grain boundaries, defects, or dislocations [2,3]. Among others, defects in rotationally invariant two-dimensional (2D) systems, i.e., vortices, attract a great deal of attention because of their universal character, as they are solutions of the complex Ginzburg-Landau equation (CGLE) that describes such different systems as fluids, superfluids, superconductors, liquid crystals, fluidized anisotropic granular matter, magnetic media, and optical dielectrics, to mention a few [4]. Vortices occur in complex fields and can be identified as topological defects, that is, pointlike singularities, which locally break the symmetry. They exhibit a zero intensity at the singular point with a phase spiraling around it. The topological charge is assigned by counting the number of spiral arms in the phase distribution, while the sign is given by the sense of the spiral rotation.

Nematic liquid crystals with negative anisotropic dielectric constant and homeotropic anchoring are a natural physical context where dissipative vortices are observed [5,6]. Figure 1 shows the typically observed vortices and schematic representations in two and three dimensions of these defects. Umbilical defects in nematic liquid crystals have long been reported in the literature (see textbooks [5–7] and references therein). Two types of stable vortices with opposite charges are observed [see Fig. 1(c)], which are characterized by being attracted (repulsed) to the opposite (identical) topological charge. The nematic liquid crystal phase is characterized by rod-shaped molecules that have no positional order but tend to point in the same direction. Then, the description of the nematic liquid crystal is given by a vector—the director $\vec{n}$—which accounts for the molecular order. Note that the defects observed in this context are strongly dissipative, compared to those observed in magnetic systems, superfluids, superconductors, and Bose-Einstein condensates. Even so, the vortexlike defects have accompanied liquid crystals since their discovery in 1889 by Lemman [8], who called these structures kernels. Later, they were observed in a similar experimental setup by Freidel, who called these defects *noyaux* [9]. Moreover, he also resolved their detailed topological structure. From the theory of elasticity of nematics liquid crystals Frank calculated the detailed structure of these defects [10]. Due to the fact that these defects break the orientational order and by analogy with dislocations in crystals of condensed matter, Frank called these defects disclinations. Despite the different names given to the observed vortices in this context, none of them were adopted by the community of liquid crystals. There the most widely used name for these defects is nematic umbilical defects. The term umbilics was coined by Rapini [11] and refers to the topological structure of the defect, which corresponds to a stringlike object in three dimensions [see Fig. 1(b)]. Because of the complex elasticity theory associated with nematic liquid crystals, characterized by three types of deformation (blend, twist, and splay), the dynamic study of defects is a thorny task [5–7]. A simple and universal strategy to study and characterize these defects and their dynamics is to analyze their behavior near the orientational instability of the molecules, which is called Fréedericksz transition [5,6]. Close to this transition the dynamics of the director can be reduced at main order to the Ginzburg-Landau equation with real coefficients [12,13]. This amplitude equation allows us to understand the emergence of different orientational domains, two types of stable vortices, and their respective dynamics. Since the vortices have a $\pm 2\pi$ phase jump (winding number), usually they are referred to as vortex $+$ and $-$, respectively. In this approach, however, both defects are indistinguishable in their amplitude and, as a result of the phase invariance of the Ginzburg-Landau equation, they account for a continuous family of solutions, characterized by a phase parameter. Notwithstanding, as a result of the inherent anisotropy of liquid crystals these defects can be distinguished experimentally.

---

[*] marcel@dfi.uchile.cl

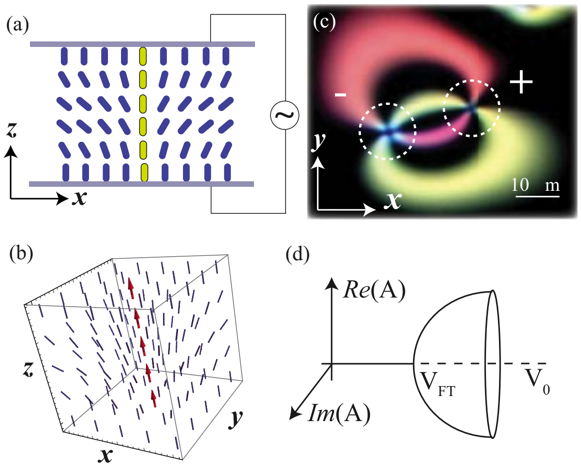

FIG. 1. (Color online) Nematic umbilical defects. (a) Schematic representation of the system under study, the rods describe the orientation of the director and the gray rods (green rods) stand for the vortex position. (b) Three-dimensional representation of the nematic umbilical defect, where arrows stand for the position of the defect. (c) Experimental image of umbilical defects. (d) Bifurcation diagram of a degenerate pitchfork bifurcation with $O(2)$ symmetry.

Figure 1(c) shows an image obtained using two crossed polarizers where one can distinguish between different defects, in which one exhibits a variety of different colors.

The aim of this manuscript is to investigate the existence, stability properties, and bifurcation diagram of the nematic umbilical defects through amplitude equations. Several studies have been performed using variational methods in the free energy of Frank [11,14], however there is no complete characterization of the nematic umbilical defects. Close to the Fréedericksz transition of nematic liquid crystals with negative anisotropic dielectric constant and homeotropic anchoring, an anisotropic Ginzburg-Landau equation for the transversal critical mode is derived by taking the 3D to 2D limit of the Frank-Oseen model. This model allows us to reveal the mechanism of symmetry breaking of nematic umbilical defects. The defect with positive charge is fully characterized as a function of the anisotropy, while the negative defect is characterized perturbatively. In particular, only a discrete number of solutions of the continuous family of defect persists when anisotropy is taken into account.

II. AMPLITUDE EQUATION CLOSE TO THE FRÉEDERICKSZ TRANSITION

Let us consider a nematic liquid crystal layer with negative anisotropic dielectric constant and homeotropic anchoring under the influence of high-frequency electrical tension (kHz). Figure 1(a) shows schematically the liquid crystal layer, where the rods account for the orientation of the director $\vec{n}(\mathbf{r},t)$ and $\{\mathbf{r},t\}$ describe the space and time, respectively. To understand the dynamical behavior of umbilical defects, we derive a model in the vicinity of the Fréedericksz transition, a limit where analytical results are accessible as nematic liquid crystal molecules are weakly tilted from the longitudinal axis $\hat{z}$ and backflow effects can safely be neglected. The dynamical equation for the molecular director $\vec{n}$ reads (the Frank-Oseen model) [6]

$$\begin{aligned}\gamma\partial_t\vec{n} = {} & K_3[\nabla^2\vec{n}-\vec{n}(\vec{n}\cdot\nabla^2\vec{n})]\\ & +(K_3-K_1)[\vec{n}(\vec{n}\cdot\vec{\nabla})(\vec{\nabla}\cdot\vec{n})-\vec{\nabla}(\vec{\nabla}\cdot\vec{n})]\\ & +(K_2-K_3)[2(\vec{n}\cdot\vec{\nabla}\times\vec{n})(\vec{n}(\vec{n}\cdot\vec{\nabla}\times\vec{n})-\vec{\nabla}\times\vec{n})\\ & +\vec{n}\times\vec{\nabla}(\vec{n}\cdot\vec{\nabla}\times\vec{n})]+\epsilon_a(\vec{n}\cdot\vec{E})[\vec{E}-\vec{n}(\vec{n}\cdot\vec{E})], \quad (1)\end{aligned}$$

where γ is the relaxation time, ϵ_a is the anisotropic dielectric constant that accounts for nonlinear response of the dielectric constant, $\{K_1,K_2,K_3\}$ are the nematic liquid crystal elastic constants, which account for the elastic deformation of splay, twist, and bend type, respectively. The electric field is given by $\vec{E}=(V/d)\hat{z}\equiv E_z\hat{z}$, where E_z is the root mean square amplitude of the electric field, V is the applied voltage and d is the width of the liquid crystal layer.

A. Amplitude equation close to Fréedericksz transition

A trivial equilibrium of the liquid crystal layer is the homeotropic state, $\vec{n}=\hat{z}$. This state undergoes a degenerate stationary instability when the anisotropic dielectric constant is negative ($\epsilon_a<0$) for critical values of the voltage, which match the Fréedericksz transition threshold $V_{FT}=\sqrt{-K_3\pi^2/\epsilon_a}$. Then, the director undergoes orientational instability, i.e., the molecules do not want to align with the electric field. As a result of elastic coupling between the molecules, the director has a cone of possible equilibria. From the point of view of bifurcation theory, this instability corresponds to a degenerate pitchfork bifurcation with $O(2)$ symmetry [3]. Figure 1(d) outlines the bifurcation diagram for this instability.

Close to the transition point, we introduce the ansatz

$$\vec{n}=\begin{pmatrix} n_x(\vec{r},\pi z/d,t)\\ n_y(\vec{r},\pi z/d,t)\\ \sqrt{1-\left(n_x^2+n_y^2\right)}\end{pmatrix},$$

with $\vec{r}=(x,y)\in\Omega\subset\mathbb{R}^2$ the transverse coordinates, $z\in(-1/2,1/2)$ and the parameter $d\ll 1$ measures the thickness of the liquid crystal sample (which is conveniently taken to be equal to πd). Now the idea is to take the 3D to 2D limit of Eq. (1) near the Fréedericksz point, or in other words take the limit $d\to 0$. To do this we assume that the voltage has the following expansion

$$V=V_{FT}+d^2V_1+\cdots,\quad V_1>0.$$

We introduce the new variable $\zeta=z/d$ and write the ansatz in a more explicit form

$$n_x(\vec{r},\zeta,t)=d^2u_0(\vec{r},t)\cos(\pi\zeta)+d^4u_1(\vec{r},t)\vartheta(\pi\zeta)+\cdots,$$

$$n_y(\vec{r},\zeta,t)=d^2v_0(\vec{r},t)\cos(\pi\zeta)+d^4v_1(\vec{r},t)\vartheta(\pi\zeta)+\cdots,$$

$$n_z(\vec{r},\zeta,t)=\sqrt{1-\left(n_x^2+n_y^2\right)},$$

where $\vartheta(\pi\zeta)$ is a function to be determined. Next, we substitute these expressions in Eq. (1) and compare terms with equal powers of d. This allows us to have a hierarchy of equations. It turns out that the $\mathcal{O}(1)$ term in the direction of the vector $\hat{x} = (1,0,0)$ satisfies

$$K_3 d^{-2}\partial^2_{\zeta\zeta} n_x + \epsilon_a V_{FT}^2 d^{-2} n_x = u_0\big(-K_3\pi^2 - \epsilon_a V_{FT}^2\big) = 0,$$

because of the choice of V_{FT}. Hence, this condition corresponds to impose that the voltage is in the Fréedericksz transition. A similar equation holds in the $\hat{y} = (0,1,0)$ direction. Note that this does not allow us to determine the functions u_0 and v_0. As is the case in the standard formal asymptotic expansion of a homogenization problem, these functions are determined as solvability conditions for the equations corresponding to $\mathcal{O}(d^2)$ order. Indeed, at this order we have to solve, say in the direction of $\hat{x}$, a linear problem for the function ϑ, which is of the form

$$u_1\big[K_3\partial^2_{\zeta\zeta} - \epsilon_a V_{FT}^2\big]\vartheta = g_x(\vec{r},\pi\zeta,t),$$

and this last equation can be solved uniquely if

$$\int_{-1/2}^{1/2} g_x(\vec{r},\pi\zeta,t)\cos(\pi\zeta)\,d\zeta = 0.$$

We show in the Appendix that this, and a similar condition in the $\hat{y}$ direction lead to the following equation for the order parameter $w_0 \equiv u_0 + i v_0$:

$$\begin{aligned}\gamma\partial_t w_0 = {} & \tfrac{1}{2}(K_1 + K_2)\nabla^2_\perp w_0 + \tfrac{1}{2}(K_1 - K_2)\partial^2_{\eta\eta}\bar{w}_0 \\ & - K_3\pi^2 w_0|w_0|^2 - \epsilon_a V_{FT} V_1 w_0, \end{aligned} \qquad (2)$$

where $\bar{w}_0$ stands for the complex conjugate of w_0, $\partial_\eta \equiv \partial_x + i\partial_y$ and $\nabla^2_\perp \equiv \partial_{xx} + \partial_{yy} = \partial_\eta\partial_{\bar{\eta}}$.

We change variables

$$w_0(\vec{r},t) \longmapsto \frac{1}{\pi}\sqrt{\frac{K_1 + K_2}{K_3}}\,A[\vec{\rho},(K_1 + K_2)t/2\gamma],$$

and let $\delta = (K_1 - K_2)/(K_1 + K_2)$. Denoting the new time variable by t again we obtain an anisotropic complex Ginzburg-Landau equation:

$$\partial_t A = \mu_0 A - |A|^2 A + \nabla^2_\perp A + \delta\partial^2_{\eta\eta}\bar{A}, \qquad (3)$$

where

$$\mu_0 = \frac{2|\epsilon_a| V_{FT} V_1}{K_1 + K_2}$$

is the bifurcation parameter and $\delta \in [-1,1]$ accounts for the elastic anisotropy.

Similar equations were derived before: using the method of amplitude equations for nematic liquid crystals near the Fréedericksz transition [13] (see also [12]), and for modeling self-organization in an array of microtubules interacting via molecular motors in Ref. [15].

Note that Eq. (3) can be rewritten in the form

$$\partial_t A = -\frac{\delta\mathcal{E}}{\delta\bar{A}}, \qquad (4)$$

where the free energy is

$$\mathcal{E}(A,\delta) \equiv \int_\Omega dS\left[|\nabla A|^2 + \frac{1}{2}(\mu_0 - |A|^2)^2 + \delta\mathrm{Re}\{(\partial_\eta\overline{A})^2\}\right], \qquad (5)$$

where $\Omega \subset \mathbb{R}^2$ is a bounded domain. In other words the time-dependent anisotropic Ginzburg-Landau Eq. (3) is simply a gradient flow of the free energy. Obviously $\mathcal{E}$ is a Lyapunov functional, i.e.,

$$\begin{aligned}\frac{d\mathcal{E}}{dt} &= \int_\Omega ds\left(\frac{\delta\mathcal{E}}{\delta A}\partial_t A + \frac{\delta\mathcal{E}}{\delta\bar{A}}\partial_t\bar{A}\right), \\ &= -2\int_\Omega ds\,\frac{\delta\mathcal{E}}{\delta A}\frac{\delta\mathcal{E}}{\delta\bar{A}} \leq 0. \end{aligned} \qquad (6)$$

The trivial equilibria that minimize the free energy are $|A|^2 = \mu_0$. However, as we will see this equation has nontrivial inhomogeneous equilibria.

B. Isotropic limit: Ginzburg-Landau equation

Considering the isotropic limit ($K_1 = K_2 = K_3$), $\delta = 0$, the above model reduces to the well-known complex Ginzburg-Landau equation with real coefficients

$$\partial_t A = \mu_0 A - |A|^2 A + \nabla^2_\perp A. \qquad (7)$$

This model has gathered a great interest by describing several physical systems such as fluids, superfluids, superconductors, liquid crystals, magnetic media, and optical cavity, to mention a few [4]. The main properties of the complex Ginzburg-Landau equation are reported in the review [16]. This equation admits stable dissipative vortex solutions with topological charge ±1 [2,4]. Figure 2 illustrates the vortex solution with negative topological charge. If one considers polar representation $A = R_v(r)e^{i(m\varphi+\varphi_0)}$, where $m = \pm 1$ is the topological charge, (r,φ) are the polar coordinates in the plane and φ_0 is a continuous parameter that accounts for the phase invariance of the above amplitude Eq. (7). The magnitude $R_v(r)$ satisfies

$$\mu_0 R_v - R_v^3 - \frac{m^2}{r^2}R_v + \frac{1}{r}\frac{dR_v}{dr} + \frac{d^2 R_v}{d^2 r} = 0. \qquad (8)$$

There are no analytical expressions for the defect solutions of this model, which were first observed numerically in Ref. [17]. However, one has the asymptotic behavior

$$R_v(r) \approx \begin{cases}\alpha_m r^{|m|} + \cdots, & r \longrightarrow 0, \\ \sqrt{\mu_0} - \frac{m^2}{2}r^{-2} + \cdots, & r \longrightarrow \infty,\end{cases}$$

where $\alpha_m > 0$ is a constant that depends on μ_0 as well.

By using Padé approximants, one can obtain suitable approximations for the vortices [2]. There is a long history of literature devoted to the rigorous study of vortices in complex Ginzburg-Landau equation (see Ref. [18] and references therein). Note that the equation for the modulus of the amplitude does not depend on the sign of the topological charge. Hence, both vortices are indistinguishable from the point of view of their magnitude.

In order to characterize the arms of the vortex and to allow a comparison with the experimental observations obtained by using cross polarizers, let us introduce the nullcline field $\psi(r,\theta) \equiv \mathrm{Re}(A)\mathrm{Im}(A)$. This auxiliary field becomes zero when the real or imaginary part of A vanishes. Then, the arms and position of the vortex are represented, respectively, by the zero and the intersection of the zero nullcline curves. Figure 2(c) shows the nullcline field obtained by using the above Ginzburg-Landau equation (7). Note that both defects are still indistinguishable (see Fig. 2), however these defects

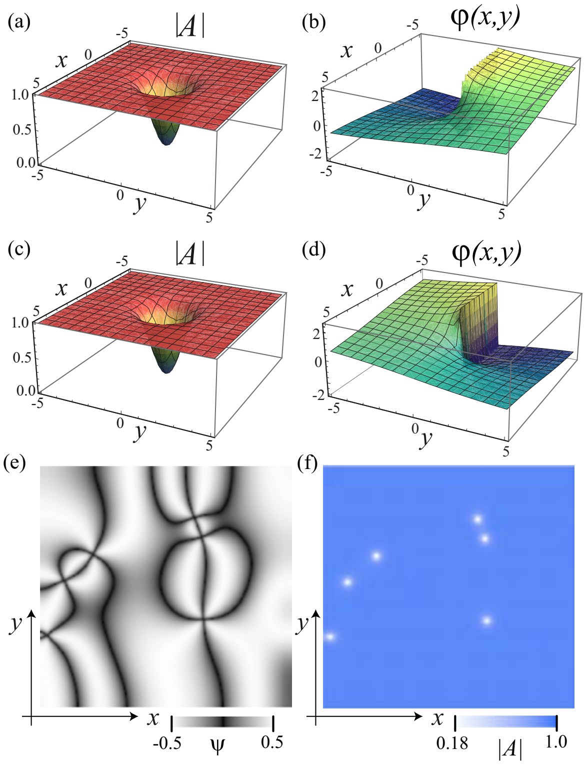

FIG. 2. (Color online) Vortex solution of Ginzburg-Landau equation (7) with $\mu_0 = 1$ (from numerical simulations). Structure of the magnitude (a) and phase of the positive vortex (b). Structure of the magnitude (c) and phase of the negative vortex (d). (e) Nullcline field, $\psi(x,y,t) = \mathrm{Re}(A)\mathrm{Im}(A)$ at given time. This field is equivalent to the light intensity observed when one considers crossed polarizers on an experimental setup. (f) Modulus of the amplitude A at given time.

are experimentally distinguishable [see Fig. 1(c)] [11,14,21]. The different colors observed experimentally are due to the different optical paths produced by the different orientations of the molecules. Moreover, from the Ginzburg-Landau equation, one deduces that the interaction between vortices is symmetric [4,22], however it has been reported that the speed of umbilic defects in the process of collision is different [23]. Numerical simulations considering the dynamic of the nematic liquid crystal show the same result, where the speed asymmetry arises from backflow effects and anisotropy in the elastic constants [23].

The Ginzburg-Landau equation is invariant under the following symmetries: $\vec{r} \longrightarrow \vec{r} + \vec{r}_0$ (spatial translation invariance), $\varphi \longrightarrow \varphi + \varphi_0$ (coordinates rotation), $\varphi \longrightarrow -\varphi$ (coordinates reflection), $A \longrightarrow Ae^{i\varphi_0}$ (phase invariance), and $A \longrightarrow \bar{A}$ (reflection invariance).

III. ANISOTROPY INDUCES SYMMETRY BREAKING

A. Fourfold symmetry of the energy and its consequences

For the purpose of the following discussion we assume that $\mu_0 = 1$. Let us now consider the effect of the anisotropy of the elastic constants ($\delta \neq 0$). From the point of view of symmetries, equation (7) as well as the free energy $\mathcal{E}$ are still invariant under spatial translation, but phase invariance and coordinates rotation are no longer valid symmetries. They are replaced by a joint symmetry $A(z,t) \longrightarrow A(ze^{-i\varphi_0},t)e^{i\varphi_0}$ (z is the complex variable that represents the Cartesian plane). Using the notation $\mathcal{R}_{\varphi_0}$ for the rotation by the angle φ_0 of $\mathbb{R}^2$ about the origin, a short calculation shows however that we still have:

$$\mathcal{E}(A,\delta) = \mathcal{E}(A \circ \mathcal{R}_{\varphi_0}, -\delta) = \mathcal{E}(\mathcal{R}_{\varphi_0} A, -\delta),$$

when $\varphi_0 = \pi/2$. This is best seen if we notice that with $A = u + iv$ we have

$$\mathcal{E}(A,\delta) = \int_\Omega dS[(1+\delta)(u_x + v_y)^2 + (1-\delta)(u_y - v_x)^2] + \frac{1}{4}\int_\Omega dS[1 - (u^2 + v^2)]^2.$$

We say that $\mathcal{E}$ has a fourfold symmetry in the sense that

$$\mathcal{E}(A,\delta) = \mathcal{E}[\mathcal{R}_{m\pi/2} A \circ \mathcal{R}_{k\pi/2}, (-1)^{m+k}\delta]. \tag{9}$$

This formula relates different equations and energies when $m + k$ is odd, and at the same time it shows that energy and bifurcation diagrams have to be even symmetric with respect to $\delta = 0$. Functionals with fourfold symmetries appear for instance in the so-called d-wave Ginzburg-Landau equation, see for instance Refs. [19,20] and the references therein.

The presence of anisotropy also breaks the symmetry between the vortices with positive and negative charge. To give a first insight into this issue let us suppose that $\Omega = B_L$ is a ball of radius L centered at the origin. Consider a function f defined in Ω with Fourier series expansion

$$f(z) = \sum_{n=-\infty}^{\infty} f_n(r) e^{in\theta},$$

with $z = re^{i\theta}$. Now, if $f(z)$ has the form

$$f(z) = \sum_{n=-\infty}^{\infty} f_{4n\pm1}(r) e^{i(4n\pm1)\theta},$$

that is, only modes indexed by $4n \pm 1$ are present, it can be checked that

$$\Delta u + \delta\partial_{\eta\eta}\bar{u} + u(1 - |u|^2)$$

has an expansion where again only modes $4n \pm 1$ appear. With this in mind we can define A to be a vortex solution with unit positive charge if its Fourier series has the terms indexed by $4n + 1$ and $f_1'(0) \neq 0$, and unit negative charge if its series has the terms $4n - 1$ and $f_{-1}'(0) \neq 0$.

Figure 3 illustrates the vortices with positive and negative topological charge found in the asymmetric Giznburg-Landau equation (3). Note that from the nullcline field $\psi(r,t)$ it is not possible to differentiate these vortices, compared to the magnitude field $|A(r,t)|$ where they are distinguishable (cf. Fig. 3). For the vortex with charge $+1$, the modulus remains rotationally invariant, while for the -1 vortex the rotational invariance around the core is broken by the fourfold symmetry. Indeed, in a single color map representation of $|A|$, one can identify the positive and negative charges on their circular and

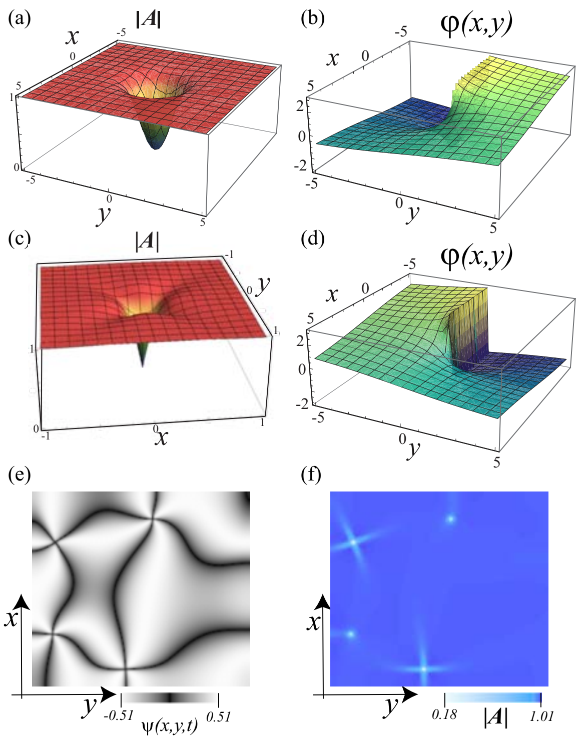

FIG. 3. (Color online) Vortex solution of the anisotropic Ginzburg-Landau equation (3) with $\mu_0 = 1$ and $\delta = 0.7$ (from numerical simulations). Structure of the magnitude (a) and phase of the positive vortex (b). Structure of the magnitude (c) and phase of the negative vortex (d). (e) Colormap of nullcline field $\psi(x,y,t) = \mathrm{Re}(A)\mathrm{Im}(A)$ and (f) modulus of the amplitude A at given time.

cross structure, respectively [cf. Fig. 3(d)]. Note that when one increases the anisotropy, the size of the cross structure grows. Below, we study the properties of each of the vortices.

B. Vortex with positive charge

By introducing the ansatz $A(r,\theta,\{\varphi_0\}) = R(r)e^{i(\theta+\varphi_0)}$ in the anisotropic Ginzburg-Landau equation (3), for the vortex solution with positive topological charge, we obtain the following set of scalar equations

$$0 = \mu_0 R - R^3 + (1+\delta e^{-2i\varphi_0})\left(\frac{d^2R}{d^2r} + \frac{1}{r}\frac{dR}{dr} - \frac{R}{r^2}\right) \tag{10}$$

$$0 = \delta \sin 2\varphi_0 \left(\frac{d^2R}{d^2r} + \frac{1}{r}\frac{dR}{dr} - \frac{R}{r^2}\right). \tag{11}$$

From Eq. (11), the only possibility to obtain a nontrivial solution is to consider the phase parameter satisfying $\sin 2\varphi_0 = 0$, which gives the discrete solutions $\varphi_0 = \{0,\pi/2,\pi,3\pi/2\}$, and which is of course consistent with the fourfold symmetry mentioned above. Therefore, from the continuous family of possible phase jumps only four possibilities survive. On the other hand, the equation for the magnitude of the amplitude reads

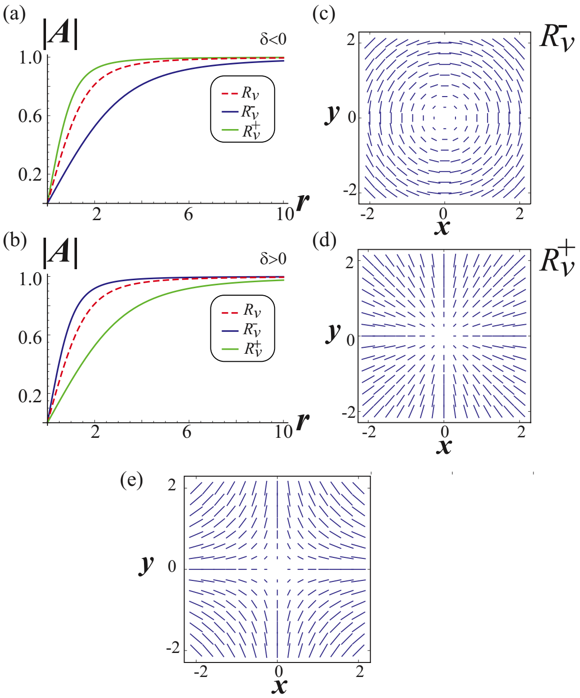

FIG. 4. (Color online) Vortex solution with positive topological charge of the anisotropic Ginzburg-Landau equation (3) with $\mu_0 = 1$ and $\delta = 0.1$. Magnitude of the vortex with positive (a) and negative (b) anisotropy, respectively. The dashed curve stands for the magnitude of the vortex for isotropic systems ($\delta = 0$). (c) and (d) schematic representation of the orientation field $A(r,\theta,\{\varphi_0\})$ for different values of φ_0: R_v^- ($\varphi_0 = \pi/2$) and R_v^+ ($\varphi_0 = 0$). (e) Schematic representation of the orientation amplitude field for the negative topological charge.

$$0 = \mu_0 R - R^3 + (1+\delta\cos 2\varphi_0)\left(\frac{d^2R}{d^2r} + \frac{1}{r}\frac{dR}{dr} - \frac{R}{r^2}\right). \tag{12}$$

Since $\varphi_0 = \{0,\pi/2,\pi,3\pi/2\}$, we must have $\cos 2\varphi_0 = \pm 1$. Rescaling the space by the factor $\sqrt{1\pm\delta}$, the above equation becomes Eq. (8). Therefore, the isotropic positive vortex has the form

$$A = R_v^{\pm}\left(\frac{r}{\sqrt{1\pm\delta}}\right)e^{i(\theta+\frac{\pi}{4}\mp\frac{\pi}{4}+n\pi)}, \tag{13}$$

with R_v the magnitude of the vortex solution of the Ginzburg-Landau equation and $n = 0,\pm1,\pm2,\ldots$. Consequently, the anisotropic vortex solution with positive charge corresponds to a simple scaling of the isotropic vortex solution, notwithstanding, with a finite number of possible phase jumps ($\varphi_0 = \{0,\pi/2,\pi,3\pi/2\}$), in opposition, to the isotropic system, which has an infinite number of solutions parameterized by the continuous parameter φ_0. Figure 4 illustrates the magnitude of a vortex with positive topological charge solution for the asymmetric Ginzburg-Landau equation (3), for positive and negative anisotropy. Note that the difference between the vortices R_v^+ and R_v^- in the amplitude are their different sizes of the vortex core. For positive (negative) anisotropy the largest core is for vortex R_v^+ (R_v^-). Also, due to the different φ_0, both vortices represent different configurations for the director orientation [cf. Figs. 4(c) and 4(d)].

It is worth noting that it is known, from the variational approach to the Frank free energy, that the elastic anisotropy allows a discrete number of four possible phase jumps for umbilical defects with positive topological charge [11,14]. These features are recovered by the analytical expression (13). In the context of self-organization of an array of microtubules interacting via molecular motors similar configurations have been numerically found for the orientational field with $\varphi_0 = 0$ and $\varphi_0 = \pi/2$, which have been denominated, respectively, *aster* and *ideal vortex* [15]. Notice that these configurations and their continuous deformation are vortex solutions like Frank remarked at the dawn of the theory of liquid crystals [10].

C. Free-energy analysis

In order to study the existence, stability properties and bifurcation diagram of the vortex solution with positive topological charge, one can analyze the properties of the free energy $\mathcal{E}$, expression (5). Using the vortex solution $A = R_v^{\pm}(r/\sqrt{1\pm\delta})e^{i(\theta+\varphi_0)}$, where the $\pm$ sign stands for $+$ for $\varphi_0 = \{0,\pi\}$ and $-$ for $\varphi_0 = \{\pi/2, 3\pi/2\}$, and taking $\Omega = B_L$ we obtain

$$\mathcal{E} = \pi \int_0^L \left\{ (\partial_r R_v)^2 + \frac{R_v^2}{r^2} + \frac{1}{2}\left(1 - R_v^2\right)^2 + \delta\cos(2\varphi_0)\left(\partial_r R_v + \frac{R_v}{r}\right)^2 \right\} r dr, \qquad (14)$$

changing variables $\rho = r/\sqrt{1\pm\delta}$, we obtain

$$\mathcal{E} = \pi \int_0^{L/\sqrt{1\pm\delta}} \left\{ (\partial_\rho R_v(\rho))^2 + \frac{R_v^2(\rho)}{\rho^2} + \frac{(1\pm\delta)\left(1 - R_v^2(\rho)\right)^2}{2} \pm \delta\left(\partial_\rho R_v(\rho) + \frac{R_v(\rho)}{\rho}\right)^2 \right\} \rho d\rho, \qquad (15)$$

after straightforward calculations and following the same strategy presented in Ref. [4], we derive the energy of the vortex with positive topological charge

$$\mathcal{E} = \pi \ln\left(\frac{L}{a_0\sqrt{1\pm\delta}}\right) + \frac{\pi(1\pm\delta)}{2} \pm \pi\delta\left(\ln\left(\frac{L}{a_0\sqrt{1\pm\delta}}\right) + 1\right). \qquad (16)$$

Figure 5 shows the energy for the two different vortices with positive topological charge (two respective signs). The lines and geometrical symbols represent, respectively, the energy obtained using formula (16) and obtained from numerical simulations of Eq. (3). The numerical results show quite good agreement with the analytical expressions. Note that this figure shows that the scaling $\sqrt{1\pm\delta}$ that makes the core smaller is the one with less energy and, therefore, preferred by the system. Therefore, if $\delta < 0$ ($\delta > 0$) the solution with minimal energy is the one with $\varphi_0 = \{0,\pi\}$ ($\varphi_0 = \{\pi/2, 3\pi/2\}$). Numerical simulations of the anisotropic Ginzburg-Landau equation (3) show that the vortices with positive topological charge and large core are unstable. Thus, the stable vortices are those with small core. The respective stability of these solutions is represented by continuous (stable) and dashed (unstable) lines in Fig. 5. One expects that vortices with small core are the more stable, because the energy privileges the uniform state $|A|^2 = \mu_0$.

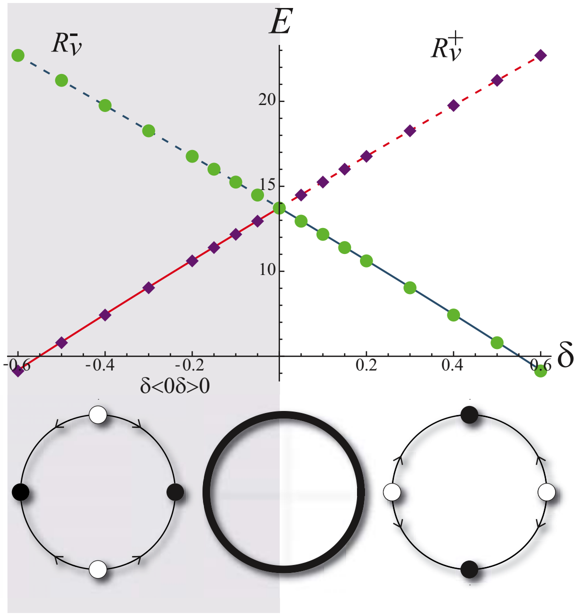

FIG. 5. (Color online) Energy of the positive vortex solutions for different jump phase φ_0 as function of δ. Numerical results obtained from vortex solutions of Eq. (3) are shown by the geometrical symbols (circles and diamonds) and the theoretical result obtained from expression (16) by a continuous and dashed line. The continuous and dashed line indicate, respectively, the stable and unstable vortex solution with positive topological charge. The bottom panel schematically illustrates the bifurcation diagram for the phase jump φ_0, which correspond to a degenerate transcritical bifurcation. The dark and white circles account for stable and unstable vortices solutions.

D. Bifurcation diagram

The above analysis shows that there are two positive vortex solutions that exist for every value of δ. These phase singularity solutions exchange stability in the isotropic limit ($\delta = 0$), where $\varphi_0 = \{0,\pi\}$ goes from stable to unstable solution, and vice versa for $\varphi_0 = \{\pi/2, 3\pi/2\}$. The mechanism through which these solutions exchange stability is not by the usual collision of solutions of the transcritical bifurcation [24,25], but rather by passing through a very degenerate point at $\delta = 0$, where an infinite number of solutions exist and φ_0 can take any continuous value between 0 and 2π. Hence, this bifurcation is a degenerate transcritical bifurcation and it is schematically shown in the bottom panel in Fig. 5, where the dark and white circles account for stable and unstable vortex solutions, respectively.

In brief, we have shown that the anisotropic elasticity is responsible for the dissimilarity of the defects with different topological charges. One possible experimental protocol for characterizing several properties of these nematic umbilical defects is through the use of crossed circular polarizers [21] and modification of the elastic constants by changing the temperature. Temperature allows to handle the values of elastic anisotropy constants. In particular, the elastic constants are quite sensitive to temperature near to the nematic-smectic transition [5].

IV. NEGATIVE VORTEX SOLUTION

The above analysis yields a complete description of vortices with topological charge +1. As we have mentioned, in vortices with negative topological charge, their rotational invariance around the core is broken by a fourfold symmetry (see Fig. 3). We will consider the strategy of perturbative analysis of these phase singularity solutions for small anisotropy ($\delta \ll 1$). Hence, we consider the following ansatz

$$A(r,\theta) \approx [R_v(r) + \delta g(r,\theta) + O(\delta^2)]e^{-i[\theta-\delta\Theta(r,\theta)]}, \tag{17}$$

where $g(r,\theta)$ and $\Theta(r,\theta)$ are dominate correction functions to the isotropic negative vortex, and with the condition that Θ has no topological charge, i.e.,

$$\oint_\Gamma \nabla\Theta \cdot d\vec{l} = 0, \tag{18}$$

where the path Γ encircles the core of the vortex. Using the above ansatz (17) in the anisotropic Ginzburg-Landau equation (3) and taking the leading order in δ, we obtain

$$\begin{aligned} 0 = e^{-i\theta}\bigg[&\mu_0 g - 3R_v^2 g + \frac{\partial^2 g}{\partial r^2} + 2i\frac{\partial\Theta}{\partial r}\frac{\partial R_v}{\partial r} \\ &+ iR_v\frac{\partial^2\Theta}{\partial r^2} + \frac{1}{r}\frac{\partial g}{\partial r} + \frac{iR_v}{r}\frac{\partial\Theta}{\partial r} + \frac{1}{r^2}\frac{\partial^2 g}{\partial\theta^2} \\ &- \frac{2i}{r^2}\frac{\partial g}{\partial\theta} + \frac{iR_v}{r^2}\frac{\partial^2\Theta}{\partial\theta^2} + \frac{2R_v}{r^2}\frac{\partial\Theta}{\partial\theta} - \frac{g}{r^2}\bigg] \\ &+ e^{3i\theta}\left[\frac{\partial^2 R_v}{\partial r^2} + \frac{3R_v}{r^2} - \frac{3}{r}\frac{\partial R_v}{\partial r}\right], \end{aligned} \tag{19}$$

separating the real and imaginary parts

$$\begin{aligned} 0 = {}&\mu_0 g - 3R_v^2 g + \frac{\partial^2 g}{\partial r^2} + \frac{1}{r}\frac{\partial g}{\partial r} + \frac{1}{r^2}\frac{\partial^2 g}{\partial\theta^2} + \frac{2R_v}{r^2}\frac{\partial\Theta}{\partial\theta} \\ &- \frac{g}{r^2} + \cos(4\theta)\left[\frac{\partial^2 R_v}{\partial r^2} + \frac{3R_v}{r^2} - \frac{3}{r}\frac{\partial R_v}{\partial r}\right], \end{aligned} \tag{20}$$

$$\begin{aligned} 0 = {}&2\frac{\partial\Theta}{\partial r}\frac{\partial R_v}{\partial r} + R_v\frac{\partial^2\Theta}{\partial r^2} + \frac{R_v}{r}\frac{\partial\Theta}{\partial r} + \frac{R_v}{r^2}\frac{\partial^2\Theta}{\partial\theta^2} \\ &- \frac{2}{r^2}\frac{\partial g}{\partial\theta} + \sin(4\theta)\left[\frac{\partial^2 R_v}{\partial r^2} + \frac{3R_v}{r^2} - \frac{3}{r}\frac{\partial R_v}{\partial r}\right]. \end{aligned} \tag{21}$$

The θ dependence is easily addressed doing variable separation, by setting $g(r,\theta) = g_4(r)\cos(4\theta)$ and $\Theta(r,\theta) = \theta_4(r)\sin(4\theta)$. Thus we obtain the following set of equations for the radial dependency

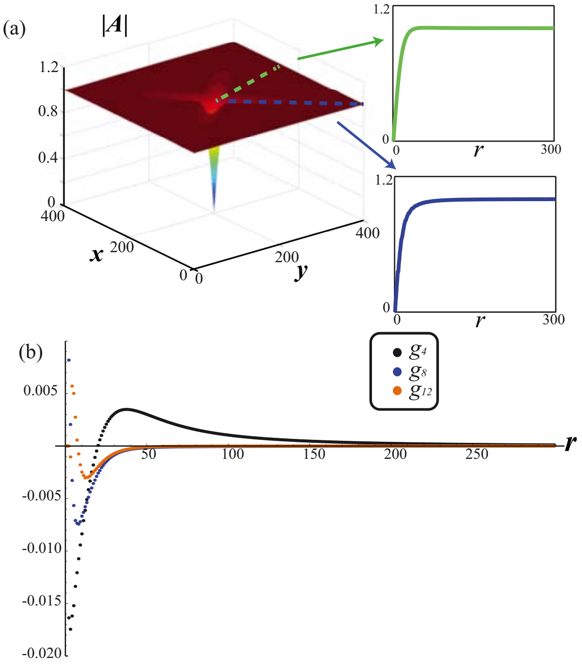

FIG. 6. (Color online) Vortex solution with negative topological charge of anisotropic Ginzburg-Landau equation (3) with $\mu_0 = 1$ and $\delta = 0.7$. (a) left panel magnitude of amplitude $|A|$ and right panels different radial profiles. (b) Numerical coefficients of the modal expansion (25).

$$\begin{aligned} 0 = {}&\mu_0 g_4 - 3R_v^2 g_4 + \frac{\partial^2 g_4}{\partial r^2} + \frac{1}{r}\frac{\partial g_4}{\partial r} - \frac{16 g_4}{r^2} \\ &+ \frac{8R_v\theta_4}{r^2} - \frac{g_4}{r^2} + \frac{\partial^2 R_v}{\partial r^2} + \frac{3R_v}{r^2} - \frac{3}{r}\frac{\partial R_v}{\partial r}, \end{aligned} \tag{22}$$

$$\begin{aligned} 0 = {}&2\frac{\partial\theta_4}{\partial r}\frac{\partial R_v}{\partial r} + R_v\frac{\partial^2\theta_4}{\partial r^2} + \frac{R_v}{r}\frac{\partial\theta_4}{\partial r} + \frac{8g_4}{r^2} \\ &- \frac{16R_v\theta_4}{r^2} + \frac{\partial^2 R_v}{\partial r^2} + \frac{3R_v}{r^2} - \frac{3}{r}\frac{\partial R_v}{\partial r}. \end{aligned} \tag{23}$$

As $r \to \infty$, the solution of this set of equations behaves as follows

$$g_4(r) \to \frac{9}{4r^2}, \quad \theta_4(r) \to \frac{3}{16}. \tag{24}$$

Then, the phase correction converges to a constant value. Using a variational approach to the Frank free energy far from the core of the vortex, neglecting the spatial dependence, and considering a modal angular expansion, one can recover the value of $\theta_4 = 3/16$ and $g_4 = 0$ [14]. However, this ansatz does not allow us to characterize the spatial structure of the negative vortex solution.

Asymptotically, the correction of the magnitude of the amplitude, $g_4(r)$, decreases as the inverse of the square of the distance. A numerical solution for $g_4(r)$ is shown in Fig. 6, which has quite good agreement with the above asymptotic expression. The magnitude of the amplitude of the phase singularity with negative topological charge as a function of the radial distance is not monotonous. However, this nonmonotonous feature is weak even for large δ [cf. Fig. 6(a)]. In order to investigate the spatial structure of the magnitude of the amplitude, we have considered the following modal angular expansion

$$|A(r,\theta)| = \sum_{n=2} g_n(r)\cos(n\theta), \tag{25}$$

where $g_n(r)$ are the coefficients of the expansion. Numerically, we have computed the coefficients for the expansion. Figure 6(b) shows some of these coefficients. One expects the mode $g_4(r)$ to be the dominant one even for larger δ as can be seen in Fig. 6(b). Hence, this mode is responsible for the fourfold symmetry of the vortex solutions with negative charge.

Note that in the perturbative analysis the phase jump, φ_0, is not predetermined, because if we consider a more general ansatz

$$A(r,\theta,\varphi_0) \approx [R_v(r) + \delta g(r,\theta)]e^{-i[\theta+\varphi_0-\delta\Theta(r,\theta)]}, \tag{26}$$

the previous analysis remains the same by setting $g(r,\theta) = g_4(r)\cos(4\theta + 4\varphi_0)$ and $\Theta(r,\theta) = \theta_4(r)\sin(4\theta + 4\varphi_0)$. Therefore, the vortex solution with negative topological charge is parametrized continuously by φ_0. Furthermore, when the anisotropy parameter δ is modified numerically, the vortex does not exhibit any bifurcation. Using the vortex solution with negative topological charge obtained numerically from the anisotropic Ginzburg-Landau equation (3) and evaluating the free energy $\mathcal{E}$, formula (5), we can reveal the dependence of the free energy as a function of the anisotropy, $\mathcal{E}(\delta)$. Figure 7 shows this function for various critical points of $\mathcal{E}$. The first observation we make is that the graph of the set $[\delta,\mathcal{E}(\delta)]$ is even. This is a general fact that follows immediately from the relation (9) with $m = 1$ and $k = 0$.

Second, the energy of the vortex with negative charge is exactly alike with the positive one only at $\delta = 0$. The vortex with positive topological charge is always more stable for anisotropic nematic liquid crystals. It is worthy to note that the vortices are always created by pairs to conserve the topological charge, even though one vortex has more energy than the other one. Furthermore, the scenario of the collision of opposite vortices described by isotropic Ginzburg-Landau (see Refs. [4,22] and references therein) does not account for the whole picture of the collision of opposite nematic umbilical defects as is shown in Ref. [23]. The characterization of vortex interaction in the anisotropic Ginzburg-Landau equation is in progress.

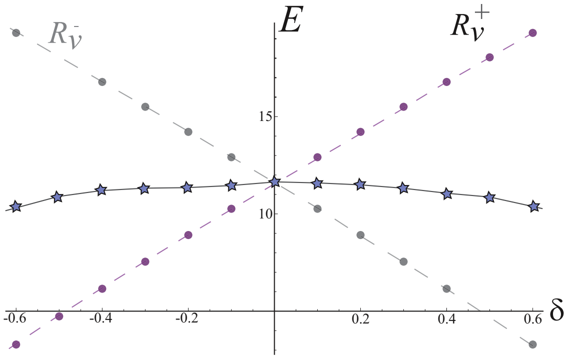

FIG. 7. (Color online) Energy of the vortex solutions as function of δ. The star symbols account for the free energy $\mathcal{E}$ obtained numerically using a vortex with negative topological charge and formula (5). The solid and dashed lines, drawn to guide the eye, show the evolution of the free energy of the vortices with topological negative and positive charge, respectively, as function of the anisotropy.

V. CONCLUSIONS AND REMARKS

The dissipative vortexlike defects, nematic umbilical, have accompanied liquid crystals since their discovery. In spite of the large amount of experimental and theoretical studies, an entire understanding of this phase singularity solutions has not been overtaken. The existence, stability properties, and bifurcation diagram of the nematic umbilical defects through amplitude equations was presented. Close to the Fréedericksz transition of a nematic liquid crystal with negative anisotropic dielectric constant and homeotropic anchoring, an anisotropic Ginzburg-Landau equation for the transversal critical mode, which is derived by taking the 3D to 2D limit of the Frank-Oseen model, is considered. This model is a variational generalization of the Ginzburg-Landau equation with real coefficients. This model allows us to reveal the mechanism of symmetry breaking of nematic umbilical defects. The defect with positive charge is fully characterized as a function of the anisotropy, while the negative defect is characterized perturbatively. In particular, only a discrete number of solutions of the continuous family of defect persist when anisotropy is considered. Numerical simulations show quite good agreement with the analytical results.

Recently, by sending circularly polarized light beams onto a homeotropic nematic liquid crystal cell with a photosensitive wall matter vortices were spontaneously induced that remain, each stable and trapped at the chosen location [26,27]. These optical lattices and others, like the ones created using magnets by Pieranski *et al.* [28] can be understood by this amplitude equation method. In particular we expect the positive vortex to rotate when the boundary or initial conditions do not agree with the phase jump imposed by the anisotropy, as is seen in Refs. [27,28].

The anisotropic Ginzburg-Landau equation opens new avenues to the study of nematic umbilical defects such as dynamical evolution and interaction.

ACKNOWLEDGMENTS

The authors thank C. Falcon for fruitful discussions. M.G.C., M.K., and J.D. thank the financial support of FONDECYT Projects No. 1120320, No. 1130126, and No. 1130360, respectively. E.V-H. thanks CONICYT-PCHA/Magíster Nacional/2013 - 221320023. M.K. and J.D. were partially supported by Fondo Basal CMM-Chile. Experimental image of umbilical defects [Fig. 1(c)] courtesy of V. Odent.

APPENDIX: 3D TO 2D ASYMPTOTICS FOR THE FULL FRANK-OSEEN MODEL NEAR THE FRÉEDERICKSZ TRANSITION

In this Appendix we provide some details of the calculation that leads from Eq. (1) to Eq. (2) in the limit $d \to 0$. As we pointed out it suffices to identify terms of order $\mathcal{O}(1)$ and those of order $\mathcal{O}(d^2)$. Taking into account that *a priori* $n_x = \mathcal{O}(d^2)$ and $n_y = \mathcal{O}(d^2)$ it is rather easy to identify these orders. For brevity in the following we will only consider the $\hat{x}$ component, calculations involving $\hat{y}$ component being similar. In the notation of Sec. II A we have the following terms at order $\mathcal{O}(1)$ and $\mathcal{O}(d^2)$:

$$\begin{aligned}
&-\big[K_3\big(\nabla_\perp^2 n_x + d^{-2}\partial_{\zeta\zeta}^2 n_x - n_x n_z d^{-2}\partial_{\zeta\zeta}^2 n_z\big)\\
&\quad +(K_3 - K_1)\big(n_x n_z d^{-2}\partial_{\zeta\zeta}^2 n_z - \partial_{xx}^2 n_x - \partial_{xy}^2 n_y\big)\\
&\quad -(K_2 - K_3)\big(\partial_{xy}^2 n_y - \partial_{yy}^2 n_x\big)\big]\\
&\quad -\epsilon_a V_{FT}^2 d^{-2} n_x - 2\epsilon_a V_{FT} V_1 n_x + \gamma\,\partial_t n_x .
\end{aligned}$$

Taking into account the definition of V_{FT} we see that $\mathcal{O}(1)$ terms above cancel and we are left with

$$\begin{aligned}
g_x = &-\big[\big(K_1\partial_{xx}^2 u_0 + K_2\partial_{yy}^2 u_0 + (K_1 - K_2)\partial_{xy}^2 v_0\big)\cos(\pi\zeta)\\
&+K_1 u_0 \tfrac{1}{2}\big(u_0^2 + v_0^2\big)\cos(\pi\zeta)\partial_{\zeta\zeta}^2 \cos^2(\pi\zeta)\\
&-2\epsilon_a V_{FT} V_1 u_0 \cos(\pi\zeta)\big] + \gamma\cos(\pi\zeta)\partial_t u_0 .
\end{aligned}$$

Condition $\int_{-1/2}^{1/2} g_x \cos(\pi\zeta)\, d\zeta = 0$ leads to

$$\begin{aligned}
\gamma\,\partial_t u_0 = &\ \frac{K_1 + K_2}{2}\nabla_\perp^2 u_0\\
&+ \frac{K_1 - K_2}{2}\big[\big(\partial_{xx}^2 - \partial_{yy}^2\big)u_0 + 2\partial_{xy}^2 v_0\big]\\
&- \frac{K_1}{2}\pi^2 u_0\big(u_0^2 + v_0^2\big) - \epsilon_a V_{FT} V_1 u_0 .
\end{aligned}$$

From this, taking into account a similar equation in the direction $\hat{y}$ we get Eq. (2).

[1] G. Nicolis and I. Prigogine, *Self-Organization in Non-Equilibrium Systems* (Wiley, New York, 1977).
[2] L. M. Pismen, *Patterns and Interfaces in Dissipative Dynamics*, Springer Series in Synergetics (Springer, Berlin, 2006).
[3] M. C. Cross and P. C. Hohenberg, Rev. Mod. Phys. **65**, 851 (1993).
[4] L. M. Pismen, *Vortices in Nonlinear Fields* (Clarendon Press, Oxford, 1999), and references therein.
[5] S. Chandrasekhar, *Liquid Crystals* (Cambridge University Press, Cambridge, 1992).
[6] P. G. de Gennes and J. Prost, *The Physics of Liquid Crystals*, 2nd ed. (Oxford Science Publications, Clarendon Press, Oxford, 1993).
[7] P. Oswald and P. Pieranski, *Nematic and Cholesteric Liquid Crystals* (Taylor & Francis Group, Boca Raton, 2005).
[8] O. Lehmann, Z. Phys. Chem. **4**, 462 (1889).
[9] G. Friedel, Annales de Physique **18**, 273 (1922).
[10] F. C. Frank, Disc. Faraday Soc. **25**, 19 (1958).
[11] A. Rapini, J. Physique **34**, 629 (1973).
[12] T. Frisch, S. Rica, P. Coullet, and J. M. Gilli, Phys. Rev. Lett. **72**, 1471 (1994).
[13] T. Frisch, Physica D **84**, 601 (1995).
[14] A. Saupe, Mol. Cryst. Liq. Cryst. **21**, 211 (1973).
[15] I. S. Aranson and L. S. Tsimring, Phys. Rev. E **74**, 031915 (2006).
[16] I. Aranson and L. Kramer, Rev. Mod. Phys. **74**, 99 (2002).
[17] V. L. Ginzburg and L. P. Pitaevskii, Sov. Phys. JETP **7**, 858 (1958).
[18] F. Bethuel, H. Brezis, and F. Helein, *Ginzburg-Landau Vortices* (Springer, New York, 1994).
[19] Q. Han and T.-C. Lin, Nonlinearity **15**, 257 (2002).
[20] M. Kim and D. Phillips, Commun. Math. Phys. **310**, 299 (2012).
[21] R. B. Meyer, Philos. Mag. **27**, 405 (1973).
[22] R. Barboza, T. Sauma, U. Bortolozzo, G. Assanto, M. G. Clerc, and S. Residori, New J. Phys. **15**, 013028 (2013).
[23] I. Dierking, M. Ravnik, E. Lark, J. Healey, G. P. Alexander, and J. M. Yeomans, Phys. Rev. E **85**, 021703 (2012).
[24] S. H. Strogatz, *Nonlinear Dynamics and Chaos: With Applications to Physics, Biology, Chemistry and Engineering* (Addison-Wesley, Reading, Massachusetts, 1994).
[25] J. D. Crawford, Rev. Mod. Phys. **63**, 991 (1991).
[26] R. Barboza, U. Bortolozzo, G. Assanto, E. Vidal-Henriquez, M. G. Clerc, and S. Residori, Phys. Rev. Lett. **109**, 143901 (2012).
[27] R. Barboza, U. Bortolozzo, G. Assanto, E. Vidal-Henriquez, M. G. Clerc, and S. Residori, Phys. Rev. Lett. **111**, 093902 (2013).
[28] P. Pieranski, B. Yang, L. J. Burtz, A. Camu, and F. Simonetti, Liq. Cryst. **40**, 1593 (2013).

Appendix D

Light-matter interaction induces a single positive vortex with swirling arms

This Appendix is the paper entitled "Light-matter interaction induces a single positive vortex with swirling arms" published in Philosophical Transactions of the Royal Society A.

PHILOSOPHICAL TRANSACTIONS OF THE ROYAL SOCIETY A

rsta.royalsocietypublishing.org

Light–matter interaction induces a single positive vortex with swirling arms

R. Barboza[1,2], U. Bortolozzo[2], M. G. Clerc[1], S. Residori[2,3] and E. Vidal-Henriquez[1]

[1]Departamento de Física, FCFM, Universidad de Chile, Casilla 487-3, Santiago, Chile
[2]INLN, Université de Nice-Sophia Antipolis, CNRS, 1361 Route des Lucioles, 06560 Valbonne, France
[3]University of Verona, Department of Computer Science, Strada Le Grazie 15, 37134 Verona, Italy

Research

Cite this article: Barboza R, Bortolozzo U, Clerc MG, Residori S, Vidal-Henriquez E. 2014 Light–matter interaction induces a single positive vortex with swirling arms. *Phil. Trans. R. Soc. A* **372**: 20140019. http://dx.doi.org/10.1098/rsta.2014.0019

One contribution of 19 to a Theme Issue 'Localized structures in dissipative media: from optics to plant ecology'.

Subject Areas:
optics, complexity, mathematical physics

Keywords:
phase singularities, localized structures, optical vortexes

Author for correspondence:
S. Residori
e-mail: stefania.residori@inln.cnrs.fr

Homeotropic nematic liquid crystal cells with a photosensitive wall and negative dielectric anisotropy exhibit, under the influence of local illumination, stable vortexes with swirling arms that are trapped at the illuminated area. Close to the Fréedericksz transition an amplitude equation is derived, which allows us to understand the origin of the induced vortex and the competition between the illuminating profile and the elastic anisotropy generating the swirling of the arms.

1. Introduction

Motivated by the unexpected intricate structures of radio echoes from the bottom of the Antarctic ice sheet, Nye & Berry [1] conducted ultrasound pulse experiments on a rough surface, allowing them to establish the emergence of singularities in wave trains, *optical vortexes*. These are singular points where the electromagnetic field goes to zero and around which the phase forms an n-armed spiral profile, with n the topological charge (see [2–4] and references therein). In low-order Gauss–Laguerre beams, a single optical vortex corresponds to a phase singularity on the beam axis [5]. Optical vortexes have been introduced on symmetry grounds as the topological defects arising above the laser transition [6] and, in this context, identified as phase singularities appearing and disappearing in pairs of opposite charge. Reported in several experiments, such as photorefractive cavities [7] and lasers [8,9], phase

Royal Society Publishing

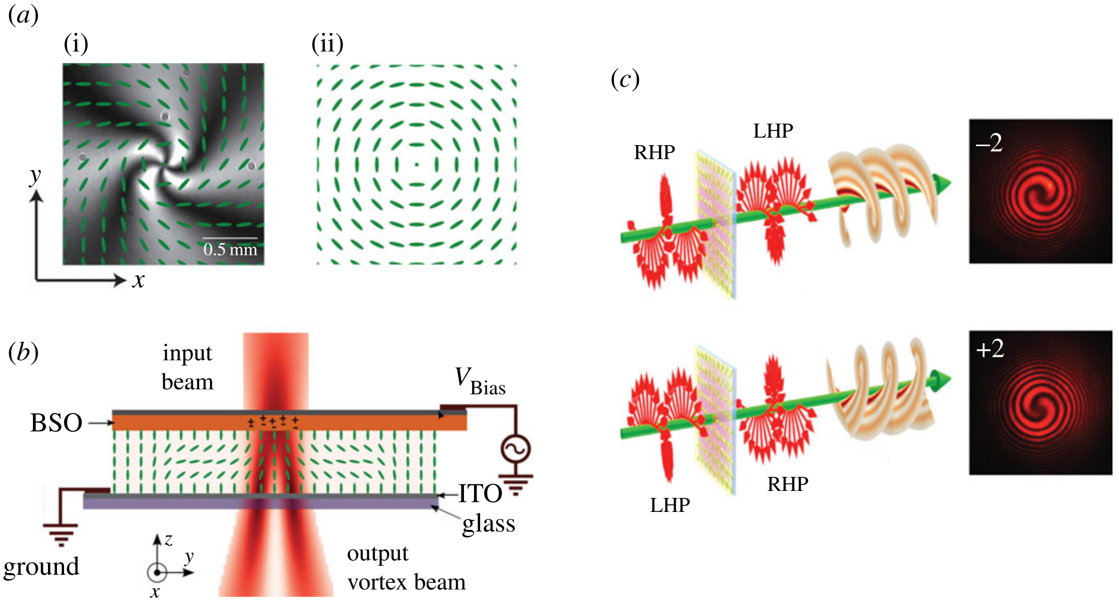

Figure 1. (*a*) Umbilical defect exhibiting swirling arms with superposed molecular organization (i); for comparison the molecular organization of a defect with straight cross arms is shown in (ii). (*b*) Set-up for the optical induction of a matter vortex induction: a circularly polarized beam is incident on the photoconductive side of the LC light valve; the voltage V_{Bias} is such that only the illuminated region undergoes the Fréedericksz transition; when reorienting, the LC molecules follow the circular pattern associated with the electric field and create the matter vortex; this, in turn, induces an optical vortex at the exit of the sample. (*c*) Schematic of the spin-orbital angular momentum transfer through the optically induced defect: an RHP (LHP) circularly polarized beam is converted into an LHP (RHP) beam with a phase singularity of topological charge −2 (+2); experimental interferograms are shown beside the respective panels. (Online version in colour.)

singularities are currently receiving a lot of attention in view of their applications, e.g. light–matter angular momentum exchange [10], optical tweezers [11–13], quantum computation [14], astronomical imaging [15] and data transmission [16].

Optical vortexes have mainly been generated with spiral phase plates [17] or diffractive elements [18]. Recently, the introduction of q-plates, planar elements with a pre-set azimuthal orientation in nematic liquid crystals (LCs), has opened up promising new avenues [19], as well as exploiting the umbilical defects in nematic textures [20]. This approach provides both tunability and high efficiency, although the LC alignment can cause some beam deformation and a consequent degradation of the generated optical vortexes [21]. Recently, by exploiting reorientational nonlinearities in the nematic LC layer of a light valve, we have accomplished the optically addressed self-induction of vortex beams that are self-aligned with the impinging light beam [22]. The spontaneous nature of the induction process guarantees that the generated defect is aligned with the incoming light beam.

In this framework, optical vortexes derive directly from the induced umbilical defects in the LC texture. Indeed, the umbilical defect is one that naturally possesses a vortex-like morphology, making it attractive for spontaneously enabling the matter template to impress a helical structure on an incoming light wavefront. Based on this vortex induction process, we have demonstrated the realization of programmable lattices of optical vortexes with an arbitrary distribution in space [23]. An intriguing property of the induced matter vortexes is their stationary swirling arms (cf. figure 1*a*). These arms are related to the phase jumps of the vortex, or the nullclines (zero-growth isoclines) showed by crossed polarizers, used to characterize the texture of umbilical defects. From the theoretical point of view, this type of behaviour is not usually expected from its universal description, *complex Ginzburg–Landau equation* (CGLE), where the arms are characterized by a cross with straight lines [2].

The aim of this paper is to establish the origin of the swirling arms of the matter vortex trapped by light in a homeotropic nematic LC cell with a photosensitive wall and negative dielectric anisotropy. Based on bifurcation theory, close to the Fréedericksz transition [24], a forced Ginzburg–Landau equation is derived. This equation allows us to understand the origin of the induced vortex, particularly the competition between the forcing generated by the light beam and the elastic medium anisotropy, which generates the swirling of the vortex arms. Numerical simulations of the amplitude equation and experimental observations show quite good agreement.

2. Experimental observation of the optically induced matter vortex

The set-up for vortex induction is sketched in figure 1*b*. The liquid crystal light valve (LCLV) is prepared by interposing a $d = 15\,\mu\text{m}$ layer of nematic LC (MLC6608 from Merck) in between two parallel planar interfaces, a glass plate and a slab of the transparent photoconductor $\text{Bi}_{12}\text{SiO}_{20}$ (BSO), $25 \times 25\,\text{mm}^2$, thickness 1 mm. The interior surfaces are treated to obtain the homeotropic anchoring of the LC, that is, with the nematic director orthogonal to the confining walls (cf. figure 1*b*). The outer surface of the photoconductor and the inner surface of the glass plate are uniformly coated with thin transparent indium–tin–oxide (ITO) electrodes, through which a voltage V_0 is applied to the cell. The employed LC has a negative dielectric anisotropy, $\epsilon_a = \epsilon_\parallel - \epsilon_\perp < 0$, with $\epsilon_\parallel$ and $\epsilon_\perp$ the dielectric susceptibility for low-frequency electric fields parallel and orthogonal, respectively, to the molecular director [24].

When a bias V_{Bias} is applied to the LCLV beyond the Fréedericskz transition voltage V_{FT}, the molecules tend to reorient perpendicularly to the (low-frequency) electric field because of the negative ϵ_a; hence, since $\boldsymbol{E} = (V_s/d)\hat{\boldsymbol{z}}$ (with V_s the voltage at the LC–BSO interface) is applied along the longitudinal z-direction and the 2π azimuthal degeneracy imposes rotational invariance around it, the LC molecules can arbitrarily align themselves in any direction, spontaneously forming spatial domains separated by umbilical defects or vortexes [24]. In the conducted experiment, we kept $V_{\text{Bias}} \lesssim V_{\text{FT}}$, in order to avoid spontaneous reorientation while bringing the molecules close to the transition point. When a light beam is incident onto the photosensitive wall of the LCLV, due to the photo-generated charges there is a slight increase in the voltage that effectively drops across the LC region underneath: the Fréedericksz threshold is locally overcome and the molecules start reorienting following the intensity gradients associated with the Gaussian beam profile of the incoming beam. Then, the light on the matter induces, through the photosensitive wall, a vortex with positive topological charge (using the convention of the right-hand rule). Figure 1*a* illustrates the typically observed vortex when one uses crossed polarizers. The black cross appearing in these conditions is the signature of an umbilical defect, which can be produced by two different types of deformations of the nematic texture, corresponding to ±1 charge, or winding numbers, of the defect [24].

To prove the optical induction of the matter vortex, and the subsequent transfer from spin to orbital angular momentum, which is mediated by the light–matter interaction, a circularly polarized laser beam of wavelength $\lambda = 632\,\text{nm}$, power $P = 0.55\,\text{mW}$ is focused to a diameter of $395\,\mu\text{m}$ on the photoconductive side of the LCLV. The input beam polarization is taken either right-handed circular or left-handed circular. Typical snapshots of the output beams observed in the two cases are illustrated in figure 2*c*, where the interferograms, made with a spherical reference wave, show the helical structure of the output wavefront. The bias voltage of the LCLV was fixed to $V_0 = 24\,\text{V}$ RMS at frequency 100 Hz. The spin-to-orbital angular momentum transfer is consistent with a $+1$ q-plate; therefore, the matter vortex is a $+1$ defect [19].

A characteristic feature of the observed vortex is that its arms are bent and thus swirling around the defect core. Experimental snapshots showing the matter defect with clockwise and anticlockwise swirling arms are displayed in figure 2*a*(i) and (ii), respectively. In order to discriminate the sign of the defect, we carried out spatially resolved polarimetry [25]. Using quarter-wave plates, we analysed the local birefringence and reconstructed the director distribution around the defect (figure 2*b*). The obtained polarimetric profile allowed us to infer

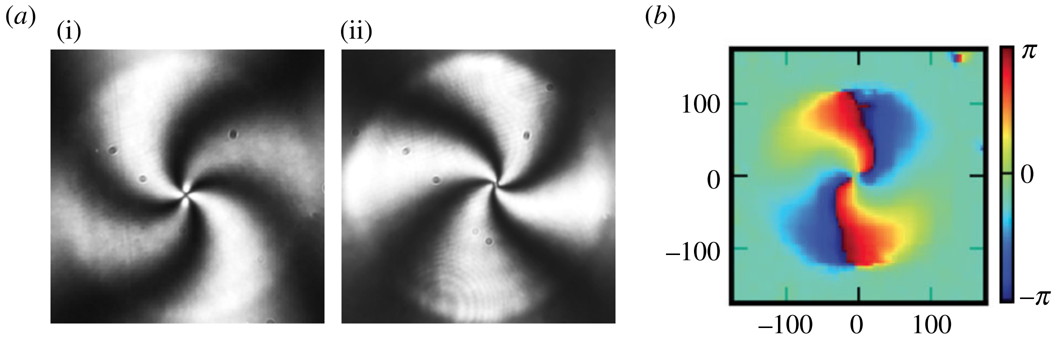

Figure 2. Matter vortex: (*a*) intensity profiles recorded under white light illumination and crossed polarizers showing clockwise (i) and anticlockwise (ii) swirling arms; (*b*) spatially resolved polarimetry in the case of a defect with anticlockwise swirling arms. (Online version in colour.)

that the defect is indeed umbilical and of winding number +1. Note that the reconstructed phase is 2θ, with θ the LC tilt in the transverse plane; therefore, the 4π phase jump around the singularity indicates a 2π change of the LC tilt angle θ. In addition, this type of method allows us to observe the bending of the arms of the vortex (cf. figure 2*b*).

3. Amplitude equation close to the Fréedericksz transition

In order to elucidate the mechanism of creation and pinning of matter vortexes, we derive an amplitude equation in the vicinity of the Fréedericksz transition, a limit where analytical results are accessible as nematic LC molecules are weakly tilted from the longitudinal axis $\hat{z}$ and backflow effects can safely be neglected. Illuminating the LCLV with a Gaussian beam induces a voltage drop with a bell-shaped profile across the LC layer, higher in the centre of the illuminated area. To determine the shape of the voltage drop within the sample, one can consider the sample as consisting of two infinitely extended planar parallel plates separated by a distance d. The upper plate, located at $z=d$, is lit by a Gaussian beam. By introducing cylindrical coordinates, the voltage $V(r,\theta,z)$ satisfies the Laplace equation

$$\partial_{zz}V+\frac{\varepsilon_{\perp}}{\varepsilon_{\parallel}}\nabla_{\perp}^{2}V=0,$$

where $\nabla_{\perp}^{2}$ stands for the transverse Laplacian operator in polar coordinates. The voltage satisfies the boundary conditions in the respective plates $V(r,\theta,z=d)=V_0+\alpha I(r)$ and $V(r,\theta,z=0)=0$, with V_0 the voltage across the LC layer in the absence of light, (r,θ) the polar coordinates in the plane where the origin of the coordinate system corresponds to the centre of the beam and $\theta=0$ accounts for the x-axis (figure 1*b*), $I(r)$ stands for the intensity of the Gaussian beam, and $I(r)=I_0\,\mathrm{e}^{-r^2/\omega^2}$, with I_0 the peak intensity and ω the beam waist. By using the Fourier transform in polar coordinates and solving the above equation with the corresponding boundary conditions, after straightforward calculations one obtains

$$V(z,r)=\frac{1}{2\pi}\int_{-\infty}^{\infty}\mathrm{d}k\,\mathrm{e}^{-\mathrm{i}k\cdot r_{\perp}}\frac{\sinh\left(\sqrt{\varepsilon_{\perp}/\varepsilon_{\parallel}}\,kz\right)}{\sinh(\sqrt{\varepsilon_{\perp}/\varepsilon_{\parallel}}\,kd)}\left(\int_{0}^{\infty}\mathrm{d}r_{\perp}^{*}\,\mathrm{e}^{\mathrm{i}k\cdot r_{\perp}^{*}}\left[V_0+\alpha I\left(\frac{r_{\perp}^{*}}{\omega}\right)\right]\right).$$

This expression is an exact analytical solution; however it is too intricate to infer results from it. For the sake of simplicity, we consider the limit of a Gaussian beam sufficiently flattened ($\omega\rightarrow\infty$). In this limit, the above expression, at the dominant order, takes the form

$$V(z,r)\approx\frac{z}{d}\left[V_0+\alpha I\left(\frac{r}{\omega}\right)\right].$$

The first and second terms on the right-hand side account for the externally applied bias and the voltage drop induced by the Gaussian beam impinging on the sample, respectively. Figure 3*a*

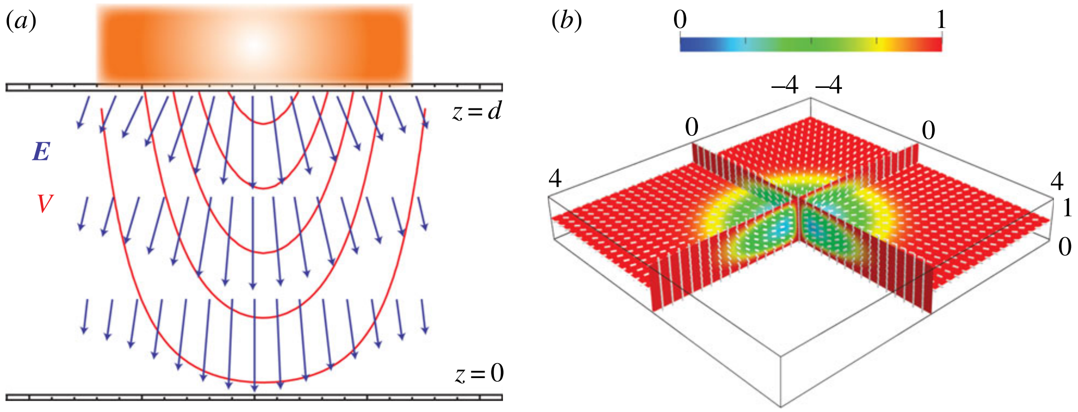

Figure 3. (*a*) Vertical cross section showing a schematic of the electric field (arrows) and voltage drop (isolines) across the LC layer when a laser beam illuminates the sample from above; (*b*) corresponding top view of the LC director orientation; the illuminating laser beam is impinging at the centre of the sample. (Online version in colour.)

illustrates the voltage drop inside the LCLV in a vertical cross-sectional view. Then, the electric field $\boldsymbol{E}(r,\theta,z)$ inside the LCLV takes the form

$$\boldsymbol{E}=-\boldsymbol{\nabla}V=E_z\hat{\boldsymbol{z}}+E_r\hat{\boldsymbol{r}}=-\frac{1}{d}\left[V_0+\alpha I\left(\frac{r}{\omega}\right)\right]\hat{\boldsymbol{z}}-\frac{z\alpha}{d\omega}\frac{\mathrm{d}I(r/\omega)}{\mathrm{d}r}\hat{\boldsymbol{r}},$$

with $\hat{\boldsymbol{z}}$ and $\hat{\boldsymbol{r}}$ the unit vectors in cylindrical coordinates (figure 3*a*). Note that the electric field contains an axisymmetrical structure. This structure will be responsible for inducing a matter vortex (cf. figure 3). The presence of an inhomogeneous electric field strongly modifies the dynamics of the LC director $\boldsymbol{n}$. The dynamical equation for the molecular director $\boldsymbol{n}$ reads [26]

$$\begin{aligned}\gamma\partial_t\boldsymbol{n}=&K_3[\nabla^2\boldsymbol{n}-\boldsymbol{n}(\boldsymbol{n}\cdot\nabla^2\boldsymbol{n})]+(K_3-K_1)[\boldsymbol{n}(\boldsymbol{n}\cdot\boldsymbol{\nabla})(\boldsymbol{\nabla}\cdot\boldsymbol{n})-\boldsymbol{\nabla}(\boldsymbol{n}\cdot\boldsymbol{\nabla})]\\&+2(K_2-K_3)[(\boldsymbol{n}\cdot\boldsymbol{\nabla}\times\boldsymbol{n})(\boldsymbol{n}(\boldsymbol{n}\cdot\boldsymbol{\nabla}\times\boldsymbol{n})-\boldsymbol{\nabla}\times\boldsymbol{n})+\boldsymbol{n}\times\boldsymbol{\nabla}(\boldsymbol{n}\cdot\boldsymbol{\nabla}\times\boldsymbol{n})]\\&+\varepsilon_a(\boldsymbol{n}\cdot\boldsymbol{E})[\boldsymbol{E}-\boldsymbol{n}(\boldsymbol{n}\cdot\boldsymbol{E})],\end{aligned}$$

where γ is the relaxation time and $\{K_1,K_2,K_3\}$ are the nematic LC elastic constants [24,26]. The dynamical behaviour of the director is of relaxation type and is characterized by preserving its norm. The homeotropic state, $\boldsymbol{n}=\hat{\boldsymbol{z}}$, undergoes a stationary instability for critical values of the voltage $V_0\equiv V_{\mathrm{FT}}=\sqrt{-K_3\pi^2/\varepsilon_a}$, which corresponds to the Fréedericksz transition of the LC [24,26]. Close to this transition point, and by considering the inhomogeneous electric field $\boldsymbol{E}(r,\theta,z)$, at the dominant order one can use the following ansatz for the amplitude of the critical mode:

$$\boldsymbol{n}(r,\theta,z)\approx\begin{pmatrix}u(r,\theta,t)\sin\left(\dfrac{\pi z}{d}\right)\\[2ex] w(r,\theta,t)\sin\left(\dfrac{\pi z}{d}\right)\\[2ex] 1-\dfrac{(u^2+w^2)}{2}\sin^2\left(\dfrac{\pi z}{d}\right)\end{pmatrix}.$$

Introducing the above ansatz in the director equation, integrating in the z coordinate over one period, and defining the complex amplitude $A\equiv u+\mathrm{i}w$, after straightforward calculations one obtains

$$\gamma\partial_t A=\mu A-aA|A|^2+K\nabla_\perp^2A+\delta\partial_{\eta,\eta}\bar{A}+b\frac{E_r(z)}{z}E_z\,\mathrm{e}^{\mathrm{i}\theta},\tag{3.1}$$

which is the amplitude equation for self-stabilization of the matter vortex [23]. Here $\mu\equiv-K_3k^2-\varepsilon_aE_z^2(r,z)$ is the bifurcation parameter (note that μ is a spatially dependent parameter), $k\equiv\pi/d$, $a\equiv-(K_3k^2/4+3\varepsilon_aE_z^2/4)>0$ is a parameter of order one that accounts for the nonlinear saturation, $b\equiv\varepsilon_a2d/\pi$, $\partial_\eta\equiv\partial_x+\mathrm{i}\partial_y$, $K\equiv(K_1+K_2)/2$ and $\delta\equiv(K_1-K_2)/(K_1+K_2)$ accounts for the elastic

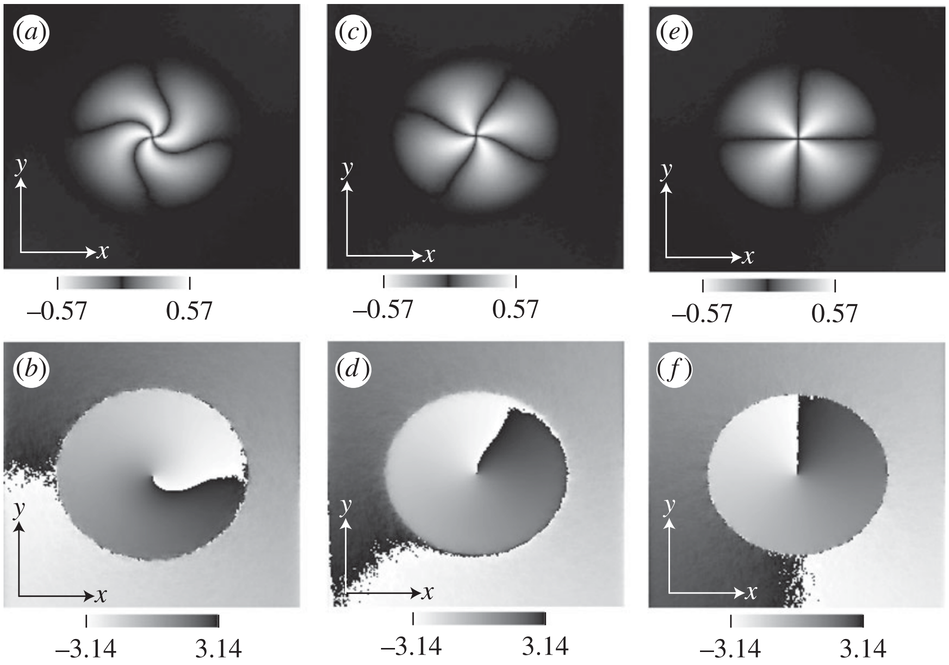

Figure 4. Vortex solution of the anisotropic and forced amplitude equation (3.1) with positive anisotropy ($\delta > 0$) and (*a*,*b*) $\theta_0 = 0$, (*c*,*d*) $\theta_0 = \pi/4$, and (*e*,*f*) $\theta_0 = \pi/2$. The top and bottom panels represent, respectively, the nullcline field $\psi(r, \theta)$, and the phase of the amplitude A. Simulations realized with $\mu = -0.5 + 1.69\,\mathrm{e}^{-r^2/\sigma^2}$, $\sigma = 18$, $\delta = 0.7$ and $b(E_r/z)E_z = 0.00169r\,\mathrm{e}^{-r^2/\sigma^2}$.

anisotropy. Note that $E_r(z)/z = -(\alpha/d\omega)\,\mathrm{d}I(r/\omega)/\mathrm{d}r$ does not depend on the z coordinate. In order to elucidate the swirling arms, we consider an extra parameter in the external forcing, changing $E_z\,\mathrm{e}^{\mathrm{i}\theta}$ for $E_z\,\mathrm{e}^{\mathrm{i}(\theta+\theta_0)}$.

The last term on the right-hand side is an external forcing generated by the inhomogeneous radial electric field, which in turn is induced by the inhomogeneous profile of the light beam. This forcing term is responsible for inducing a matter vortex with positive charge in the centre position where the applied Gaussian beam is peaked, which is at the origin of the self-stabilization mechanism for the vortex induction.

In order to characterize the dynamics of the arms of the vortex and to allow a direct comparison with the observations obtained by using crossed polarizers, let us introduce the nullcline field $\psi(r, \theta) \equiv \mathrm{Re}(A)\,\mathrm{Im}(A)$. This auxiliary field becomes zero when the real or imaginary part of A vanishes. Then, the arms and position of the vortex are represented, respectively, by the zero and the intersection of the zero nullcline curves. Figure 4 shows the nullcline field and the phase field obtained by using the above Ginzburg–Landau equation with anisotropic forcing, equation (3.1). Note that the vortexes shown in the left and centre panels are similar to those observed experimentally (figure 1). The anisotropic term (the term proportional to δ) is responsible for moving and slightly rotating the matter vortex, as we will see later.

4. Positive vortex with swirling arms

Neglecting anisotropy $\delta = 0$ ($K_1 = K_2 = K_3$) and spatial variations of the voltage ($E_r = 0$), the above model reduces to the well-known CGLE with real coefficients. This model has gathered a great interest by describing various physical systems such as fluids, superfluids, superconductors, LCs, magnetic media and optical cavities, to mention a few [2]. The main properties of the CGLE are reported in a review [27]. The CGLE admits stable dissipative vortex solutions with topological charge (winding number) ±1 [2]. To characterize these stationary solutions, let us consider the polar representation and polar coordinates $A = R_v(r)\,\mathrm{e}^{\mathrm{i}(m\theta+\varphi_0)}$, where $m = \pm 1$ is the topological

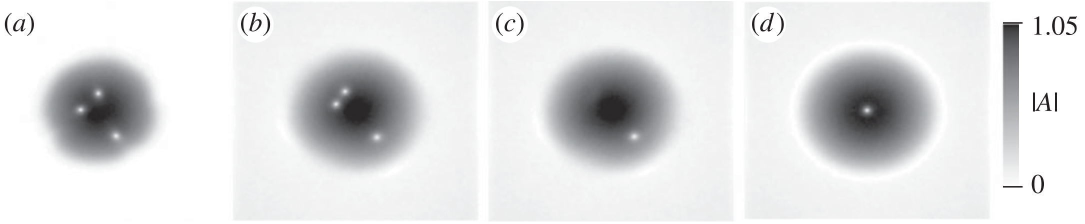

Figure 5. Dynamical evolution of the vortexes observed in the forced amplitude equation (3.1) without anisotropy ($\delta = 0$) starting from the unstable state, $A = 0$, with an initial noise. The temporal evolution is from (*a*) to (*d*). The magnitude of the amplitude $|A|$ is displayed in greyscale. The steady state, which corresponds to a single vortex trapped in the centre, is shown in (*d*). Simulations realized with $\mu = -0.5 + 1.69\,\mathrm{e}^{-r^2/\sigma^2}$, $\sigma = 18$, $\delta = 0.7$ and $b(E_r/z)E_z = 0.00169r\,\mathrm{e}^{-r^2/\sigma^2}$.

charge, and φ_0 is a continuous parameter that accounts for the phase invariance of the CGLE. The magnitude $R_v(r)$ satisfies

$$\mu_0 R_v - R_v^3 - \frac{m^2}{r^2} R_v + \frac{1}{r}\frac{\mathrm{d}R_v}{\mathrm{d}r} + \frac{\mathrm{d}^2 R_v}{\mathrm{d}^2 r} = 0, \tag{4.1}$$

where $\mu \equiv -K_3 k^2 - \varepsilon_a E_z^2$, measured in the middle of the sample. The defect solution of this model was first observed numerically in [28] and does not have an analytical expression. However, the vortex has the asymptotic behaviour

$$R_v(r) \longrightarrow \begin{cases} r, & r \longrightarrow 0, \\ \sqrt{\mu_0}\left(1 - 2\,\mathrm{e}^{-2r\sqrt{\mu_0/2}}\right), & r \longrightarrow \infty. \end{cases} \tag{4.2}$$

By using Padé approximants, one can obtain suitable approximations for the vortexes [2]. Note that the equation for the modulus of the amplitude (4.1) does not depend on the sign of the topological charge. Hence, the two vortexes are indistinguishable from the point of view of the magnitude. The nullcline field in this case takes the form $\psi(r,\theta) = R_v^2(r)\sin(2\theta)/2$. Thus, the vortex arms are characterized by being straight and orthogonal, forming a cross whose centre determines the position of the vortex. An example of this case is shown in figure 4*e*. In addition, the phase jump is characterized by a straight line emerging from the position of the vortex (figure 4*f*).

(a) Effects of forcing

When the Fréedericksz transition starts from the unstable state, $A = 0$, in the presence of noise, or under uniform illumination, the system initially generates a large number of vortexes that subsequently annihilate by pairs of opposite topological charge or fade towards the edges. Let us now consider the effect of forcing, $E_r \neq 0$, occurring in the presence of a non-uniform illumination. Such a forcing simultaneously breaks the translational symmetry and the spatial rotation and, consequently, leads to a single positive vortex to be attracted and trapped in the central position of the addressed area. Figure 5 shows a sequence of pictures illustrating the process described above. Starting from three generated vortexes, a couple of them, oppositely charged, mutually attract and annihilate (figure 5*a*–*c*), thus leaving a single positive vortex at the end (figure 5*c*). The single vortex is then attracted to the centre of the illuminated area where it remains pinned. The stationary pinned vortex is depicted in figure 5*d*.

Figure 4*e* and *f* shows, respectively, the nullcline field and the corresponding phase of the induced stationary vortex. Note that negatively charged vortexes are not consistent with the charge induced by the forcing; thus they are not a steady state. Note also that the phase jump is always consistent with that imposed by the forcing (θ_0).

(b) Effects of elastic anisotropy

We now focus on the effect of elastic anisotropy on the single positive vortex. We first ignore the inhomogeneous forcing; hence, we take $E_r = 0$. In this case, the amplitude of the critical mode satisfies the anisotropic Ginzburg–Landau equation [29]

$$\gamma\,\partial_t A = \mu_0 A - aA|A|^2 + K\nabla_\perp^2 A + \delta\,\partial_{\eta,\eta}\bar{A}. \tag{4.3}$$

By introducing the ansatz $A(r,\theta) = R(r)\,\mathrm{e}^{\mathrm{i}(\theta+\varphi_0)}$ in the above equation for the vortex solution with positive topological charge, we obtain the following set of scalar equations:

$$0 = \mu_0 R - aR^3 + (K + \delta\,\mathrm{e}^{-2\mathrm{i}\varphi_0})\left(\frac{\mathrm{d}^2R}{\mathrm{d}^2r} + \frac{1}{r}\frac{\mathrm{d}R}{\mathrm{d}r} - \frac{R}{r^2}\right) \tag{4.4}$$

and

$$0 = \delta\sin 2\varphi_0\left(\frac{\mathrm{d}^2R}{\mathrm{d}^2r} + \frac{1}{r}\frac{\mathrm{d}R}{\mathrm{d}r} - \frac{R}{r^2}\right). \tag{4.5}$$

From equation (4.5), the only possibility to obtain a non-trivial solution is to consider the phase parameter satisfying $\sin 2\varphi_0 = 0$, which gives the solutions $\varphi_0 = \{0, \pi/2, \pi, 3\pi/2\}$. Therefore, from the continuous family of possible phase jumps, only four possibilities survive. On the other hand, the equation for the magnitude of the amplitude reads

$$0 = \mu_0 R - aR^3 + (K + \delta\cos 2\varphi_0)\left(\frac{\mathrm{d}^2R}{\mathrm{d}^2r} + \frac{1}{r}\frac{\mathrm{d}R}{\mathrm{d}r} - \frac{R}{r^2}\right). \tag{4.6}$$

Owing to the periodicity of the cosine function, we only have two possibilities, $\cos 2\varphi_0 = \pm 1$. Rescaling the space by the factor $\sqrt{1\pm\delta}$, the above equation becomes equation (4.1). Therefore, the isotropic positive vortex has the solution

$$A = R_v\left(\frac{r}{\sqrt{1\pm\delta}}\right)\mathrm{e}^{\mathrm{i}(\theta+\pi/4\mp\pi/4+n\pi)}, \tag{4.7}$$

with $n = 0, \pm1, \pm2, \ldots$. Consequently, the anisotropic vortex solution with positive charge corresponds to a simple scaling of the isotropic vortex solution, notwithstanding, with a finite number of possible phase jumps ($\varphi_0 = \{0, \pi/2, \pi, 3\pi/2\}$), in opposition, with the isotropic system, which has an infinite number of solutions parametrized by the continuous parameter φ_0. Of the four solutions found, those with a smaller core are stable and the others are unstable. It can be inferred from energy calculations, or through numerical simulations, that for positive (negative) anisotropy the stable solutions are $\varphi_0 = \{\pi/2, 3\pi/2\}$ ($\varphi_0 = \{0, \pi\}$). It is worth noting that it is known, from the variational approach to the Frank free energy, that the elastic anisotropy allows a discrete number of four possible phase jumps for umbilical defects [30,31]. These conditions are recovered by the above solutions.

(c) Simultaneous effect of anisotropy and forcing

We now consider simultaneously the effects of the elastic anisotropy, which is intrinsic to the medium properties, and the spatial forcing that is induced by the light. While the forcing induces a vortex that is pinned at the centre of the light beam and tries to impose the phase jump in θ_0, the elastic anisotropy imposes a phase jump that must be consistent with the four above-mentioned φ_0. Because the anisotropy is proportional to the spatial derivatives, we expect it to be more relevant near the core of the vortex. Therefore, one expects that the anisotropy is imposing the phase jump in the region close to the vortex core and the spatial forcing imposes the phase jump in the outer regions of the vortex. Figure 4 illustrates stationary vortexes for positive anisotropy ($\varphi_0 = \{\pi/2, 3\pi/2\}$ are privileged) with different θ_0. In the left, centre and right panels are considered $\theta_0 = 0$, $\theta_0 = \pi/4$ and $\theta_0 = \pi/2$, respectively. As a result of adjusting the respective angles of the phase jump, the vortex solution exhibits a phase gradient, which induces a small force responsible for slightly displacing the vortex from its centre.

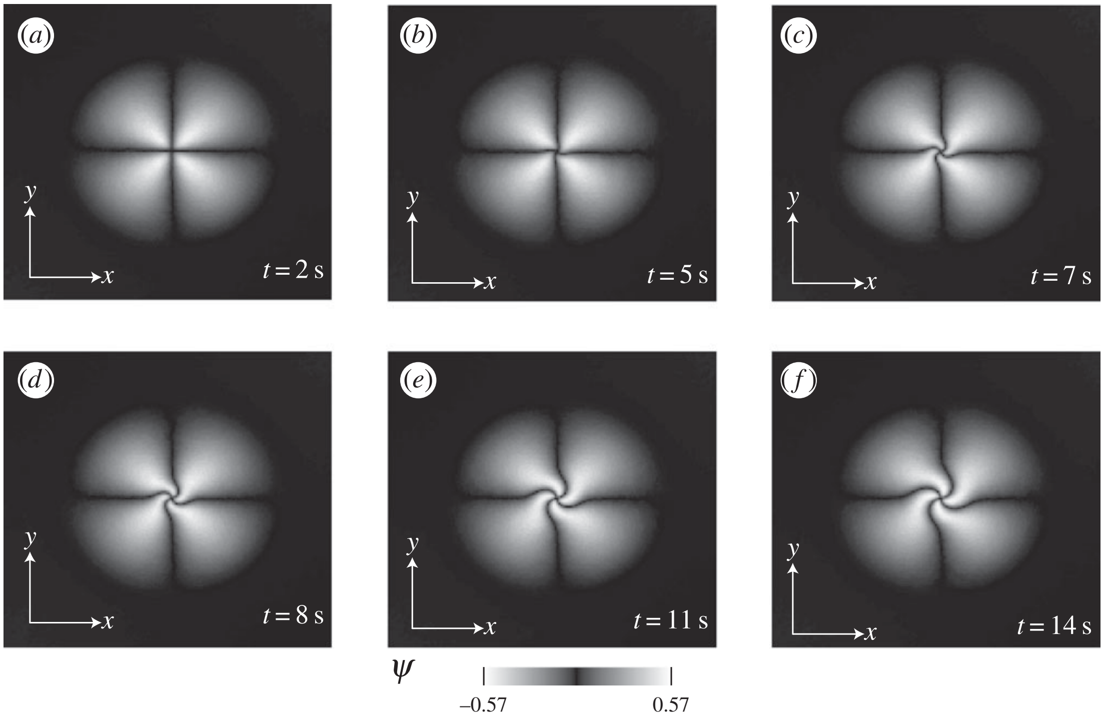

Figure 6. Bending process of the arms of a single positive vortex obtained from the forced amplitude equation (3.1) for positive elastic anisotropy. The time evolution corresponds to (*a*) to (*f*). The nullcline field ψ is displayed in greyscale. During its evolution, the vortex develops a swirling of the arms around its core. The final configuration is shown in (*f*). Simulations realized with $\mu = -0.5 + 1.69\,\mathrm{e}^{-r^2/\sigma^2}$, $\sigma = 18$, $\delta = 0.7$, and $b(E_r/z)E_z = 0.00169r\,\mathrm{e}^{-r^2/\sigma^2}$; the time shown is scaled by γ.

Therefore, the origin of the bent arms of the vortexes is simply the result of the competition between two effects: the anisotropy, imposing a phase jump angle in the core of the vortex, and the spatial forcing, imposing another phase jump angle in the outside regions. Figure 6 shows the evolution of a positive vortex initially consistent with the spatial forcing and its later temporal evolution resulting from the anisotropy. Clearly, a process of bending of the arms of the vortex is originated from the core. These numerical findings are consistent with the experimental observations.

5. Conclusion and comment

By using a nematic LC in a homeotropic light-valve geometry, we experimentally demonstrated a robust phenomenon of controlled vortex induction, which is, at the same time, spontaneous, self-stabilizing and positionally stable. After its induction, the vortex develops a swirling of the arms, which remain stationary and stable. Close to the Fréedericksz transition, an amplitude equation is derived, which allows us to understand the origin of the induced vortex and the competition between the forcing induced by the light and the elastic anisotropy that generates the swirling arms of the vortex. More precisely, the spatial forcing induces a single charge vortex, then the anisotropy imposes a phase jump in the region close to the vortex core and the spatial forcing imposes a phase jump in the outer regions. Numerical simulations of the amplitude equation show a fairly good agreement with the experimental observations.

Vortexes with swirling arms are usually observed in vortex interactions [32]. They have also been observed in LCs with an active surface [33] and in singular birefringent patterns generated by non-singular light beams [34]. All these observations can be understood as the result of the combination of the elastic anisotropy and an external forcing given, for instance, by another vortex, or by the boundary conditions, or an external field. The anisotropy and the external forcing try to impose the phase jump in different directions, generating a vortex with swirling arms.

By means of appropriate illumination profiles, one could induce vortexes of opposite charges in the same LC sample with a photosensitive wall. The interaction of oppositely charged vortexes exhibits a complex dynamics [2,32]. The characterization of the interaction of vortexes with swirling arms is a work in progress.

Acknowledgement. We acknowledge financial support of the ANR international programme, project ANR-2010-INTB-402-02 (ANR-CONICYT39), 'COLORS'.

Funding statement. M.G.C. and R.B. are grateful for financial support through FONDECYT projects 1120320 and 3140577, respectively. E.V.-H. acknowledges with thanks the Master fellowship from CONICYT contract 221320023 and financial support from DPP of the University of Chile.

References

1. Nye JF, Berry MV. 1974 Dislocations in wave trains. *Proc. R. Soc. Lond. A* **336**, 165–190. (doi:10.1098/rspa.1974.0012)
2. Pismen LM. 1999 *Vortices in nonlinear fields*. New York, NY: Oxford Science Publications.
3. Soskin MS, Vasnetov MV. 2001 Singular optics. In *Progress in optics*, vol. 42 (ed. E Wolf), pp. 219–276. Amsterdam, The Netherlands: Elsevier. (doi:10.1016/S0079-6638(01)80018-4)
4. Staliunas K, Sanchez-Morcillo VJ. 2003 *Transverse patterns in nonlinear optical resonators*. Springer Tracts in Modern Physics, vol. 183. Berlin, Germany: Springer. (doi:10.1007/3-540-36416-1)
5. Yao AM, Padgett MJ. 2011 Orbital angular momentum: origins, behavior and applications. *Adv. Opt. Photonics* **3**, 161–204. (doi:10.1364/AOP.3.000161)
6. Coullet P, Gil L, Rocca F. 1989 Optical vortices. *Opt. Commun.* **73**, 403–408. (doi:10.1016/0030-4018(89)90180-6)
7. Arecchi FT, Giacomelli G, Ramazza PL, Residori S. 1991 Vortices and defect statistics in two-dimensional optical chaos. *Phys. Rev. Lett.* **67**, 3749. (doi:10.1103/PhysRevLett.67.3749)
8. Brambilla M, Battipede F, Lugiato LA, Penna V, Prati F, Tamm C, Weiss CO. 1991 Transverse laser patterns. I. Phase singularity crystals. *Phys. Rev. A* **43**, 5090. (doi:10.1103/PhysRevA.43.5090)
9. Weiss CO, Telle HR, Staliunas K, Brambilla M. 1993 Restless optical vortex. *Phys. Rev. A* **47**, R1616. (doi:10.1103/PhysRevA.47.R1616)
10. Allen L, Beijersbergen MW, Spreeuw RJC, Woerdman JP. 1992 Orbital angular momentum of light and the transformation of Laguerre–Gaussian laser modes. *Phys. Rev. A* **45**, 8185. (doi:10.1103/PhysRevA.45.8185)
11. Grier DG. 2003 A revolution in optical manipulation. *Nature* **424**, 810–816. (doi:10.1038/nature01935)
12. Shvedov VG, Rode AV, Izdebskaya YV, Desyatnikov AS, Krolikowski W, Kivshar YS. 2010 Giant optical manipulation. *Phys. Rev. Lett.* **105**, 118103. (doi:10.1103/PhysRevLett.105.118103)
13. Padgett M, Bowman R. 2011 Tweezers with a twist. *Nat. Photonics* **5**, 343–348. (doi:10.1038/nphoton.2011.81)
14. Arnaut HH, Barbosa GA. 2000 Orbital and intrinsic angular momentum of single photons and entangled pairs of photons generated by parametric down-conversion. *Phys. Rev. Lett.* **85**, 286–289. (doi:10.1103/PhysRevLett.85.286)
15. Tamburini F, Anzolin G, Umbriaco G, Bianchini A, Barbieri C. 2006 Overcoming the Rayleigh criterion limit with optical vortices. *Phys. Rev. Lett.* **97**, 163903. (doi:10.1103/PhysRevLett.97.163903)
16. Wang J *et al.* 2012 Terabit free-space data transmission employing orbital angular momentum multiplexing. *Nat. Photonics* **6**, 488–496. (doi:10.1038/nphoton.2012.138)
17. Beijersbergen MW, Allen L, van der Veen HELO, Woerdman JP. 1993 Astigmatic laser mode converters and transfer of orbital angular momentum. *Opt. Commun.* **96**, 123–132. (doi:10.1016/0030-4018(93)90535-D)
18. Sacks Z, Rozas D, Swartzlander GA. 1998 Holographic formation of optical-vortex filaments. *J. Opt. Soc. Am.* **B15**, 2226–2234. (doi:10.1364/JOSAB.15.002226)
19. Marrucci L, Manzo C, Paparo D. 2006 Optical spin-to-orbital angular momentum conversion in inhomogeneous anisotropic media. *Phys. Rev. Lett.* **96**, 163905. (doi:10.1103/PhysRevLett.96.163905)
20. Brasselet E. 2012 Tunable optical vortex arrays from a single nematic topological defect. *Phys. Rev. Lett.* **108**, 087801. (doi:10.1103/PhysRevLett.108.087801)

21. Bekshaev AY, Sviridova SV. 2010 Effects of misalignments in the optical vortex transformation performed by holograms with embedded phase singularity. *Opt. Commun.* **283**, 4866–4876. (doi:10.1016/j.optcom.2010.07.031)
22. Barboza R, Bortolozzo U, Assanto G, Vidal-Henriquez E, Clerc MG, Residori S. 2012 Vortex induction via anisotropy stabilized light–matter interaction. *Phys. Rev. Lett.* **109**, 143901. (doi:10.1103/PhysRevLett.109.143901)
23. Barboza R, Bortolozzo U, Assanto G, Vidal-Henriquez E, Clerc MG, Residori S. 2013 Harnessing optical vortex lattices in nematic liquid crystals. *Phys. Rev. Lett.* **111**, 93902. (doi:10.1103/PhysRevLett.111.093902)
24. Chandrasekhar S. 1977 *Liquid crystals*. New York, NY: Cambridge University Press.
25. Soskin MS, Denisenko VG, Egorov RI. 2004 Singular Stokes-polarimetry as new technique for metrology and inspection of polarized speckle fields. *Proc. SPIE* **5458**, 79. (doi:10.1117/12.544681)
26. de Gennes PG, Prost J. 1993 *The physics of liquid crystals*, 2nd edn. New York, NY: Oxford Science Publications.
27. Aranson I, Kramer L. 2002 The world of the complex Ginzburg–Landau equation. *Rev. Mod. Phys.* **74**, 99–143. (doi:10.1103/RevModPhys.74.99)
28. Ginzburg VL, Pitaeskii LP. 1958 On the theory of superfluidity. *Sov. Phys. JETP* **7**, 858.
29. Frisch T, Rica S, Coullet P, Gilli JM. 1994 Spiral waves in liquid crystal. *Phys. Rev. Lett.* **72**, 1471–1474. (doi:10.1103/PhysRevLett.72.1471)
30. Rapini A. 1973 Umbilics: static properties and shear-induced displacements. *J Physique* **34**, 629–633. (doi:10.1051/jphys:01973003407062900)
31. Nehring JR, Saupe A. 1972 On the schlieren texture in nematic and smectic liquid crystals. *J. Chem. Soc.* **2**, 1–15. (doi:10.1039/f29726800001)
32. Barboza R, Sauma T, Bortolozzo U, Assanto G, Clerc MG, Residori S. 2013 Characterization of the vortex-pair interaction law and nonlinear mobility effects. *New J. Phys.* **15**, 013028. (doi:10.1088/1367-2630/15/1/013028)
33. McCamley MK, Crawford GP, Ravnik M, Žumer S, Artenstein AW, Opal SM. 2007 Optical detection of anchoring at free and fluid surfaces using a nematic liquid crystal sensor. *Appl. Phys. Lett.* **91**, 141916. (doi:10.1063/1.2795347)
34. Brasselet E. 2009 Singular optical manipulation of birefringent elastic media using nonsingular beams. *Opt. Lett.* **34**, 3229–3231. (doi:10.1364/OL.34.003229)